UCGE Reports
Number 20229

Department of Geomatics Engineering

Precise Point Positioning Using Un-Differenced Code and Carrier Phase Observations

(URL: http://www.geomatics.ucalgary.ca/links/GradTheses.html)

by

Mohamed Abdel-tawwab Abdel-salam

September 2005

SCHULICH
School of Engineering

UNIVERSITY OF CALGARY

UNIVERSITY OF CALGARY

Precise Point Positioning Using Un-Differenced Code and Carrier Phase Observations

by

Mohamed Abdel-tawwab Abdel-salam

A DISSERTATION

SUBMITTED TO THE FACULTY OF GRADUATE STUDIES

IN PARTIAL FULFILMENT OF THE REQUIREMENTS FOR THE

DEGREE OF DOCTOR OF PHILOSOPHY

DEPARTMENT OF GEOMATICS ENGINEERING

CALGARY, ALBERTA

SEPTEMBER, 2005

UNIVERSITY OF CALGARY

FACULTY OF GRADUATE STUDIES

The undersigned certify that they have read, and recommend to the Faculty of Graduate Studies for acceptance, a thesis entitled " Precise Point Positioning Using Un-Differenced Code and Carrier Phase Observations " submitted by Mohamed Abdel-tawwab Abdel-salam in partial fulfillment of the requirements of the degree of Doctor of Philosophy.

Supervisor, Dr. Yang Gao, Department of Geomatics Engineering

Dr. Naser El-Sheimy, Department of Geomatics Engineering

Dr. Abu B. Sesay, Department of Electrical and Computer Engineering

Dr. Behrouz H. Far, Department of Electrical and Computer Engineering

External Examiner, Dr. Alfred Leick, Maine University

Sept 9, 05

Date

Abstract

This thesis presents a comprehensive study of Precise Point Positioning (PPP) using un-differenced GPS pseudocode and carrier phase observations as well as precise orbit and clock data. To initiate the study, a precise point positioning system that is capable of using IGS products was developed. The thesis presents PPP error mitigation techniques, stochastic, and functional models. It tackles the positioning accuracy of PPP under different dynamic conditions using static, land vehicle, marine, and airborne data. The overall performance of PPP under these different conditions was investigated and analyzed. The thesis also investigates the convergence behavior of PPP and elucidates the potential decrease of the convergence time caused by the foreseen enhancement in precise data intervals. It has been concluded that the IGS satellite clock correction sampling intervals have a great effect on positioning accuracy. Moreover, the issue of carrier phase non-zero initial phase and its role in PPP as well as its effect on PPP ambiguity resolution was investigated. To overcome the long convergence time associated with PPP, two studies were proposed and carried out. The first study investigated the effect of troposphere modeling instead of estimation and the second study investigated the effect of discontinuing the estimation of the accurate ambiguities. The results of the two studies were analyzed and their limitations were highlighted. The issues of ambiguity estimation and the inter-frequency bias were studied. It was established that the ambiguity estimation in the existing two PPP functional models are equivalent and that the effect of the inter-frequency bias is canceled in the existing PPP functional models. Another aspect of the investigation deals with the PPP's atmosphere

sensing capability. A scheme was designed to retrieve and assess tropospheric delays obtained from PPP. The assessment was carried out with respect to the corresponding IGS tropospheric delay and the water vapor profiler. The thesis provides a new technique for estimating the ionospheric delay with the precision of carrier phase observations. The technique demonstrates high accuracy and low noise compared with the long established code-based ionospheric delay.

Acknowledgements

Dedication

To those who left our world missing us while we are away from them:
My beloved late father
GOD bless his soul

And to those who have suffered from my absence:
My family

Table of Contents

List of Figures

List of Tables

List of Abbreviations

C/A	Coarse Acquisition
CODE	Center for Orbit Determination in Europe
DART	Dynamic Ambiguity Real Time Standalone
DDGPS	Double Differential GPS
DGPS	Differential GPS
DoD	Department of Defense
DOP	Dilution of Precision
DZTD	Dry Zenith Troposphere Delay
EFEC	Earth-Fixed Earth-Centered
EGNOS	European Geostationary Navigation Overlay Service
ERP	Earth Rotation Parameters
FAA	Federal Aviation Administration
G730	Revised WGS84 Reference Frame (week 730)
G873	Revised WGS84 Reference Frame (week 873)
G1150	Revised WGS84 Reference Frame (week 1150)
GDOP	Geometrical Dilution of Precision
GPS	Global Positioning System
IAG	International Association of Geodesy
ICD	Interface Control Document
IERS	International Earth Rotation Service
IGS	International GPS service for Geodynamics
ITRF	International Terrestrial Reference Frame
JPL	Jet Propulsion Laboratory
mas	Milli Arc Second
MSAS	MTSAT Satellite Augmentation System
NAD83	The North American Datum
NAVSTAR	Navigation Satellite Timing and Ranging
NGA	National Geospatial Intelligence Agency

NGS	National Geodetic Survey
NIMA	National Imagery and Mapping Agency
NOAA	National Oceanic and Atmospheric Administration
NRCan	Natural Resources Canada
P-Code	Precise Code
PDOP	Position Dilution of Precision
ppb	Part Per Billion
PPP	Precise Point Positioning
PPS	Precise Positioning Service
PRN	Pseudo Random Noise
RCP	Right Circularly Polarized
RINEX	Receiver Independent Exchange Format
RMS	Root Mean Square
RTCM	Radio Technical Commission for Marine
RTK	Real-time Kinematic
SA	Selective Availability
SPP	Single Point Positioning
SPS	Standard Positioning Service
STD	Standard Deviation
TEC	Total Electron Content
USNO	United States Naval Observatory
VLBI	Very Long Baseline Interferometry
VTEC	Vertical Total Electron Content
WAAS	Wide Area Augmentation System
WADGPS	Wide Area Differential GPS
WGS84	World Geodetic System 1984
WVP	Water Vapor Profiler
WZTD	Wet Zenith Troposphere Delay
ZTD	Zenith Troposphere Delay

List of Symbols

β_N, β_E, βh	Correlation Time for North, East, and Height
c	Speed of Light
D, E, F1, F2, and H	Ionosphere Layers
Δ_{dry}	Dry Troposphere Delay
dt	Satellite Clock Error
dT	Receiver Clock Error
Δt_p	Gravity Delay Error
Δt_r	Relativity Corrections
Δ_{TROP}	Total Troposphere Delay
Δ_{wet}	Wet Troposphere Delay
Φ	Transition Matrix
ϕ_1	Carrier Phase Observation on L1
ϕ_2	Carrier Phase Observation on L2
ϕ_{ro}	Receiver Non-Zero Initial Phase
ϕ^s_o	Satellite Non-Zero Initial Phase
G	Gravitational Constant
h2	The Nominal Second Degree Shida Number
L1	Carrier Phase on L1
λ_1	Wavelength on L1
L2	Carrier Phase on L2
λ_2	Wavelength on L2
l2	The Nominal Second Degree Love Number
M code	New GPS Military Code
M(E)	Elevation Mapping Function
M_{dry}	Dry Mapping Function
M_E	Mass of Earth
M_{wet}	Wet Mapping Function

ν	Satellite Receiver Velocity Vector
ns	Nano Second
P(y)	Encrypted P Code
P1	P1 Code
P2	P2 Code
θg	The Greenwich Mean Sidereal Time
Qi	Noise Matrix for i Component
ρ	Satellite Receiver Geometrical Range
R_m	Earth Radius in Meridian Direction
R_n	Earth Radius in Prime Meridian Direction
S_i	Spectral Density for i Component
$S_{v\phi}$, $S_{v\lambda}$, and S_{vh}	Velocity Spectral Density in North, East, and Height
$\grave{T}_{GD,r}$	Receiver Inter-frequency Bias of Carrier Phase Observations
$\grave{T}_{GD,s}$	Satellite Inter-frequency Bias of Carrier Phase Observations
$T_{GD,r}$	Receiver Inter-frequency Bias of Pseudorange Observations
$T_{GD,s}$	Satellite Inter-frequency Bias of Pseudorange Observations
$d_{r(Interfreq/P(Li))}$	Receiver pseudocode inter-frequency bias on Li
$d^s_{Interfreq/P(Li)}$	Satellite pseudocode inter-frequency bias on Li
$\tilde{d}_{r(Interfreq/\Phi(Li))}$	Receiver carrier phase inter-frequency bias on Li
$\tilde{d}^s_{Interfreq/\Phi(Li)}$	Satellite carrier phase inter-frequency bias on Li

CHAPTER 1

INTRODUCTION

1.1 Background

Global Positioning System (GPS) is a satellite-based structure for navigation and positioning. It has become the backbone of many aspects of our live and its applications, such as vehicle navigation, recreation, and weather forecasting touch our daily activities. Many other complex applications depend heavily on GPS, such as marine navigation, airborne navigation, time transfer, rescues, mapping, and missile guidance.

GPS satellites transmit pseudocode and carrier phase observations at two frequencies. GPS receivers are capable of receiving the GPS signals at one or two frequencies. The GPS pseudocode carries a time tag identifying the time of transmission, whereas the carrier phase does not. Therefore, the pseudocode observation can be considered an absolute measurement, whereas the carrier observation is a relative one. Positioning using GPS observations is similar to the triangulation process: distances to at least four satellites are needed to estimate the GPS receiver's location and time bias. The distance between the GPS satellites and GPS receiver station can be determined by observing the

time difference between the transmitted GPS pseduocode and the receiver generated one. To account for the GPS receiver clock error, a receiver clock offset is estimated along with GPS station parameters. This simple concept of positioning is called "autonomous positioning". It is the most flexible positioning form and is the original positioning technique that GPS was designed for. However, because of the errors caused by satellite ephemerides, satellite clock, ionosphere, troposphere, multipath and noise, the accuracy of autonomous point positioning could not be better than a couple of meters even after the Selective Availability (SA) was turned off (Neilan et al.., 2000; Mohinder et al.., 2001).

Owing to these limitations, positioning and navigation techniques based on GPS have changed and evolved in the last couple of years providing positioning solutions with centimeter accuracy. However, the price of the increase in accuracy is usually paid by the increase in complexity and constraints that must be met as will be seen in the later section of this chapter. Practically, the best approach would be the development of a GPS autonomous positioning technique that has the accuracy of the modern Differential GPS (DGPS) techniques. This topic is covered in this thesis.

1.2 Precise GPS Positioning Techniques and Their Challenges

For the class of users who operate and manage precise applications, traditional GPS autonomous positional accuracy cannot meet the majority of their expectations. One way to obtain higher accuracy is to mitigate the abovementioned errors by using the spatial

correlation between one or more reference stations with known coordinates and the nearby rover GPS receiver station whose coordinates are to be determined. The concept behind this spatial correlation is that nearby GPS receivers observe all errors equally except multipath errors. The GPS positioning techniques that use the concept of spatial correlation are known as Differential GPS (DGPS) and have been widely used in one of two forms. The first form involves merging simultaneous observations of the reference receiver data with the corresponding observations from the rover GPS receiver, resulting in a relative positioning solution with respect to the reference station coordinates. The second form uses an estimated vector of double difference corrections that can be applied at the rover GPS receiver also resulting in a relative positioning solution.

Currently, increased attention is being paid to GPS global differential positioning techniques. These techniques rely on a worldwide network of reference GPS receivers and enable authorized GPS users to process their data and to get their positioning solution anywhere on the globe. The main reasons for this attention are threefold: the ability of these techniques to achieve globally consistent accuracy, the reduction of user operational costs, and the reduction of logistical complexity imposed by the necessity for simultaneous observations and the need for rover GPS stations to work in the vicinity of base stations. However, these techniques use the traditional DGPS concepts; accordingly, GPS users need to work near one of these global reference stations or a degradation in accuracy may be observed.

The numerous systems of DGPS have three drawbacks associated with them: the need for a base or reference station(s), the need for simultaneous observations between the

reference and rover stations, and the necessity for the rover GPS station to work in the vicinity of the reference stations, which define only a locally consistent reference frame.

Nowadays, the existence of the extremely precise ephemerides and clock corrections, namely precise data, has pushed global differential positioning techniques to a new era where users need precise data, which is valid globally, to obtain their positions without the need to process their data with respect to nearby reference station(s). An example for these new global techniques is Precise Point Positioning (PPP). Several organizations have started to provide precise ephemerides and satellite clock corrections. The international GPS service (IGS) is one of these organizations, which has been providing the most precise satellite ephemerides and clock corrections currently available in the market (IGS, 2004; 2004a).

This thesis focuses on a relatively new global positioning technique, namely Precise Point Positioning (PPP) that uses un-differenced pseudorange and carrier phase observations from a single high precision dual frequency GPS receiver in addition to precise ephemeredes and satellite clock data. This technique does not suffer from the drawbacks of the conventional DGPS techniques and has the potential to provide the same positioning accuracy without the requirement of a reference station(s). The success of this system will significantly improve the operational flexibility of precise positioning using GPS and at the same time reduce the field operational costs. Such a system will also increase the number of applications using GPS technology, such as vehicle navigation, machine control, and atmospheric sensing.

1.3 Problem Statement

Traditional differential GPS positioning systems that are capable of providing centimeter to decimeter accuracy suffer from several drawbacks. These are discussed below.

1.3.1 The Need for Simultaneous Observations at Reference and Rover Stations

At least a pair of GPS stations should be used, including a reference and a rover user receiver. The two GPS stations must be time synchronized and operated simultaneously. The need for a pair of GPS receivers necessitates the use of the same type or compatible GPS receivers at the reference and rover stations as well as the need for field workers at both rover and reference GPS stations. These constraints increase the cost and the logistical complexity of the DGPS positioning process.

1.3.2 The Need to Work in the Vicinity of the Reference Station

To mitigate the GPS errors at the rover station, users have to know the values of these errors at the reference stations and apply them to the rover GPS station in the form of corrections. For these corrections to be representative of the errors at the rover receiver, a strong spatial correlation between the two sets of errors at the reference(s) and the rover GPS receiver stations must exist. Thus, the rover GPS should be within close distance to the GPS reference station(s) (Grewal, 2001). As a rover GPS station moves further away from its GPS reference stations, the correlation of GPS errors degrades and the corrections at the base stations cannot represent the errors at the rover GPS station.

Therefore, unaccounted errors from atmosphere and orbits will degrade the rover position solutions (Roulston et al.., 2000). For a DGPS to be effective, the separation between the rover and reference stations in the case of Real Time Kinematic (RTK) is required to be less than 20 km (Fortez, 2002; Hofmann, 2001), while in the case of network-based RTK the separation could allow up to 50 km (Seeber, 2000). This requirement imposes a limitation on the distance which the GPS rover station can travel.

1.3.3 Inconsistency of Reference Frame

Because the differential corrections are generated from a reference or a network of reference stations, the position solutions obtained at the GPS rover stations refer to the reference frame defined by those GPS reference stations. Therefore, any errors in the GPS reference station coordinates will directly propagate into the GPS rover station coordinates. With the use of different GPS reference stations as is the case of the current practice of DGPS positioning, the position solutions may be inconsistent if the user switches between several reference stations with different accuracies. Therefore, DGPS users should ensure that all the used GPS reference stations are consistent in terms of accuracies and reference frames.

With precise ephemerides and satellite clock corrections become available from IGS and several other organizations, it is possible to remove uncertainties caused by orbit and clock. In addition, with the use of dual frequency GPS observations, ionospheric delays can be mitigated. By mitigating all major GPS error sources, the most precise observations, i.e. carrier phase, can be used in the form of un-differenced observations.

These facts can be used directly in positioning to conduct high precision absolute positioning without the need to difference simultaneous observations from reference and rover stations.

1.4 Research Objectives

The major objectives of this thesis are, first, to develop methods and algorithms for precise point positioning using un-differenced code and carrier phase observations with decimeter and centimeter positioning accuracy; and, second, to analyze the developed PPP system and its value-added products that may arise. To achieve the major objectives, the following minor tasks will be addressed:

- Investigate and Develop Methods to Mitigate Significant Errors

- Investigate a Suitable Observation Model for PPP

- Investigate and Develop an Efficient Processing Method for PPP

- Investigate and Provide an Assessment to PPP Value Added Products

1.5 Thesis Outline

Chapter 1 presents the introduction, problem statement, and thesis objectives.

Chapter 2 discusses current GPS developments, positioning techniques, error sources and mitigations. In addition, the chapter covers the concept of precise point positioning, precise orbit and clock product providers, accuracy and challenges in PPP.

Chapter 3 provides the details of precise point positioning. Error mitigations are the key for highly precise navigations. This chapter presents all PPP related errors and their mitigation models and strategies. These error sources include standard GPS errors and those errors specific to the PPP techniques.

Chapter 4 deals with the function and stochastic models that are used in PPP. It presents both the traditional and the University of Calgary (UofC) processing model.

Chapter 5 aggregates the concepts and method of precise point positioning through investigating the positioning accuracy under different states of dynamics. The results are presented along with the analysis.

Chapter 6 deals with different aspects of PPP, such as the carrier phase non-zero initial phase, convergence, effect of precise data types, and ambiguity equivalence in PPP models.

Chapter 7 presents two interesting value added products: the tropospheric and ionospheric delays. The accuracy of PPP based troposphere delay estimation is investigated and analyzed with respect to IGS as well as Water Vapor Profiler (WVP) data.

Chapter 8 summarizes the main conclusions and recommendations of this thesis.

CHAPTER 2

NAVIGATION AND POSITIONING USING GPS

2.1 Introduction

Navigation and Positioning is the art of determining position, speed, and orientations of an object. This art has been evolving since the beginning of human creation. Navigation systems take many forms, varying from simple forms like lighthouses, compasses, and stars to more modern ones like artificial satellites. GPS is a satellite-based system that provides signals that can be acquired and processed by users to provide positioning parameters and time. Satellite-based navigation techniques started as early as the 1970s. The first system was the U.S. Navy Navigation Satellite System, known as Transit, which uses the principle of the measurement of the Doppler Shift. Two modified versions of Transit were developed: namely, Timation and 621B (Parkinson, 1996). Later, in 1978, GPS was introduced. Since then, it has become the backbone of a whole body of navigation and positioning systems.

This chapter presents current GPS development, positioning techniques, error sources and mitigations. In addition, it presents the concept of precise point positioning, enabling organization, accuracy, and challenges.

2.2 GPS System

The original design of the Global Positioning System consists of 24 satellites orbiting the Earth at an altitude of about 20,000 km. The satellites are distributed in six equally spaced orbit planes of inclination of 55 degrees with respect to the equator. Each satellite circulates the earth in a period of 12 hours sidereal time. In addition, the satellite sends timed signals at two L-band frequencies, 1.57542 and 1.2276GHz, namely L1 and L2. The signals contain codes that identify each satellite, time of the emitted signal, position, satellite clock corrections of the satellite, and other data related to ionosphere and satellite. The L1 signals carry a Coarse/Acquisition (C/A) code, which is available for civilian use, and a more precise P(Y) code, which is available for authorized users. The L2 signals, in contrast, carry the precise P(Y) code, which is available only for authorized users. The C/A-code has a unique sequence of 1023 chips with a width of 300m and repeats every 1 ms. The P-code is extremely long ($\sim10^{14}$chips) but with a smaller chip width, 30m, and repeats itself every one week. High quality receivers use several techniques such as squaring and cross correlation to acquire the P code on L1 and L2 but with noisier characteristics compared with the original codes (Hoffmann et al.., 2001).

The crucial issue in GPS positioning is to observe the time difference between the satellites and users; therefore, high quality redundant atomic clocks are used onboard GPS satellites. The Control Segment is responsible for maintaining the satellites in orbits, adjusting satellite clocks, and uploading navigation data. The control segment consists of five monitoring stations, four ground antenna upload stations, and the Master operational control center as shown in Figure 2.1 (FAA, 2004).
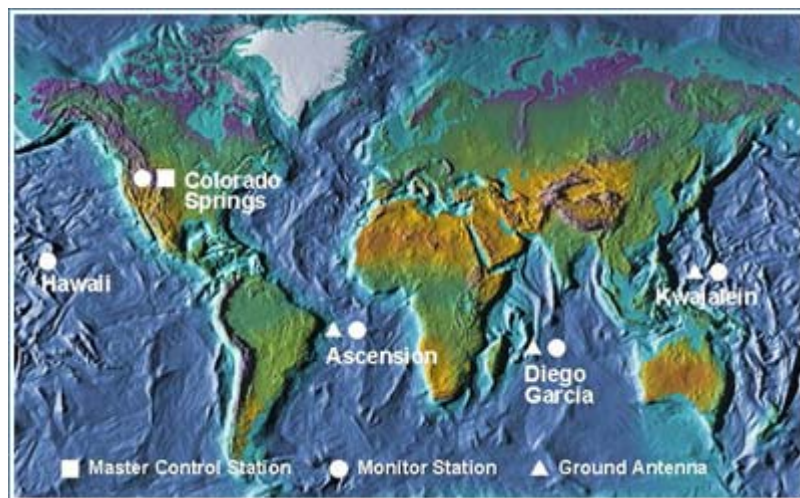
Figure 2.1 GPS control segment (FAA, 2004)

In November 2004, GPS constellations consisted of 30 satellites, divided into three groups: 2 Block II, 16 Block IIA, and 12 Block IIR. The major characteristics of each Block are shown in Table 2.1 (USNO, 2004).

Table 2.1 GPS Block characteristics (USNO, 2004)

Block	Manufacture	No. of operational satellites	Max days of operation without contact from control segment	Launching dates	PRN number	Design Life	Onboard Clock
II	Rockwell International	2	14 days	Feb 1989 through Oct 1990	13 - 21	7.3 years	2 Cesium + 2 Rubidium
IIA	Rockwell International	16	180 days	Nov. 1990 through Nov. 1997	22 - 40	7.3 years	2 Cesium + 2 Rubidium
IIR	Lockheed Martin	12	up to 180 days	From Jan. 1997	41 - 62	7.8 years	3 Rubidium

2.3 GPS Modernization

To increase the precision navigation worldwide, to reduce interference, and to be competitive with the emerging satellite navigation system, Galileo, the USA initiated an ambitious plan for GPS modernization. The plan consists of two steps. The first includes adding a new C/A code on L2, a new Military code (M) on L1 and L2, and increasing the signals' power. The second step includes adding a new civilian signal on a new frequency 1176.45 Mhz (L5). The first step will be applicable to some of the IIR satellites that are being launched and are anticipated to operate in 2008. Some of these satellites are already in orbit, but the expected operation capabilities will start in 2008. The second stage of modernization is expected to operate in 2012. Figure 2.2 depicts a summary of the modernization process (Sandhoo et al., 2000).
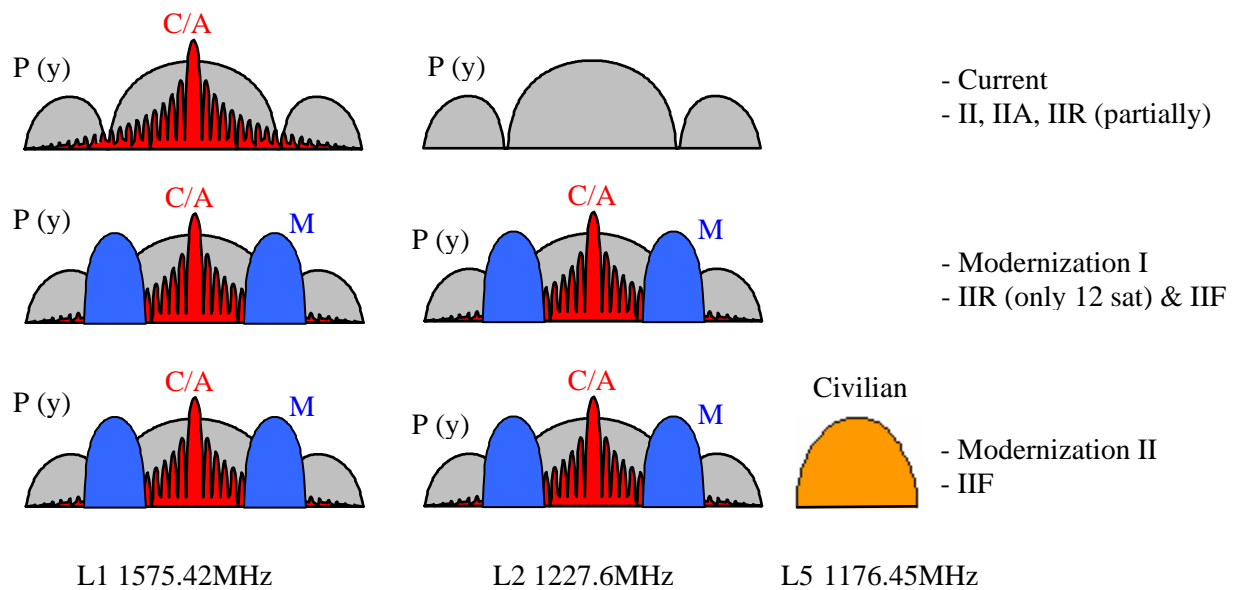
Figure 2.2 GPS signals' modernization plan

2.4 Positioning Techniques

Autonomous point positioning or Standard Positioning Service (SPS) is vulnerable to the effect caused by all GPS related errors. Examples for these errors are the uncertainty in satellite orbit and clock; atmosphere propagation effects such as ionosphere and troposphere delay; site belongings such as multipath, and receiver performance such as noise. Table 2.2 depicts the common magnitude of each error. Because of these shortcomings, autonomous or standard point positioning can support positioning accuracy only at the level of several meters. Several positioning techniques have been developed to overcome the existence of these errors and to obtain higher positional accuracy. These methods include code-based Differential GPS; carrier phase-based differential GPS;

Dynamic Ambiguity Real Time Standalone (DARTS); and, recently, Precise Point Positioning. The following sections give a brief overview of each technique.

Table 2.2 GPS Error Budget (Misra and Enge, 2001)

Common Error Source	Error size
Satellite orbit	≈ 2 m
Satellite clock	≈ 2 m
Ionospheric delay	$\approx 2\text{-}10$ m at zenith
Tropospheric delay	$\approx 2.3\text{-}2.5$ m at zenith
Multipath	In a clean environment Code: 0.5-1 m Carrier: 0.5-1 cm
Receiver Noise	Code: 0.25-0.5 m for code Carrier phase: 1-2 mm for carrier phase

2.4.1 Code-based Differential GPS Methods

The idea behind code-based differential GPS techniques is to make use of spatial correlations to remove the common errors between base and rover stations. These techniques can take several forms depending on the type of processing methods such as position, observations, or state space approach; and the coverage of the system which can be local, regional, or global.

2.4.1.1 Local Area Differential GPS

In local area differential GPS, a reference receiver with known coordinates is operated simultaneously with a nearby rover receiver. By knowing the coordinates of the reference

receiver, a scalar correction representing all GPS range errors can be calculated and be sent to the rover receiver to be applied. This scalar correction can be a range or position. The user should be within the vicinity of the reference station to ensure that these received corrections really represent the errors he or she suffered from. Another version of local code DGPS is to broadcast the reference GPS station measurements to the rover GPS station where differencing of the measurements is applied. In general, these techniques can alleviate the effect of GPS errors, but, as the separation between the reference and rover stations increases, the errors' correlation between the rover and base stations decreases.

2.4.1.2 Wide Area Differential GPS

Unlike the local area differential GPS method, the wide area differential GPS uses a network of GPS receivers' stations with known coordinates that operate simultaneously to model each GPS error separately. Thus, the correction of Wide Area Differential GPS is given in a state-space domain (Abousalem, 1995). This system is capable of covering large areas compared with the local area differential GPS and has the capability of producing sub meter positional accuracy. Examples of these systems are the Wide Area Augmentation System (WAAS) at USA, MTSAT Satellite Augmentation System (MSAS) at Japan, and European Geostationary Navigation Overlay Service (EGNOS) at Europe as shown in Figure 2.3 (TrackLog, 2004).
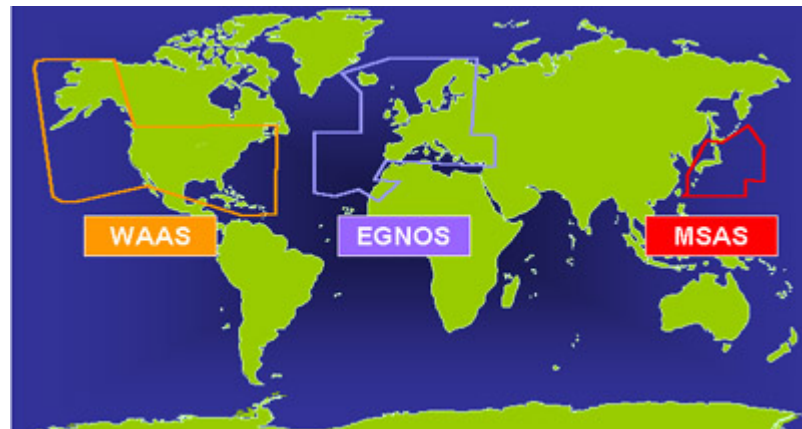
Figure 2.3 Existing wide area differential GPS (TrackLog, 2004)

2.4.2 Carrier Phase-based Differential GPS Methods

In contrast to the code-based differential GPS, the carrier phase-based differential GPS is capable of achieving higher positioning accuracy from the high precision of carrier phase observations. It can be categorized according to the coverage area or the number of the GPS reference stations that are used to support the GPS rover station. The following two sections summarize the different concepts of carrier phase based differential GPS methods.

2.4.2.1 Local Area Real Time Kinematic (RTK)

Similar to local DGPS, a reference station with a known position can transmit either its observations or its corrections to a rover GPS station. The data transmission process can be done through the RTCM message 18/19 or 20/21 (Neumann et al., 1999). The role of the rover station is to resolve the integer ambiguity to get a highly instantaneous accurate positioning solution. The case of using RTCM message 18/19 is the same as the case of

using relative processing of carrier phase observations, whereas in the case of using RTCM message 20/21, the rate of change of the base station observation is used. It is worth mentioning that RTK can produce positional accuracy of centimeter level for the case of baselines with a length less than 20 km.

2.4.2.2 Network RTK

With the popularity and availability of many ground reference stations, a correction vector that represents GPS errors can be generated. Each component of the correction vector corresponds to a unique error source. Users within the vicinity of these networks of reference stations can use these corrections to correct the rover observations and get an accurate position solution. The merit of this method is that a lower number of base stations are needed over large areas compared with local RTK (Rizos, 2002). Several RTK networks have been implemented around the world. Examples of these networks are in Norway, Japan, and Italy.

2.4.3 Dynamic Ambiguity Real Time Standalone (DARTS) Method

The Dynamic Ambiguity Real Time Standalone (DARTS) method has been recently proposed by Simsky (2003) at Septentrio Inc. Processing un-differenced code and carrier phase observations along with the broadcast satellite orbit and clock is usually inefficient because of the large uncertainty of the broadcast satellite orbit and clock data. To overcome the uncertainty problem, the ambiguities bias can be modeled as a dynamic variable rather than a constant. For this purpose, the system noise can be optimized to

allow the absorption of orbit and clock errors. The advantage of this method is that standalone receivers can be used without any type of corrections, but the accuracy that can be obtained from this method is similar to the GPS code-based differential techniques. The technique has been implemented in dual frequency GPS receivers developed at Septentrio Inc.

2.4.4 Precise Point Positioning

The International GPS Service (IGS) is a civilian organization, which emerged from the International Association of Geodesy (IAG). It operates a global network of high quality dual frequency GPS stations to support geodetic and geophysical research. IGS takes the responsibility of providing GPS orbit, GPS data, earth rotation parameters, troposphere delay, and global ionosphere map.

With the advent of precise ephemeredes and satellite clock corrections from IGS and several other organizations, it is possible to conduct high precision GPS positioning without the need to difference simultaneous observations of reference and rover stations. As a result, only a single receiver is needed, and the positioning process can be carried out with high confidence based on the assumption that the space segment errors are mitigated. Moreover, the proper use of carrier phase observations as the primary observable can lead to decimeter or centimeter positional accuracy. This positioning method that uses un-differenced code and carrier phase observations is known as "precise point positioning". Some research results on positioning using un-differenced code and carrier phase observations have been described in Witchayangkoon (2000), Abdel-salam

et al. (2002); Bisnath and Langley (2001); Collins et al. (2001); Han et al. (2002); Lundberg et al. (2001); Muellerschoen et al. (2000); Muellerschoen (2001); Ovstedal et al. (2002); Zumberge et al. (1997); Zumberge et al. (2001); Gao and Shen, (2001). Some of these are described below.

Precise Point Positioning using un-differenced code and carrier phase observations from dual frequency receivers was proposed by Zumberge et al. (1998; 1997) as well as Kouba and Heroux (2000). In 1997, during the Selective Availability era, IGS produced precise orbit and satellite clock corrections, but, because of SA, it was impossible to interpolate these corrections over short intervals without a severe degradation of accuracy. Zumberge et al. (1997) suggested a method for calculating the orbit and clock data at small intervals using a subset of the IGS network. Afterward, they used these precise data in post processing software to calculate user station coordinates along with other parameters such as the tropospheric delay. Precise data with intervals of 30 and 900 seconds were used for clock and orbit, respectively. Promising results were obtained based on their technique.

Kouba and Heroux (2000) were the first to publish in detail the technique of using un-differenced code and carrier phase observations from dual frequency receivers. They emphasized error mitigations especially those related to the un-differenced code and carrier phase observations. Using GPS data at intervals of 30 seconds, the unknown parameters were estimated at 15 minute intervals, the interval of final IGS precise data. Comparable results to Zumberge's were obtained.

Later, as a continuous work at JPL, Muellerschoen et al. (2000) developed a system for precise point positioning for dual frequency receivers. JPL operates a global network of GPS stations, which transmit GPS data to JPL in real time over the Internet. JPL then calculates the corrections corresponding to the broadcast orbit and satellite clock corrections. These corrections are then transferred to the users through the Internet. Also, JPL is planning to broadcast these corrections through satellites. JPL reported 8 cm RMS accuracy in horizontal and 20 cm RMS accuracy in vertical (IGDG, 2004). Like JPL, the Natural Resources of Canada is operating a network of GPS stations all over Canada and uses them to produce real time satellite orbit and clock corrections. These corrections are available through the Internet and the Canadian MSAT communication satellite (Lochhead et al., 2002). With world wide reference stations, the JPL precise data enjoys better accuracy.

The previous research work was obtained from using the observation model, which uses the ionosphere free pseudo-code and carrier phase combinations. The unknowns include one float ambiguity term for each satellite in addition to a position, a receiver clock bias, and an atmosphere parameter. Gao and Shen (2001) introduced a different observation model that uses an averaged pseudo-code and carrier phase observations on the two GPS frequencies in addition to the ionosphere free carrier phase combination. The model allows for the estimation of two float ambiguities for each satellite in addition to station parameters, receiver clock, and troposphere delay. Moreover, they introduced a new technique for resolving the float ambiguities, which is known as "pseudo-fixing".

In addition to these academic research works, several commercial organizations are paying much attention to this technique. Examples of these are the NAVCOM StarFire and Omnistar-HP systems (Bisnath et al., 2003).

2.4.5 Pros and Cons

The previous section provided an overview of the existing GPS position techniques. A limitation exists for local DGPS systems in terms of fast degradation with the increase of rover reference separation. Regional systems such as WADGPS or network RTK necessitate that the users must work in the vicinity of reference stations and need an expensive infrastructure. Although DARTS is an attractive global positional technique, it cannot achieve decimeter or centimeter positioning accuracy. Therefore, PPP is the only global technique that can provide high accuracy and does not need the deployment of dense reference station(s). A summary of the differences is illustrated in Table 2.3.

Table 2.3 GPS positioning techniques characteristics

Service Type	Coverage	Accuracy
Autonomous Point Positioning	Global	Several meters
Code Based DGPS	Local & wide area	Meter level
Carrier Phase Based DGPS	Local & wide area	Centimeter to decimeters
DARTS	Global	Sub meter level
PPP	Global	Centimeter to decimeter level

CHAPTER 3

ERROR SOURCES AND MITIGATION IN PRECISE POINT POSITIONING

3.1 Introduction

The key point for precise positioning and navigation is the ability to mitigate all potential error sources in the system. As a result of the un-differenced nature of PPP, all errors caused by space segment, propagation, environment, and receiver need to be mitigated. The mitigation can be carried out by modeling, estimation, or observation combination. Most of the PPP errors, except for troposphere, receiver clock, and ionospheric delay, can to some extent be mitigated through modeling. The receiver clock error and troposphere delay can be mitigated by estimation, while ionospheric delay can be mitigated by observations combination.

This chapter presents the PPP errors' mitigation strategy. The errors are classified into two groups: traditional and specific to precise point positioning. Also, the chapter depicts the reference frame considerations.

3.2 Traditional GPS Error Survey

Traditional GPS error sources are those affecting the standard positioning service and, to a lesser extent, the differential GPS systems. These errors include satellite orbit and clock, troposphere and ionospheric delay, Sagnac, relativity, receiver and satellite phase offset, multipath and noise.

3.2.1 Satellite Ephemeris and Clock Errors

Errors associated with satellite vehicle are uncertainties in ephemeris and satellite clock corrections. The magnitudes of these errors are about 2 m for ephemeris and 7 ns for clock correction (IGS, 2004); however, large values may be observed (Roulston et al., 2000). The effect of this error depends on the type of the GPS processing technique that is being used. In the differential positioning system, orbit errors will affect the solution with the increase of the separation between reference and rover GPS stations. In contrast to the orbit error, there is no baseline dependent component for the satellite clock correction (Parkinson et al., 1996). With the emergence of global GPS station networks, the GPS orbit and clock can be estimated with high accuracy. IGS provides GPS orbit and clock in different latencies and accuracies as shown in Table 3.1 (IGS, 2004). The clock corrections shown at 30 second intervals is not an official IGS product but is produced by the CODE analysis center at Bern University (IGSmail#4913, 2004). By using these precise data, the uncertainty in orbit and clock can be significantly reduced.

Table 3.1 IGS products (IGS, 2004)

Data	Accuracy		Latency	Interval	
	Orbit	Clock		Orbit	Clock
Final	< 5 cm	~ 0.1ns	~ 13 days	15 minutes	15 minutes
					5 minutes
					30* second
Rapid	< 5 cm	~ 0.1 ns	~ 17 hours	15 minutes	5 minutes
					30* second
Ultra rapid (observed)	< 5cm	~ 0.2 ns	~ 3 hours	15 minutes	15 minutes
Ultra rapid (predicted)	~10 cm	~ 5 ns	Real time	15 minutes	15 minutes

Not official IGS product

3.2.2 Troposphere Delay

Troposphere is the lower layer of atmosphere, extending from the sea level up to about 40 km (Hofmann, 2001). It is a non-dispersive medium; therefore, the delay from troposphere is invariant to GPS signals' frequencies. The troposphere effect can be divided into wet and dry components. The wet component is caused by the lower portion of troposphere, 11 km from sea level, and it contains most of the water vapor. Because of the variation of water vapor density with position and time, the modeling of the wet component is difficult. The wet component represents 10% of the total troposphere delay (Misra and Enge, 2001).

Unlike the wet component, the dry component is the higher portion of atmosphere lying directly above the wet components, and containing mainly gases. It represents the remaining 90% of the troposphere and can be easily modeled. The average total

troposphere delay at zenith is about 2.5 m, and it changes but does not suffer much from rapid change or large variation. The dry and wet troposphere delays are usually modeled at zenith and then mapped, using a mapping function to the satellite elevation as shown in Equation 3.1.

$$\Delta_{\text{Trop}} = \Delta_{\text{wet}} \, M_{\text{wet}} + \Delta_{\text{dry}} \, M_{\text{dry}} \qquad (3.1)$$

where,

Δ_{wet} - the zenith wet component

Δ_{dry} - the zenith dry component

M_{wet} - the wet mapping function

M_{dry} - the dry mapping function

Different models and mapping functions based on theoretical or practical data are in use. Troposphere models include Saastamoinen, Hopfield, and Black-Eisner, while mapping functions include Davis, Chao, Marini and Niell (Mendes and Langely, 1994). An example of these models is the Hopfield model. It is an empirical model for zenith wet and dry tropospheric delay components obtained on the basis of extensive measurements. Hopfield model depends on temperature, pressure, and humidity. The models for zenith wet and dry troposphere delays are shown in Equations 3.2 and 3.3, respectively (Spilker, 1996).

$$Trop_{WZTD} = 7.46512 \times 10^{-2} \times (\frac{e}{T_k^2}) \times h_w \qquad (3.2)$$

$$Trop_{DZTD} = 1.552 \times 10^{-5} \times (\frac{P}{T_k}) \times h_d \qquad (3.3)$$

where

P — atmosphere pressure in mbar

T_k — temperature in Kelvin

e — parameter derived using humidity

h_w — dry tropospheric height ($\approx$ 43 km)

h_d — wet tropospheric height ($\approx$ 12 km)

An example of mapping function that reduces the tropospheric delay from the zenith to an arbitrary elevation angle is the Niell Mapping function. It is an empirical function that depends on the latitude and time of the station. It has different forms for wet and dry troposphere delays. The wet mapping function is shown in Equations 3.4 (Leick, 2004).

$$M_{Wet} = \frac{1 + \dfrac{a}{1 + \dfrac{b}{1+c}}}{\sin(E) + \dfrac{a}{\sin(E) + \dfrac{b}{\sin(E) + c}}} \tag{3.4}$$

where

E — Elevation angle

a, b, and c — coefficients depend on the station latitude

According to (Leick, 2004), the dry mapping functions takes more complex form compared to the wet mapping function as shown in Equation 3.5. The coefficients of the wet and dry mapping functions are given in Appendix A.

$$M_{Dry} = \frac{1 + \dfrac{a}{1 + \dfrac{b}{1 + c}}}{\sin(E) + \dfrac{a}{\sin(E) + \dfrac{b}{\sin(E) + c}}} + h \cdot \left(\frac{1}{\sin(E)} - \frac{1 + \dfrac{a_h}{1 + \dfrac{b_h}{1 + c_h}}}{\sin(E) + \dfrac{a_h}{\sin(E) + \dfrac{a_h}{\sin(E) + \dfrac{b_h}{\sin(E) + c_h}}}} \right)$$

(3.5)

where

$$a(\phi, DOY) = \tilde{a} - a_p \cos(2\Pi \frac{DOY - DOY_0}{365.25})$$ (3.6)

$$b(\phi, DOY) = \tilde{b} - b_p \cos(2\Pi \frac{DOY - DOY_0}{365.25})$$ (3.7)

$$c(\phi, DOY) = \tilde{c} - c_p \cos(2\Pi \frac{DOY - DOY_0}{365.25})$$ (3.8)

E - elevation angle

$\tilde{a}, \tilde{b}, \tilde{b}$ - coefficients depend on the station latitude

a_p, b_p, c_p - coefficients depend on the station latitude

a_h, b_h, c_h - coefficients depend on the station latitude

DOY - Day Of year

DOY_0 - constant equals to 28 or 211 for stations at the north and south of the equator, respectively

h - station height above sea level

Π - Pi =3.14159265.

3.2.3 Ionospheric Delay

The ionosphere layer is the higher stratum of the atmosphere with an extension from about 40 to 1000 km. The ionosphere contains ionized particles created by the sun's ultraviolet radiation. Unlike the troposphere, the ionosphere is a dispersive medium causing different delays for the L1 and L2 frequencies. The zenith magnitude of the delay caused by the ionosphere is larger than the one caused by the troposphere and can reach tens of meters. As a consequence of solar activities, ionospheric delays can change significantly in both the short and long terms. Moreover, diverse characteristics exist depending on the geographic regions (Skone, 2000; Afraimovich et al., 2002). The density of the ionized particles differs with the height profile and can be illustrated as five layers: H, F2, F1, E and D. The properties of each layer are shown in Table 3.2 (Klobuchar, 1996).

Table 3.2 Ionosphere layers

Layer	Height (km)	Characteristics	Contribution
D	50 - 90	Caused by hard x rays	negligible
E	90 - 140	Caused by solar soft x rays	minimal
F1	140 - 210	Caused by ionization of molecular species Region of the aurora and scintillation	10%
F2	210 -1000	Caused by ionized atomic oxygen	80 - 40%
H^+	>1000	Caused by ionized hydrogen Place of major magnetic storm	10 - 50%

One characteristic of the ionosphere is that it advances the carrier phase but delays code observations. Single frequency GPS users can use ionosphere models to alleviate its effect. Among these models are Chiu, Bent, semi-empirical SLIM, FAIM, and the International Reference Ionosphere (IRI) models (Cander et al., 1999). For dual frequency GPS receivers, the absolute ionospheric delay can be calculated from code observations, whereas a more accurate estimate but relative can be derived from carrier phase observations. The expressions for calculating absolute and relative ionospheric delay on L1 and L2 are depicted in Equations 3.9 and 3.10 for code observations and in 3.11 and 3.12 for carrier phase observations (Skone, 2001).

$$\frac{40.3}{f_1^2}TEC = \frac{f_2^2}{f_1^2 - f_2^2}(P_1 - P_2 - (1 - \frac{f_1^2}{f_2^2})cT_{GD,r} + (1 - \frac{f_1^2}{f_2^2})cT_{GD,s})$$ (3.9)

$$\frac{40.3}{f_2^2}TEC = \frac{f_1^2}{f_1^2 - f_2^2}(P_1 - P_2 - (1 - \frac{f_1^2}{f_2^2})cT_{GD,r} + (1 - \frac{f_1^2}{f_2^2})cT_{GD,s})$$ (3.10)

$$\frac{40.3}{f_1^2}TEC = \frac{f_2^2}{f_1^2 - f_2^2}(\Phi_1 + N_1\lambda_1 - \Phi_2 - N_2\lambda_2 + (1 - \frac{f_1^2}{f_2^2})cT'_{GD,r} - (1 - \frac{f_1^2}{f_2^2})cT'_{GD,s})$$ (3.11)

$$\frac{40.3}{f_2^2}TEC = \frac{f_1^2}{f_1^2 - f_2^2}(\Phi_1 + N_1\lambda_1 - \Phi_2 - N_2\lambda_2 + (1 - \frac{f_1^2}{f_2^2})cT'_{GD,r} - (1 - \frac{f_1^2}{f_2^2})cT'_{GD,s})$$ (3.12)

where,

TEC - the total electron content (el/m^2)

P_1, P_2 - the measured pseudorange on L1 and L2 (m)

Φ_1, Φ_2 - the measured carrier phase range on L1 and L2 (m)

c - the speed of light (m/s)

λ_1, λ_2 - the wavelength on Li (m)

$T_{GD,s}$, $T'_{GD,s}$ - the satellite interfrequency bias in code and carrier phase measurements

(s)

$T_{GD,r}$, $T'_{GD,r}$ - the receiver interfrequency bias in code and carrier phase measurements

(s)

3.2.4 Sagnac

The Sagnac effect arises from the rotation of the Earth during the GPS signal propagation. The Sagnac effect is a correction for adapting the dilation of time caused to a clock carried by a rotating object on non inertial frames (Ashby and Spilker, 1997). According to Ashby and Spilker, this correction can be estimated from Equation (3.13) or can be considered through iterating the solution of the propagation delay. The latter solution can be obtained through rotating the receiver coordinates around the z axis by the amount of earth rotation during the propagation time until no remarkable change in coordinates is observed. Then, the correction can be estimated as the difference between the original range and the one obtained from the transformation.

$$\Delta t_{Sagnac} = -\frac{\vec{r}_r^{\,s} \bullet \vec{v}_r^{\,s}}{c^2} \tag{3.13}$$

where,

$\vec{r}_r^{\,s}$ - Receiver to satellite position vector

$\vec{v}_r$ - Receiver to satellite velocity vector

c - Speed of light

$\bullet$ - Dot product

3.2.5 Relativity

The concept of satellite ranging systems is based on observing the time difference between the satellites and recipients. Two factors affect the concept of time: gravity and motion of the satellite. The satellite clock is subjected to the force of the Earth gravity, which is less than the forces at the user's side. This phenomenon is known as "general relativity". The satellite clock will run faster than the receiver clock; therefore, a correction should be considered. Another phenomena related to the clock is that a moving clock tends to be slower than one at rest or one moving slower. The previous reason would cause a constant frequency offset that can be interpreted as a distance; however, because of the near circular orbit of the GPS satellite, the effect of relativity will be periodic and can be given in Equation 3.14 (ICD-GPS-200, 2000). Moreover to the clock effect, the earth gravity field causes delay for GPS signals. The correction term is given in Equation 3.15 (Rothacher and Beutler, 2002).

$$\Delta t_r = -\frac{2\vec{r}^s \bullet \vec{v}^s}{c^2} \tag{3.14}$$

$$\Delta t_p = \frac{2GM_E}{c^2} \ln(\frac{r^s + r_r + r_r^s}{r^s + r_r - r_r^s}) \tag{3.15}$$

where all coordinates are in the earth centered inertial frame and

Δt_r - Relativity correction

Δt_p - Gravity delay error

$\vec{r}^s$ - Satellite position vector

$\vec{v}^s$ - Satellite velocity vector

r^s - Distance between the satellite and earth center

r_r - Distance between the receiver and earth center

r_r^s - Distance from the receiver to satellite

c - Speed of light

G - Gravitational constant

M_E - Mass of the earth

$\bullet$ - Dot product

3.2.6 Receiver Antenna Phase Center

The measurements of GPS receivers refer to the electronic center of the antenna. A receiver's Antenna Phase Center is not a physical mark that GPS users can refer to. In addition, it changes according to the elevation of the incoming GPS signals, and this variation is a function of the antenna fabrication. As a result, every GPS antenna will have an offset in addition to a variable element because of the elevation angle of the satellite. This error must be corrected; otherwise, an error that can reach a decimeter would be unaccounted for (Mader, 1999; 2001). Several methods exist for the calibration of receiver antennas to determine the electronic center of the antenna. Among these methods are relative, robot, and chamber calibrations (Mader, 1999; Mader, 2001; Schmitz et al., 2002; Schupler and Clark, 2001; Leick, 2004). Currently, the offset and the variation at an elevation angle's interval of 5 degrees are available from IGS and the US National Geodetic Survey (NGS). GPS users can interpolate the available antenna phase center variation values to get the corresponding values at any arbitrary elevation.

3.2.7 Multipath and Noise

Multipath and noise affect code severely compared to carrier phase observations. The effect of multipath can reach tens of meters for code observations in contrary to only a few centimeters for carrier phase observations. Several techniques for the mitigation can be applied, such as narrow correlator, multiple antenna system, chocke ring antenna, or estimation (Cannon et al., 2001; 2001a). Noise has similar effect to multipath; however, the amplitude of noise is smaller. The noise levels can reach decimeter levels for code observations and a few mm for carrier phase observations.

3.3 Special GPS Error Sources

There are several GPS related errors that have attracted only trivial attention from the GPS community. The reasons were that the values of these errors are small with respect to the affordable GPS positional accuracy or these errors can be canceled in the case of differential GPS processing. However, owing to the un-differencing nature and the high positioning accuracy of PPP, these errors must be considered; otherwise, erroneous results will be obtained. The following section describes these errors.

3.3.1 Satellite Antenna Phase Center Offset

GPS satellites carry onboard antenna that broadcast its signals; thus, all measurements refer to the antenna electronic phase center. This is the case for broadcast ephemeredes. Different from this case is the IGS precise orbit. The IGS uses dynamic modeling for

estimating the GPS orbit; therefore, the resulting orbital data refers to the center of mass, not the electronic phase of the antenna as shown in Figure 3.1. The effect of this separation is twofold. Users interested in estimating satellite clock corrections will have an erroneous clock product if not considering it. In addition, GPS users not paying attention to it will get an imperfect station height (Zhu et al., 2002).
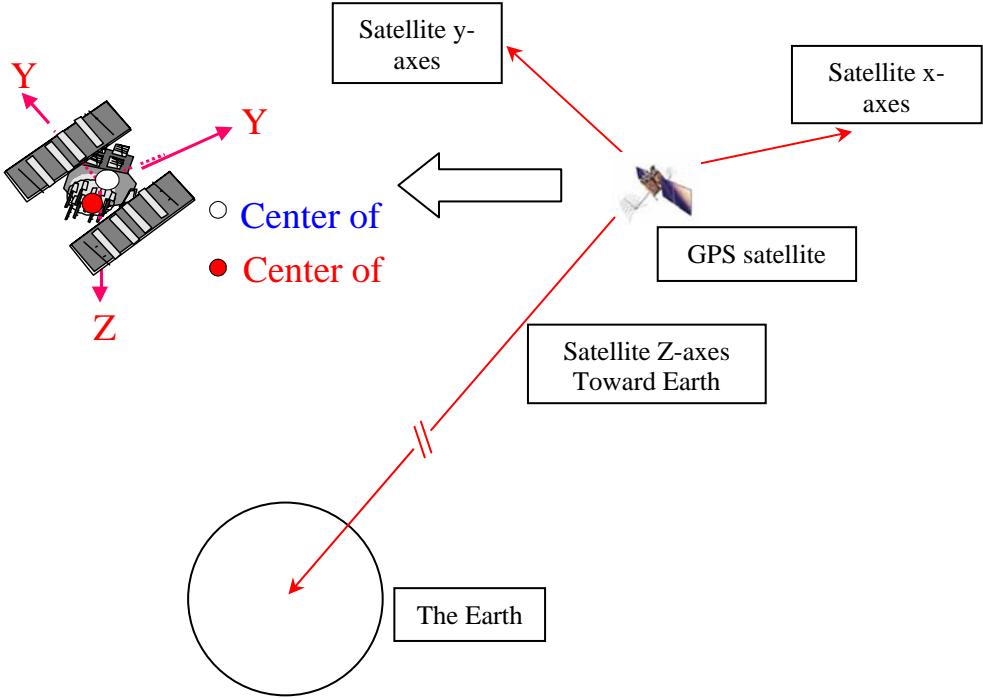
Figure 3.1 Satellite antenna phase center offset

The separation between the two centers depends mainly on the satellite design. This separation is located in two directions. The first direction is the Z, which is the direction of a vector passing through the satellite center of mass and the Earth; the second is the direction of the vector joining the Sun and the satellite center of mass (Kouba and Heroux, 2000). The known values for this offset are uncertain, but for the sake of clock

product consistency, several standardized values at the ionosphere-free frequency are used for each satellite or satellite block as shown in Table 3.3.

Table 3.3 Satellite antenna phase offset values given by NGA

Block	PRN	Delta-x (m)	Delta-y (m)	Delta-z (m)
II	All	0.2794	0	0.9519
IIA	All	0.2794	0	0.9519
IIR	PRN 11	0.0019	0.0011	1.5141
IIR	PRN 13	0.0024	0.0025	1.6140
IIR	PRN 14	0.0018	0.0002	1.6137
IIR	PRN 16	-0.0098	0.0060	1.6630
IIR	PRN 18	-0.0098	0.0060	1.5923
IIR	PRN 19	-0.0100	0.0064	1.5620
IIR	PRN 20	0.0022	0.0014	1.6140
IIR	PRN 21	0.0023	-0.0006	1.5840
IIR	PRN 22	0.0018	-0.0009	0.0598
IIR	PRN 23	0.0088	0.0035	0.0004
IIR	PRN 28	0.0018	0.0007	1.5131

These values are made available by The National Geospatial-Intelligence Agency (NGA, 2004). It is worth mentioning that the values shown in Table 3.3 are different from the values given by Kouba and Heroux (2000) as illustrated in Table 3.4. Moreover, Mader (2001) indicated different offsets based on the GPS frequencies. His research work was based on actual site calibration for a GPS satellite antenna that made available for research purposes. The discrepancy of the satellite antenna phase offset values can be attributed to the difference in the estimation methods and to the difficulty in the estimation process due to the existence of correlation among the orbit radius, station height and zenith tropospheric delay (Zhu et al., 2003; Springer, 2000; Bar-Sever, 1998).

The values in Table 3.4 are used in this thesis because IGS precise data are estimated based on them. The correction of this error is given in Equation 3.16 (Leick, 2004).

$$X_{phase\ center} = X_{center\ of\ mass} + \begin{bmatrix} x & y & z \end{bmatrix}^{-1} X \quad\quad (3.16)$$

where,

$\begin{bmatrix} x & y & z \end{bmatrix}$ - satellite body local unit vector

x - satellite-Sun unit vector in Earth Centered Earth Fixed (ECEF)

z - satellite unit vector toward Earth in ECEF

y - the third vector of x and z which complete the right hand system

X - $\begin{bmatrix} x_{offst} & y_{offst} & z_{offst} \end{bmatrix}^{T}$ Offset in the satellite fixed coordinates system

Table 3.4 Satellite antenna phase center offset

	Delta x (m)	Delta y (m)	Delta z (m)
Block II/IIA	0.279	0	1.023
Block IIR	0	0	0

3.3.2 Phase Wind Up

GPS signals are right circularly polarized (RCP). One property of this type of signal is that any relative rotation between satellite and receiver antennas is interpreted as a change in the line of sight distance. Therefore, when using GPS carrier phase observations, any relative orientation during the observation period must be accounted for through phase wind up correction as given by Equations 3.17, 3.18, and 3.19 (Wu et al., 1993; Leick, 2004). Phase wind up error can reach a phase cycle. It exists even in static surveys because the satellite antenna is always in the state of slow rotation due to the

continuous reorientation of its solar panels toward the Sun. Rapid phase wind up error can occur in the case of an eclipse (Kouba and Heroux, 2000).

$$d = x - k(k \bullet x) - k \times y \tag{3.17}$$

$$\bar{d} = \bar{x} - k(k \bullet \bar{x}) + k \times \bar{y} \tag{3.18}$$

$$\delta\phi = sign(k \bullet (\bar{d} \times d)) \ \cos^{-1}(\frac{d \bullet \bar{d}}{\| d \| \| \bar{d} \|}) \tag{3.19}$$

where

k - the satellite to receiver unit vector

x, y, z - the satellite body local unit vector (as in satellite antenna phase offset)

$\bar{x}, \bar{y}, \bar{z}$ - the receiver local unit vector

$\| \bar{d} \|$ - the magnitude of the vector

$\delta\phi$ - the phase wind up correction

$\bullet$ - the dot product

3.3.3 Earth Tide

The Earth is not a real solid object; as a result, it responds to the gravitational forces imposed by the Sun and the Moon. These gravitational forces cause a decimeter level variation on the Earth's crust. As can be seen in Figure 3.2, the solid earth tide depends on the station location and sidereal time.
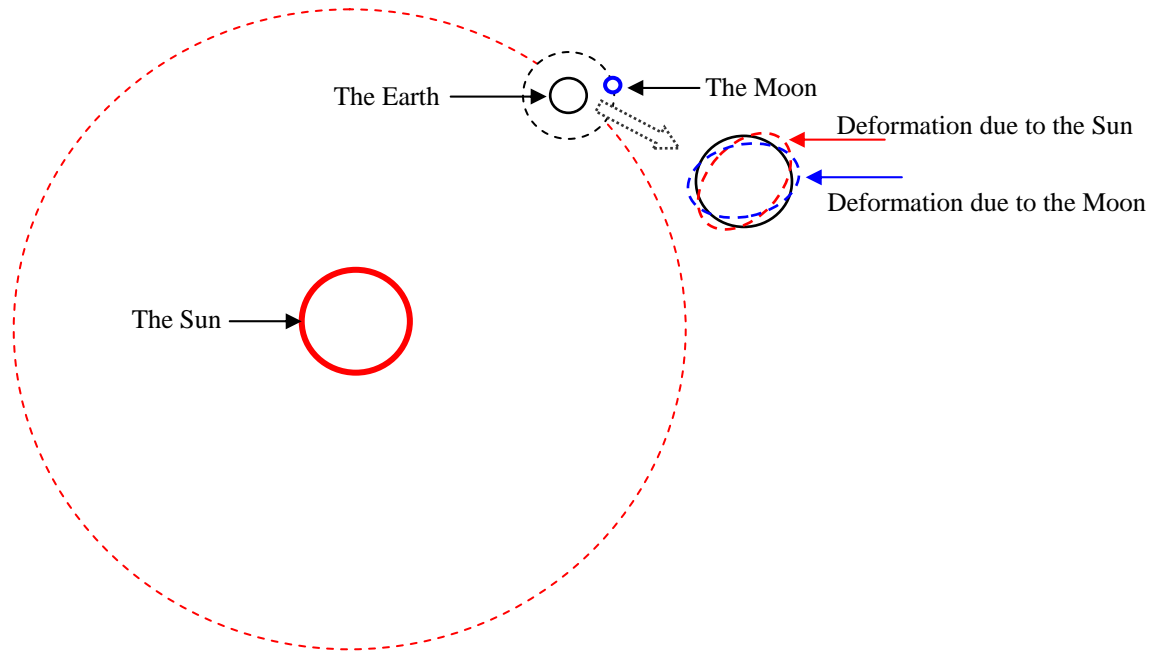
Figure 3.2 Earth, Sun, and Moon interaction

Its effect in the height direction is large and can reach 30 cm, whereas it can reach 5 cm in the horizontal direction. The displacement caused by the solid earth's tide has a permanent component, which can reach 12 cm in mid latitude, and a periodic component, which is characterized with diurnal and semi diurnal trends (Kouba and Heroux, 2001). The solid earth's tide can be modeled with high accuracy. According to McCarthy (1996), the model given in Equation 3.20 is capable of modeling the solid earth's tide with an accuracy of a few mm.

$$\Delta \vec{r} = \sum_{j=2}^{3} \frac{GM_j}{GM} \frac{r^4}{R_j^3} \left\{ \left[3l_2 \left(\widehat{R}_j \cdot \widehat{r} \right) \right] \widehat{R}_j + \left[3 \left(\frac{h_2}{2} - l_2 \right) \left(\widehat{R}_j \cdot \widehat{r} \right)^2 - \frac{h_2}{2} \right] \widehat{r} \right\} +$$

$$\left[-0.025 \cdot \sin \phi \cdot \cos \phi \cdot \sin \left(\theta_g + \lambda \right) \right] \cdot \widehat{r} \tag{3.20}$$

where

GM	- gravitational parameters of the Earth
GM_j	- gravitational parameters of the Moon ($j=2$) and the Sun ($j=3$)
R	- geocentric state vectors of the station
R_j	- geocentric state vectors of the Moon ($j=2$) and the Sun ($j=3$)
$\hat{r}$	- geocentric unit state vectors of the station
$\hat{R}_j$	- geocentric unit state unit vectors of the Moon ($j=2$) and the Sun ($j=3$)
l_2	- nominal second degree Love number (0.609)
h_2	- nominal Shida dimensionless numbers (0.085)
ϕ	- site latitude
λ	- site longitude
θ_g	- Greenwich Mean Sidereal Time

3.3.4 Ocean Tide Loading

Similar to the effect of the Moon and Sun on solid earth, the water in the oceans is in a continuous state of distribution because of the gravitational force. This redistribution imposes a load on the coastal area, which causes a surface displacement that can reach 5 cm in the vertical and 2 cm in the horizontal direction. It is characterized by diurnal and semi diurnal displacement. The model of ocean loading as given by McCarthy (1996) is illustrated in Equation 3.21. The effect of this error is assumed to be negligible when the GPS station is far from ocean coast lines.

$$\Delta x = \sum_j f_j A_{cj} \, cos(\omega_j t + \chi_j + u_j - \Phi_{cj}) \tag{3.21}$$

where

Δx	- displacement due to ocean loading
j	- represents the 11 tidal waves known as $M_2, S_2, N_2, K_2, K_1, O_1, P_1, Q_1, M_f, M_m$

and S_{sa}

f_j - depend on the longitude of lunar node (at 1-3 mm precision $f_j =1$)

u_j - depend on the longitude of lunar node (at 1-3 mm precision $u_j =0$)

ω_j - angular velocity at time $t=0h$

χ_j - astronomical arguments at time $t=0h$

u_j - depend on the longitude of lunar node (at 1-3 mm precision $u_j =0$)

A_{cj} - station specific amplitude

Φ_{cj} - station specific phase

3.3.5 Atmosphere Loading

The atmosphere column weight above the earth's surface causes a load on the earth's surface. This load varies according to the change of atmosphere pressure, causing varied vertical and horizontal displacements. According to Petrov and Boy (2003), these displacements can be as large as 20 mm for the vertical component and 3 mm for the horizontal component. Atmosphere pressure loading displacement is a function of geographic location. It has a large value for mid latitude locations compared with high latitude (McCarthy, 1996). Models for atmosphere pressure loading displacement vary from simple to complex. A simple model is presented by Rabbel and Schul (1986) as given by Equation 3.22. The effect of this error is assumed to be negligible in this thesis.

$$\Delta r = -0.35p - 0.55 \bar{p} \tag{3.22}$$

where

Δr - atmosphere pressure load displacement in mm

p - site pressure difference from the standard value (101.3KPA)

$\bar{p}$ - pressure anomaly within 2000 km from the station

3.3.6 Code Observations Consistency

Because of the emergence of numerous types of receivers, which produce pseudocode observations on L1 and L2, the consistency between these observations has become a matter of investigation. Recent research studies have shown a bias between the C/A and P1 codes of a few decimeters (IGS mail # 5078). Therefore, any successful deployment of un-differenced positioning system should consider this bias. It is worth mentioning that this bias causes a twofold problem. The first problem is that all tracking stations should use the same type of observations to ensure consistent precise orbit and clock data. This is a concern of networks that track GPS satellites. At the user level, users should examine GPS receiver observations thoroughly; otherwise, it will propagate in the position solution. Depending on the type of receivers and the technology of acquiring satellite signals, this problem can be classified. Cross correlation receivers, such as AOA Rogue and TurboRogue (TR), produce C/A, P2 in addition to L1 and L2, but the P2 is calculated based on the summation of C/A code and the difference between P1 and P2, which is monitored by the receiver. Non-cross correlation receiver types, modern receivers, can produce C/A, P1, and P2, in addition to L1 and L2. However, the P2 observations of the latter class of receivers are not equivalent to the corresponding P2 observation of cross correlations receivers. As a result, users have to transfer C/A / P2 cross correlation types of observations to be consistent with P1/P2 non-cross correlation types by applying a satellite-based bias, as given in Equations 3.23 and 3.24, to make them compatible with the modern receiver observations.

$$C/A_{corrected} = C/A + B(i) \qquad\qquad (3.23)$$
$$P2_{corrected} = P2 + B(i) \qquad\qquad (3.24)$$

where

C/A   - coarse acquisition code

$CA_{corrected}$ - corrected C/A code on L1 that is consistent with P1

P2   - P-code on L2

$P2_{corrected}$ - corrected P2 code on L2 that is consistent with modern P2

B(i)   - bias between C/A and P1

In the case in which a non-cross correlation receiver produces C/A instead of P1, the correction can take the following form:

$$C/A_{corrected} = C/A + B(i) \qquad\qquad (3.25)$$

where,

C/A   - coarse acquisition code

$CA_{corrected}$ - corrected C/A code on L1 that is consistent with P1

B(i)   - bias between C/A and P1

The IGS precise data are based on a network that operates on modern GPS receivers. Therefore, users should not worry about the consistency of precise data; instead, they should consider this consistency if using C/A code observations. The values of pseudo code biases are estimated and refined regularly by IGS analysis centers. According to IGS mail # 5078, the biases in nano-seconds for each satellites arranged by PRN value are listed in Table 3.5.

Table 3.5 P1-CA bias (ns)

PRN	bias	PRN	bias	PRN	bias	PRN	bias	PRN	bias
1	-0.028	2	-0.061	3	0.077	4	1.334	5	-0.929
6	0.664	7	-0.912	8	-0.335	9	0.529	10	-1.567
11	0.535	12	NA	13	1.541	14	0.335	15	-1.057
16	-0.419	17	-0.906	18	0.098	19	-2.269	20	-1.105
21	-0.346	22	0.579	23	-0.221	24	0.152	25	0.735
26	1.247	27	-0.018	28	-0.205	29	0.842	30	2.017
31	-0.307								

3.4 Reference Frames

The Earth's surface goes through a slow crust movement in all directions. These movements can take the form of sea level variation, ocean loading, atmosphere loading, solid earth tide, plate tectonics, subsidence, and plate boundary deformation. Local, regional, or even national geodetic datums are unable to describe this type of motions owing to its scale. Therefore, only a global reference frame can express this type of slow motion. The accessibility and the accuracy of reference frames are of importance because every object or feature is referenced with respect to them. The following section presents the major reference frames used in precise positioning.

3.4.1 WGS84

World Geodetic System 1984 (WGS84) is the reference frame used by GPS. It is maintained by US National Imagery and Mapping Agency (NIMA) and accessible

through GPS satellites' ephemeredes. It has evolved since the original form. These changes include the mitigation from WGS84 (original: January 23, 1987 to June 28, 1994), WGS84 (G730: June 29, 1994 to January 28, 1997), and WGS84 (G873: January 29, 1997 to January 19, 2002), to the recent version WGS84 (G1150: January 20, 2002 to present). The last version has offset about two meters from the original one (Kouba and Poelar, 2001; Soler and Snay, 2004). As a result of policies and the nature of the reference frame, there is no precise physical accessibility to this reference frame except un-differenced GPS measurements which can lead to positioning accuracy of a few meters.

3.4.2 NAD 83

The North American datum (NAD83) is the result of collaboration between US and Canada toward a unified spatial reference frame. It started in the mid-1980s through a network of geodetic monuments (Craymer et al., 1999). Evolving of technology and emerging of GPS showed that the NAD83 has an offset of about 2 meters from the true geocenter. The NAD 83 is considered equivalent to WGS84 (original).

3.4.3 ITRF

Because of the limitation of WGS84 reference frame, a civilian terrestrial reference frame was initiated by international efforts. This frame was realized through global Cartesian coordinates and velocity of network of stations (Kouba and Popelar, 2000). These

stations' coordinates have been determined through precise geodetic techniques such as GPS, laser ranging, Doppler, and Very Long Baseline Interferometery (VLBI). The body controlling the ITRF is The International Earth Rotation and Reference Systems Service (IERS). ITRF has undergone several revisions and refinements, such as ITRF89, ITRF90, ITRF91, ITRF92, ITRF93, ITRF94, ITRF95, ITRF96, ITRF97, and ITRF2000. The ITRF accounts for earth curst deformation from plate tectonics, the NUVEL-1A (DeMets et al., 1994; McCarthy, 1996; Leick, 2004). Therefore, any station coordinates expressed in ITRF coordinates must be identified with a date. It is worth mentioning that the consistency between the revised WGS84 (G1150) and ITRF2000 is at the level of cm (Merrigan et al., 2002).

3.4.4 Transformation between Reference Frames

To express a 3D point or baseline coordinates in different reference frames, the similarity transformation is used. The traditional way is to define a similarity transformation with seven parameters: three translations, three rotations, and a scale. However, because of the change of geodetic measurements, the time changes of these parameters are also needed. Consequently, the transformation parameters between two reference frames include their rate of change, in addition to the seven similarity transformation parameters. The general transformation between the two frames takes the following form:

$$
\begin{pmatrix} X_t(t) \\ Y_t(t) \\ Z_t(t) \end{pmatrix} = \begin{pmatrix} T_x(t) \\ T_y(t) \\ T_z(t) \end{pmatrix} + \begin{pmatrix} S(t) & -R_z(t) & R_y(t) \\ R_z(t) & S(t) & -R_x(t) \\ -R_y(t) & R_x(t) & S(t) \end{pmatrix} \begin{pmatrix} X_s(t) \\ Y_s(t) \\ Z_s(t) \end{pmatrix}
\tag{3.26}
$$

$$R_x(t) = R_x(t_o) + \dot{R}_x(t - t_o) \tag{3.27}$$

$$R_y(t) = R_y(t_o) + \dot{R}_y(t - t_o) \tag{3.28}$$

$$R_z(t) = R_z(t_o) + \dot{R}_z(t - t_o) \tag{3.29}$$

$$T_x(t) = T_x(t_o) + \dot{T}_x(t - t_o) \tag{3.30}$$

$$T_y(t) = T_y(t_o) + \dot{T}_y(t - t_o) \tag{3.31}$$

$$T_z(t) = T_z(t_o) + \dot{T}_z(t - t_o) \tag{3.32}$$

$$S(t) = S(t_o) + \dot{S}(t - t_o) \tag{3.33}$$

where

$X_t(t)$ - X- coordinate in the target reference system

$Y_t(t)$ - Y- coordinate in the target reference system

$Z_t(t)$ - Z- coordinate in the target reference system

$T_x(t)$ - Geocenter X-shift between the two reference frames

$T_y(t)$ - Geocenter Y-shift between the two reference frames

$T_z(t)$ - Geocenter Z-shift between the two reference frames

$R_x(t)$ - rotation between the X-axes of the two reference frames

$R_y(t)$ - rotation between the Y-axes of the two reference frames

$R_z(t)$ - rotation between the Z-axes of the two reference frames

$S(t)$ - scale between the two reference frame

$\dot{T}_x$ - Geocenter X-shift rate between the two reference frames

$\dot{T}_y$ - Geocenter Y-shift rate between the two reference frames

$\dot{T}_y$ - Geocenter Z-shift rate between the two reference frames

$\dot{R}_z$ - rotation rate between the X-axes of the two reference frames

$\dot{R}_y$ - rotation rate between the Y-axes of the two reference frames

$\dot{R}_z$ - rotation rate between the Z-axes of the two reference frames

t - target epoch

t_o - reference epoch

$\dot{S}$ - scale rate of change

These transformation equations can be used to transform the coordinates from one to different frames. A compendium of transformation parameters between ITRF and NAD83 reference frames are depicted in Table 3.6 (Soler et al., 2001; Soler and Marshall, 2003; Craymer et al., 1999).

Table 3.6 Transformation parameters between different reference frames

Parameters	ITRF93 to NAD83	ITRF94 To NAD83	ITRF96 to NAD83	ITRF97 To NAD83	ITRF00 to NAD83	ITRF97 to ITRF96	ITRF00 to ITRF97
T_X (m)	0.9769	0.9738	0.9910	0.9889	0.9956	-0.00207	0.0067
T_Y (m)	-1.9392	-1.9353	-1.9072	-1.9074	-1.9013	0.00069	0.0000
T_Z (m)	-0.5461	-0.5486	-0.5129	-0.5030	-0.5215	-0.00021	0.0061
R_x (mas)	26.40	27.55	25.79	25.915	25.915	-0.00010	-0.0006
R_y (mas)	10.10	10.05	9.65	9.426	9.426	0.00995	-0.0185
R_z (mas)	10.30	11.36	11.66	11.599	11.599	0.00186	-0.0014
$\dot{T}_X$ m/year	0	0	0	0.0007	0.0007	0.12467	0.0
$\dot{T}_Y$ m/year	0	0	0	-0.0001	-0.0007	0.01347	0.0
$\dot{T}_Z$ m/year	0	0	0	0.0019	0.0005	-0.22355	0.0
$\dot{R}_X$ mas/year	0	0.09	0.0532	0.067	0.067	-0.01514	0.0
$\dot{R}_Y$ mas/year	0	-0.77	-0.7423	-0.757	-0.757	-0.06065	0.0
$\dot{R}_Z$ mas/year	0	0.02	-0.0316	-0.031	-0.051	0.00027	-0.02
S (ppb)	0	0	0	-0.93	0.62	+0.93496	1.55
$\dot{S}$ (ppb/year)	0	0	0	-0.19	-0.18	-0.19201	0.01
Reference epoch	1995.00	1996.00	1997.00	1997.00	1997.00	1997.00	1997.00

CHAPTER 4

PPP FUNCTIONAL AND STOCHASTIC MODELLING

4.1 Introduction

This chapter presents the mathematical model of Precise Point Positioning. First, a brief summary of Kalman Filter is presented and then the detailed functional and stochastic implementations of PPP are described.

4.2 Kalman Filter

Kalman Filter (KF) is a recursive optimal estimator that incorporates knowledge about the system and the measurements (Gelb, 1979). It is recursive because the user does not need to save previous observations; instead, all previous information is carried forward in the filter. It is optimal because the design of the filter satisfies the three general optimality conditions as given in Equations 4.1 to 4.3 (Mikhail and Ackermann, 1976):

Consistence $\quad \lim_{n\to\infty} P(|\hat{x}-x|<\varepsilon)=1$ (4.1)

Unbiased $\quad E(\hat{x})=x$ (4.2)

Minimum mean square error $\quad E\{(\hat{x}-E(\hat{x}))^T(\hat{x}-E(\hat{x}))\}=\min$ (4.3)

where

n - sample size

x - parameters being estimated

$\hat{x}$ - estimate of the parameter x

ε - a very small value

$P()$ - statistical probability

$E()$ - statistical expectation

The recursive and optimality natures are the two main reasons for the selection of this filter. Kalman's architecture includes measurement and system models as well as their corresponding stochastic models as illustrated in Equations 4.4 and 4.5. The details of these functional and stochastic models will be covered in later sections of this chapter. One of the characteristics of the noises, namely w_{k-1}, and v_k, of the two models is that they are assumed to be independent from each other and distributed according to the normal distribution.

System Model

$$x_k = \Phi_{k-1}x_{k-1} + w_{k-1} \, , \; w_{k-1} \sim N(0, Q_{k-1}) \tag{4.4}$$

Measurements Model

$$z_k = H_k x_k + v_k \, , \; v_k \sim N(0, R_k) \tag{4.5}$$

where

x_k - state vector at epoch k

Φ_{k-1} - transition matrix at epoch k-1

x_{k-1} - state vector at epoch k-1

w_{k-1} - system noise at epoch k-1

Q_{k-1} — covariance matrix of system noise w_{k-1}

z_k — measurements vector

H_k — design matrix

v_k — measurement noise vector

R_k — covariance matrix of measurement noise v_k

The random vectors v and w are assumed to be Gaussian with known statistics and must satisfy the following conditions:

$$E(w_k v_j^T) = 0, \text{ for all } j, k \tag{4.6}$$

$$E(w_k w_j^T) = \begin{cases} Q, \text{ for all } j = k \\ \\ 0, j \neq k \end{cases} \tag{4.7}$$

$$E(v_k v_j^T) = \begin{cases} R, \text{ for all } j = k \\ \\ 0, j \neq k \end{cases} \tag{4.8}$$

In terms of data processing, two major steps characterize the Kalman filter: the first is prediction, and the second is updating as shown in Equations 4.9 to 4.13 (Gelb, 1979; Grewal and Andrews, 1993).

Prediction

$$\hat{x}_k(-) = \Phi_{k-1}\hat{x}_{k-1}(+) \tag{4.9}$$

$$P_k(-) = \Phi_{k-1}P_{k-1}(+)\Phi_{k-1}^T + Q_{k-1} \tag{4.10}$$

Updating

$$K_k = P_k(-)H_k^T[H_k P_k(-)H_k^T + R_k]^{-1} \tag{4.11}$$

$$\hat{x}_k(+) = \hat{x}_k(-) + K_k[z_k - H_k\hat{x}_k(-)] \tag{4.12}$$

$$P_k(+) = [I - K_k H_k] P_k(-) \qquad\qquad (4.13)$$

where

$\hat{x}_k(-)$, $\hat{x}_k(+)$ - predicted and updated state vectors

$P_k(-)$, $P_k(+)$ - predicted and updated state vector variance covariance matrices

K_k - gain matrix

In the formulas above, the (-) sign indicates prediction and the (+) sign indicates updating. The K_k expresses the gain matrix. The Kalman filter process is illustrated in Figure 4.1 (Witchayangkoon, 2000).
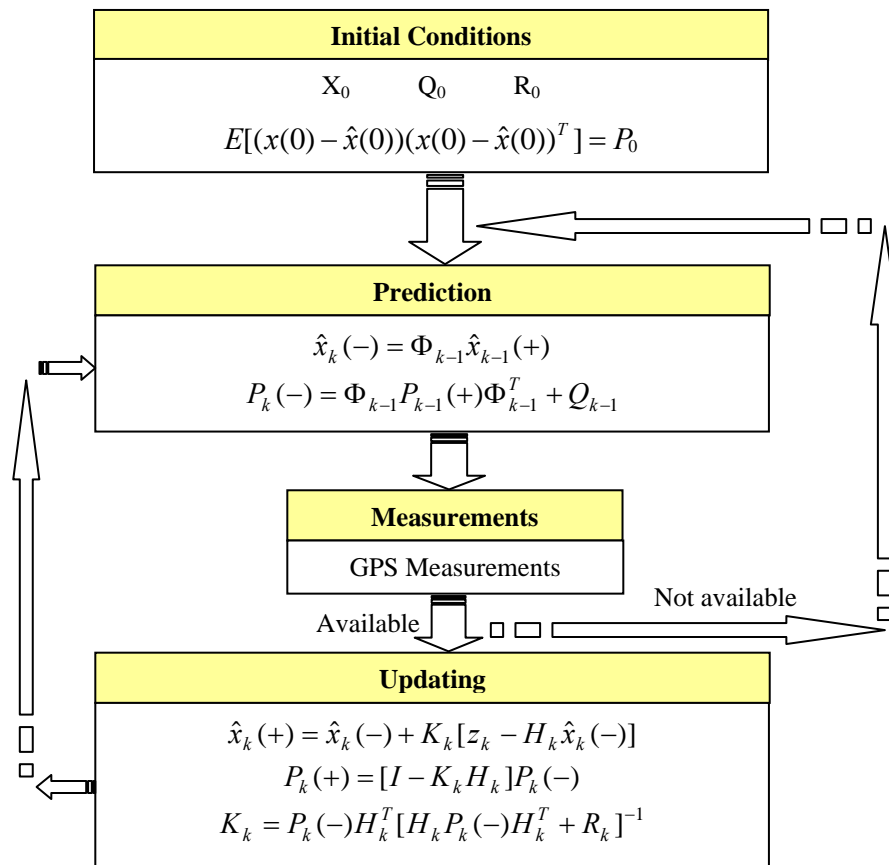
Figure 4.1 Kalman filter illustration

4.3 Observation Models

The observation model represents the explicit relation between observations and unknowns. Using the Least Square or Kalman filter principle, the GPS measurements can be linked in a suitable form to the unknown parameters. The selection of this relationship must avoid any formulation that can result in similar parameter coefficients; otherwise, a defective system could arise. In the next subsections, the PPP function models are presented.

4.3.1 The Traditional Model

The ionosphere-free code and carrier phase observations combinations are the most famous formulation used to alleviate the cumbersome effect caused by the ionosphere. Zumberge et al. (1998) as well as Kouba and Heroux (2000) have used both of these combinations as a functional model for PPP. For the sake of convenience, the un-differenced observation equations and the traditional model are illustrated in the following equations:

$$P(Li) = \rho - cdT + d_{trop} + d_{ion/Li} + d^{s}_{Interfreq/P(Li)} - d_{r(Interfreq/P(Li))} + d^{s}_{hd/P(Li)} - d_{r(hd/P(Li))} +$$
$$d_{mult/P(Li)} + \varepsilon(P(Li))$$

$$(4.14)$$

$$\Phi(Li) = \rho - cdT + d_{trop} - d_{ion/Li} + \lambda_i N_i + \tilde{d}^{s}_{Interfreq/\Phi(Li)} - \tilde{d}_{r(Interfreq/\Phi(Li))} + \lambda_i(\phi_r(t_0, Li) -$$
$$\phi_s(t_0, Li)) + \tilde{d}^{s}_{hd/\Phi(Li)} - \tilde{d}_{r(hd/\Phi(Li))} + d_{mult/\Phi(Li)} + \varepsilon(\Phi(Li))$$

$$(4.15)$$

$$P_{IF} = \frac{f_1^2 \cdot P(L_1) - f_2^2 \cdot P(L_2)}{f_1^2 - f_2^2}$$ (4.16)

$$= \rho + -cdT + d_{trop} + d^s_{hd(P(L_1,L_2))} - d_{r(hd(P(L_1,L_2)))} + d_{mult/P(L_1,L_2)} + \varepsilon\ (P(L_1,L_2))$$

$$\Phi_{IF} = \frac{f_1^2 \cdot \Phi(L_1) - f_2^2 \cdot \Phi(L_2)}{f_1^2 - f_2^2}$$

$$= \rho - cdT + d_{trop} + \frac{f_1^2 \lambda_1 N_1 - f_2^2 \lambda_2 N_2}{f_1^2 - f_2^2} + \frac{f_1^2 \lambda_1}{f_1^2 - f_2^2}(\phi_r(t_0, L_1) - \phi_s(t_0, L_1)) +$$ (4.17)

$$\frac{f_2^2 \lambda_2}{f_1^2 - f_2^2}(\phi_r(t_0, L_2) - \phi^s(t_0, L_2)) + \tilde{d}^s_{hd(\Phi(L_1,L_2))} - \tilde{d}_{r(hd(\Phi(L_1,L_2)))} + d_{mult/\Phi(L_1,L_2)} +$$

$$\varepsilon\ (\Phi(L_1, L_2))$$

where

$P(L_i)$ - measured pseudorange on Li (m)

$\Phi(L_i)$ - measured carrier phase on Li (m)

Φ_{IF} - ionosphere-free carrier phase combination

ρ - true geometric range (m)

c - speed of light (m/s)

dT - receiver clock error (s)

d_{trop} - tropospheric delay (m)

$d_{ion/Li}$ - ionospheric delay on Li (m)

$d^s_{hd/P(Li)}$ - satellite pseudocode hardware bias on Li (m)

$d_{r(hd/P(Li))}$ - receiver pseudocode hardware bias on Li (m)

$\tilde{d}^s_{hd/\Phi(Li)}$ - satellite carrier phase hardware bias on Li (m)

$\tilde{d}_{r(hd/\Phi(Li))}$ - receiver carrier phase hardware bias on Li (m)

$d_{r(Interfreq/P(Li))}$ - receiver pseudocode inter-frequency bias on Li (m)

$$= (cT_{GD,r}, \frac{f_1^2}{f_2^2} cT_{GD,r} \text{ for } i=1,2, \text{ respectively})$$

$d_{Interfreq/P(Li)}^{s}$ - satellite pseudocode inter-frequency bias on Li (m)

$$= (cT_{GD,s}, \frac{f_1^2}{f_2^2}cT_{GD,s} \text{ for } i=1,2, \text{ respectively})$$

$\tilde{d}_{r(Interfreq/\Phi(Li))}$ - receiver carrier phase inter-frequency bias on Li (m)

$$= (cT'_{GD,r}, \frac{f_1^2}{f_2^2}cT'_{GD,r} \text{ for } i=1,2, \text{ respectively})$$

$\tilde{d}_{Interfreq/\Phi(Li)}^{s}$ - satellite carrier phase inter-frequency bias on Li (m)

$$= (cT'_{GD,s}, \frac{f_1^2}{f_2^2}cT'_{GD,s} \text{ for } i=1,2, \text{ respectively})$$

λ_i - wavelength on Li (m)

N_i - integer phase ambiguity on Li (cycle)

$\phi_r(t_0, L_i)$ - initial phase of the receiver oscillator

$\phi^s(t_0, L_i)$ - initial phase of the satellite oscillator

$d_{mult/P(Li)}$ - multipath effect in the measured pseudorange on Li (m)

$d_{mult/\Phi(Li)}$ - multipath effect in the measured carrier phase on Li (m)

$\varepsilon(.)$ - measurement noise (m).

In Equations 4.14 and 4.15 above, the inter-frequency biases and the hardware delay can be lumped together because they are inseparable (Leick, 2004; IDC-GPS-200C, 2000). The inter-frequency bias is a delay between L1 and L2 signals to allow dual frequency GPS users to mitigate GPS ionospheric delay. It must be considered when using L1 or L2 alone. For the case of the ionosphere-free observations combination, the inter-frequency bias is canceled. In this context, the hardware delay is caused by satellite and receiver hardware components such as the RF and signal processing (Ray, 2005; Raquet, 2001). This hardware delay is of no concern to navigation process since it has the same

magnitude for all frequencies and channels. Accordingly, it would be lumped to receiver clock (Ray, 2005). Appendix B shows the different GPS delays and their sources. The PPP traditional model as illustrated in Equations 4.16 and 4.17 is capable of mitigating the first order ionospheric delay effect as well as the inter-frequency bias, whereas the equipment (hardware) delay will remain. For the carrier phase, the nonzero initial phase will not be cancelled in these equations and will be mapped to the ambiguities. This mapping should not be a problem because the ionosphere-free ambiguities $(\frac{f_1^2 \lambda_1 N_1 - f_2^2 \lambda_2 N_2}{f_1^2 - f_2^2})$ are calculated as a lumped term and treated as a float number. If Doppler measurements are not considered, the estimated variables herein are three positional parameters, receiver clock offset, zenith tropospheric delay, and the ionosphere-free carrier phase ambiguities. Therefore, if the number of the observed satellite is n, the number of observation equations will be *2n* and the number of unknowns will be *5+n*. Equation 4.18 shows the vector of parameters. An example for the design matrix for one satellite is given in Equations 4.19 and 4.20 for a general case which includes ionosphere-free code and phase rate observations. The order of the elements is arbitrary and presented here only for illustration purposes.

$$X = \left\{ \delta\phi, \delta\lambda, \delta h, \delta\dot{\phi}, \delta\dot{\lambda}, \delta\dot{h}, \delta dT, \delta d\dot{T}, \delta Trop, \delta N_1, ,, \delta N_n \right\}^T \tag{4.18}$$

$$A_i = \begin{bmatrix} \dfrac{\partial f(X, \ell_{P_{IF}})}{\partial X_i} \\[6pt] \dfrac{\partial f(X, \ell_{\Phi_{IF}})}{\partial X_i} \\[6pt] \dfrac{\partial f(X, \ell_{Doppler_{IF}})}{\partial X_i} \end{bmatrix} = \tag{4.19}$$

$$\begin{bmatrix} A_{1,1} & A_{1,2} & A_{1,3} & A_{1,4} & A_{1,5} & A_{1,6} & A_{1,7} & A_{1,8} & A_{1,9} & A_{1,10} & A_{1,11} & . & . & A_{1,9+n} \\ A_{2,1} & A_{2,2} & A_{2,3} & A_{2,4} & A_{2,5} & A_{2,6} & A_{2,7} & A_{2,8} & A_{2,9} & A_{2,10} & A_{2,11} & . & . & A_{2,9+n} \\ A_{3,1} & A_{3,2} & A_{3,3} & A_{3,4} & A_{3,5} & A_{3,6} & A_{3,7} & A_{3,8} & A_{3,9} & A_{3,10} & A_{3,11} & . & . & A_{3,9+n} \end{bmatrix}$$

$$\underbrace{\qquad}_{\text{Position}} \quad \underbrace{\qquad}_{\text{Velocity}} \quad \underbrace{\quad}_{\text{Clock}} \underbrace{\;}_{\text{Trop}} \underbrace{\qquad}_{\text{Ambiguity}} \tag{4.20}$$

where

n	- is the number of satellites
i	- represents an arbitrary satellite
$\delta\dot{\Phi}$	- rate of change of latitude error
$\delta\dot{\lambda}$	- rate of change of longitude error
$\delta\dot{h}$	- rate of change of height error
$\delta\dot{dT}$	- rate of change of receiver clock error

The details of each element, $A_{i,j}$ in Equation 4.20, are given in Appendix C.

4.3.2 The UofC Model

Unlike the traditional model, the UofC model (Gao and Shen, 2001) uses an average of code and carrier phase observations on L_1 and L_2 in addition to the ionosphere-free carrier phase combination. The model description is illustrated in Equations 4.21 to 4.24.

$$P_{Pi,\Phi i} = 0.5(P_{SM}(L_i) + \Phi(L_i)) \tag{4.21}$$

$$
\begin{aligned}
P_{(P1,\Phi1)} = {} & \rho - c \cdot dT + T_{trop} + 0.5\lambda_1 N_1 + 0.5\lambda_1(\phi_r(t_0,L_1) - \phi^s(t_0,L_1)) + \\
& 0.5(d^s_{hd/P(L1)} + \tilde{d}^s_{hd/\Phi(L1)} - d_{r(hd/P(L1))} - \tilde{d}_{r(hd/\Phi(L1))}) + \\
& 0.5(d^s_{Interfreq/P(L1)} - d_{r(Interfreq/P(L1))} + \tilde{d}^s_{Interfreq/\Phi(L1)} - \tilde{d}_{r(Interfreq/\Phi(L1))}) + \\
& d_{mult(\Phi((L1),P(L1))} + \varepsilon(\Phi(L_1),P(L_1))
\end{aligned}
\tag{4.22}
$$

$$
\begin{aligned}
P_{(P2,\Phi2)} = {} & \rho - c \cdot dT + d_{trop} + 0.5\lambda_2 N_2 + 0.5\lambda_2(\phi_r(t_0,L_2) - \phi_s(t_0,L_2)) + \\
& 0.5(d^s_{hd/P(L2)} + \tilde{d}^s_{hd/L2} - d_{r(hd/P(L2))} - \tilde{d}_{r(hd/\Phi(L2))}) + \\
& 0.5(d^s_{Interfreq/P(L2)} - d_{r(Interfreq/P(L2))} + \tilde{d}^s_{Interfreq/\Phi(L2)} - \tilde{d}_{r(Interfreq/\Phi(L2))}) + \\
& d_{mult(\Phi(L2),P(L2))} + \varepsilon(\Phi(L_2),P(L_2))
\end{aligned}
\tag{4.23}
$$

$$
\begin{aligned}
\Phi_{IF} = {} & \rho - c \cdot dT + d_{trop} + \frac{f_1^2 \lambda_1}{f_1^2 - f_2^2} N_1 + \frac{f_2^2 \lambda_2}{f_1^2 - f_2^2} N_2 + \frac{f_1^2 \lambda_1}{f_1^2 - f_2^2}(\varphi_r(t_0,L_1) - \varphi_s(t_0,L_1)) + \\
& \frac{f_2^2 \lambda_2}{f_1^2 - f_2^2}(\varphi_r(t_0,L_2) - \varphi^s(t_0,L_2)) + \tilde{d}^s_{hd(L1,L2)} - \tilde{d}_{r(hd(L1,L2))} + d_{mult/\Phi(L_1,L_2)} + \varepsilon(\Phi(L_1,L_2))
\end{aligned}
\tag{4.24}
$$

where

$P_{Pi,\Phi i}$ — average of pseudocode and carrier phase observations

$P_{SM}(Li)$ — ionospheric-free smoothed pseudocode

$P_{\Phi1,L1}$ — average of pseudocode and carrier phase observations on L1

$P_{\Phi2,L2}$ — average of pseudocode and carrier phase observations on L2

This model allows for the estimation of ambiguities on the L1 and L2 frequencies, station position, receiver clock offset, and troposphere. For the case of observing *n* satellites and no Doppler observations are considered, the number of observation equations will be *3n*, while the number of the unknown will be equal to *5+2n*. Several systematic delays or errors will remain in the system such as the non-zero initial phase, code, and carrier phase inter-frequency bias for satellite as well as receiver. If opposite signs are assumed for the inter-frequency bias in the case of the code and carrier phase, then only the difference between them will remain. How big the difference is, is not quite known, but for the sake of simplicity we will assume that they are equal and will return to this point later in Sections 7.7.3 and 6.3. For the ionosphere-free carrier phase combination, there will be no inter-frequency bias as stated earlier; however, the non-zero initial phase will remain in all equations. The satellites' non-zero initial phase and the difference in inter-frequency bias for the satellite segment will join the ambiguities, whereas the receiver equivalent part will join the station clock (Teunissen and Kleusberg, 1998; Liu, 2002). The reason is that any systematic errors related to an individual satellite will join ambiguities, and those that are common to all satellites will map to the GPS station clock. The vector of parameters is given in Equation 4.25. An example for the design matrix for one satellite is given in Equations 4.26 and 4.27.

$$X = \left\{ \delta\Phi, \delta\lambda, \delta h, \delta\dot{\Phi}, \delta\dot{\lambda}, \delta\dot{h}, \delta dT, \delta d\dot{T}, \delta Trop, \delta N_1, \delta N_2,, \delta N_{2\times n} \right\} \qquad (4.25)$$

$$A_i = \begin{bmatrix} \dfrac{\partial f(X, \ell_{(P1+\Phi1)/2})}{\partial X_i} \\ \dfrac{\partial f(X, \ell_{(P2+\Phi2)/2})}{\partial X_i} \\ \dfrac{\partial f(X, \ell_{\Phi IF})}{\partial X_i} \\ \dfrac{\partial f(X, \ell_{doppler})}{\partial X_i} \end{bmatrix} \qquad (4.26)$$

$$A = \begin{bmatrix} A_{1,1} & A_{1,2} & A_{1,3} & A_{1,4} & A_{1,5} & A_{1,6} & A_{1,7} & A_{1,8} & A_{1,9} & A_{1,10} & A_{1,11} & \cdot & \cdot & \cdot & A_{1,9+n\times2} \\ A_{2,1} & A_{2,2} & A_{2,3} & A_{2,4} & A_{2,5} & A_{2,6} & A_{2,7} & A_{2,8} & A_{2,9} & A_{2,10} & A_{2,11} & \cdot & \cdot & \cdot & A_{2,9+n\times2} \\ A_{3,1} & A_{3,2} & A_{3,3} & A_{3,4} & A_{3,5} & A_{3,6} & A_{3,7} & A_{3,8} & A_{3,9} & A_{3,10} & A_{3,11} & \cdot & \cdot & \cdot & A_{3,9+n\times2} \\ A_{4,1} & A_{4,2} & A_{4,3} & A_{4,4} & A_{4,5} & A_{4,6} & A_{4,7} & A_{4,8} & A_{4,9} & A_{4,10} & A_{4,11} & \cdot & \cdot & \cdot & A_{4,9+n\times2} \end{bmatrix}$$

$$\underbrace{\phantom{A_{1,1} A_{1,2} A_{1,3}}}_{\text{Position}} \quad \underbrace{\phantom{A_{1,4} A_{1,5} A_{1,6}}}_{\text{Velocity}} \quad \underbrace{\phantom{A_{1,7} A_{1,8}}}_{\text{Clock}} \quad \underbrace{\phantom{A_{1,9}}}_{\text{Trop}} \quad \underbrace{\phantom{A_{1,10} A_{1,11}}}_{\text{Ambiguity}} \qquad (4.27)$$

There is a similarity among the elements of the design matrix of both models and only two slight differences. The first is that one extra row appeared. The second is that there are two columns corresponding to the ambiguities instead of one. The details of the design matrix are shown in Appendix D.

4.4 Stochastic Modeling

A proper modeling of any problem must guarantee an incorporation of statistical information along with its deterministic component. Three branches of stochastic modeling are addressed: observations, system dynamic, and parameters. Observations' stochastic modeling includes information about the accuracy of the model's measurements and any relations among observations. The stochastic description of the

system dynamics expresses the kinematic behavior of the GPS station and the change of parameters with time. Parameters' stochastic information includes particulars about the initial accuracy of the parameters and its variation over time.

4.5 Observations' Stochastic Modeling

GPS produces several measurements such as code, carrier phase, and phase rate (Doppler). These observations have different accuracies; therefore, when dealing with different GPS observations, the weight of each observation should be chosen carefully to express their absolute and relative accuracies with respect to each other. In the case of mixing the observations, the error propagation concept should be applied to estimate the precision of the combination under consideration. Observations' stochastic modeling has been a matter of interest in many studies, including El-Rabbany (1994); Tiberius (1999); Bona (2000); Bona (2000a); and Liu (2002). In this section, two points of interest will be addressed: the generation of different observations and the mathematical correlation of observations. The first is called the "stochastic physical correlation" and the second is called the "stochastic functional correlation".

4.5.1 Stochastic Physical Correlation

Depending on the type of GPS receiver, the GPS measurements are generated using different tracking methodologies. For PPP, two situations exist: cross correlation and the modern codeless (non cross-correlation) receivers. Cross correlation receivers monitor

the P_1 and L_1 signals in addition to their difference from P_2 and L_2. Therefore, the measurements P_2 and L_2 are directly related to P_1 and L_1. As a result, there is a correlation between the observations on L_1 and L_2. On the contrary, modern receivers (noncross-correlation) rebuild code and carrier phase observations separately on both L_1 and L_2. Hence, the observations resulting from the codeless receiver are considered with no correlation. As most of the dual frequency receivers tend to be codeless, the weight matrix of un-differenced observations will be diagonal and the value of the diagonals will mainly depend on the type of observations and their relative precision.

Another issue that can lead to stochastic correlation is that each satellite signal traveled through different geometric paths. Thus, the measurements' accuracy to each GPS satellite is a function of these paths. A long path can cause attenuation for the GPS signals and makes them noisy. This can be quantified through either the elevation of the satellite, the signal to noise ratio, or a combination of both (Jin, 1996; Tiberius, 2003; Collins and Langley, 1999; Witchayangkoon, 2000). The common practice is to quantify the precision of satellite measurements throughout the elevation angle, which can take several mapping forms such as exponential and trigonometric functions. The function used herein is the *SIN* as shown in Equation 4.28. The reason for using this function is attributed to the similarity of the Cosecant function and behavior of troposphere and ionospheric delay changes with respect to the satellite elevation (Vermeer, 1997; Collins and Langely, 1999).

$$M(E) = \frac{1}{\sin(Elevation)} \tag{4.28}$$

4.5.2 Stochastic Functional Correlation

In the two PPP functional models, GPS observations are not used directly. Instead, they are combined with each other. Therefore, error propagation should be applied to estimate the precision of the combined observation. The effect of this function correlation on the two PPP models is illustrated below.

4.5.2.1 Traditional Model

If no correlation is assumed between $P(L_1)$ and $P(L_2)$ in addition to $\Phi(L_1)$ and $\Phi(L_2)$, the covariance between them vanishes. Also, if the correlation between the smoothed code and the carrier phase observations is considered to be zero, the covariance matrix of the observations will be diagonal. This is the case used herein, $Q_{P\Phi}=0$. The effect of using the carrier phase to smooth the code may be of interest and can generate covariance between the two types of ionosphere-free combinations. Therefore, the observations covariance matrix can be non-diagonal. The observations covariance matrix is illustrated and expressed in Figure 4.2 as well as Appendix E.
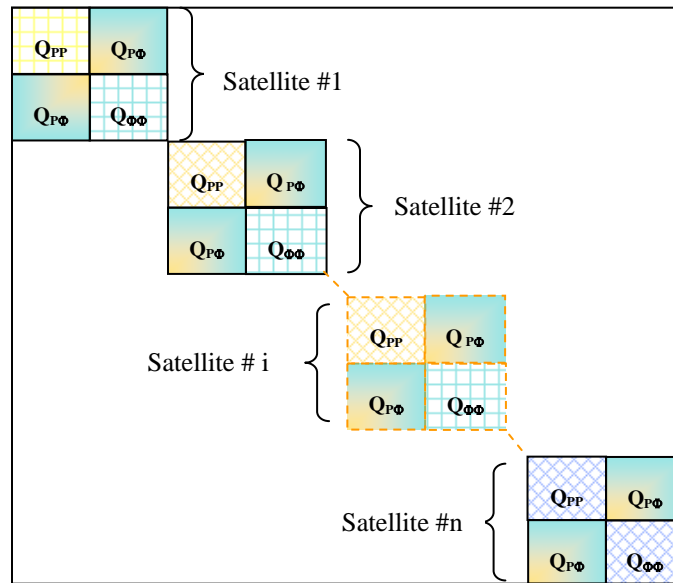
Figure 4.2 Covariance matrix of the GPS observations (Traditional model)

4.5.2.2 UofC Model

The UofC uses an average of code and carrier phase observations on L1 and L2 as well as the ionosphere free carrier phase combination. Therefore, even if there is no correlation between the smoothed code and carrier phase observation, there will be a correlation between the first two observation equations and the last one. This correlation can be calculated using the concept of error propagation. This correlation is given in Equations 4.29 and 4.30 as well as Appendix F. Figure 4.3 depicts the general structure of the observations covariance matrix. In the case of considering the effect of smoothing the code with carrier phase observations a more complex form can be derived.

$$\sigma_{12} = 0.5 \frac{f_1^2}{f_1^2 - f_2^2} \sigma_{\Phi 1}^2 \qquad (4.29)$$

$$\sigma_{13} = 0.5 \frac{f_2^2}{f_1^2 - f_2^2} \sigma_{\Phi 2}^2 \qquad (4.30)$$

where

σ_{12} - correlation between $0.5(P_1+\Phi_1)$ and $\Phi_{iono\text{-}free}$

σ_{13} - correlation between $0.5(P_2+\Phi_2)$ and $\Phi_{iono\text{-}free}$

$\sigma_{\Phi1}^2$ - precision of carrier phase observation on L_1

$\sigma_{\Phi2}^2$ - precision of carrier phase observation on L_2
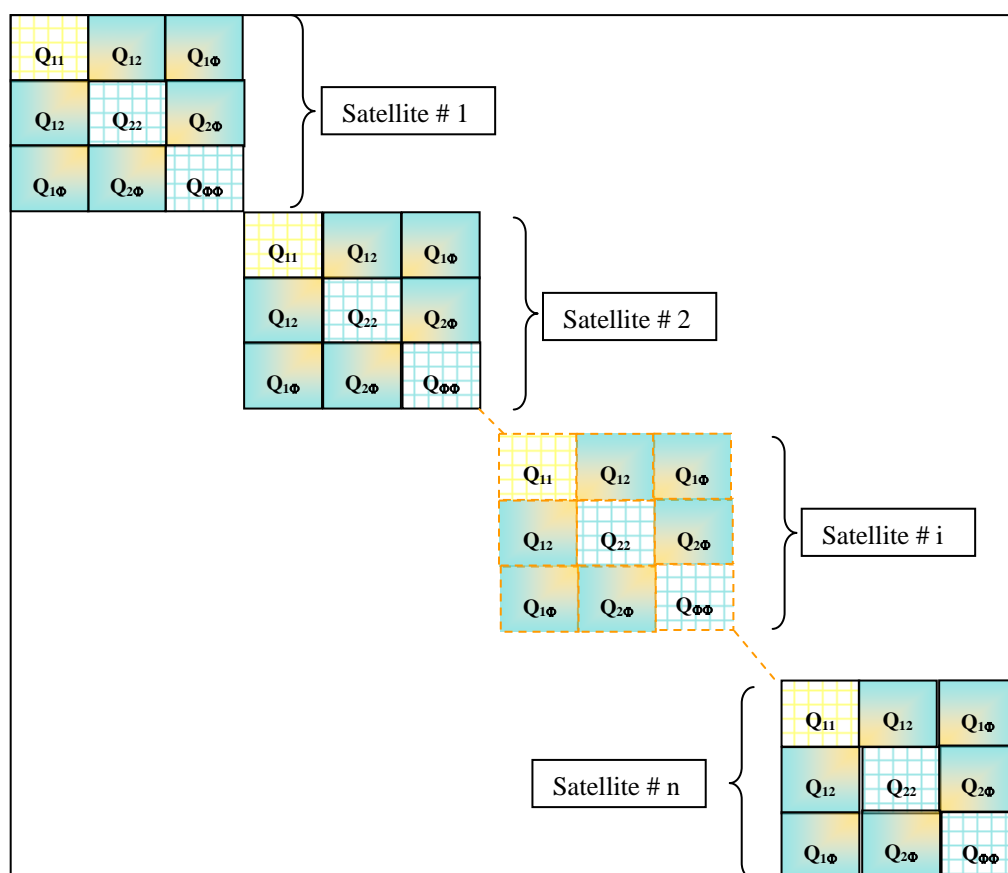
Figure 4.3 Covariance matrix of the GPS observations (UofC model)

4.6 Parameters' Stochastic Modeling

The nature of the parameters dictates the suitable modeling process. Recalling the observation models, the PPP state vector contains states that correspond to position coordinates, receiver clock, zenith tropospheric delay, and ambiguity errors. Position and clock states are usually modeled as Random Walk or first order Gauss Markov (Brown and Hwang, 1997; Kechine et al., 2003; Axelrad and Brown, 1996). Conversely, the long established way for modeling the troposphere is to assume it is a random walk as will be seen in Section 4.6.1 (Kouba and Heroux, 2000; Zumberge et al., 1998). The selection of the suitable stochastic model depends mainly on the application under consideration. The ambiguity states are assumed to be constant if no cycle slips over time. The transition and noise matrices for the cases of random walk and first order Gauss Markov is given herein. First, the general transition and noise matrices are provided. For illustration purposes, the structure of these matrices is divided into sub-blocks, in which each block represents a set of related parameters, such as position, clock, troposphere, and ambiguities. Figure 4.4 shows the general structure of the noise matrix that is used in Kalman filter.
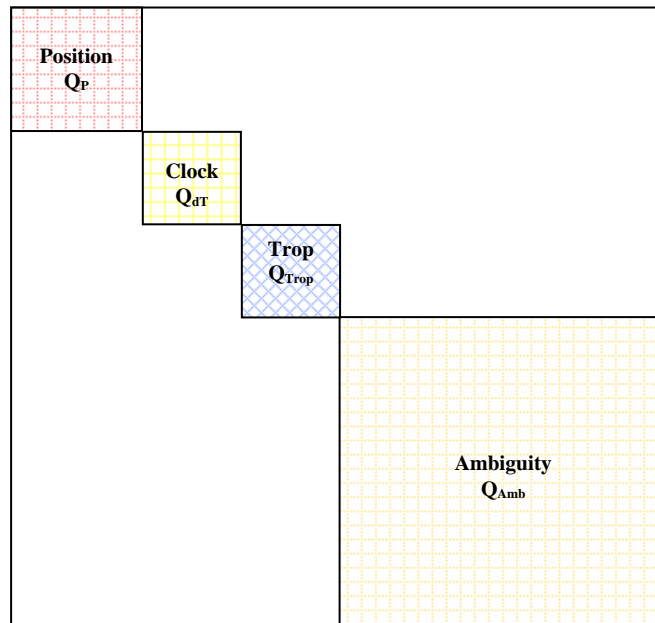
Figure 4.4 Noise matrix structure

4.6.1 Matrices Block Composition

Depending on the parameters' model under consideration, the sub-matrix blocks can be constructed. All the models presented herein can be deduced from the solution of the differential equation of the system dynamic and the propagation of its variance-covariance matrix as shown in the simplified Equations 4.31 and 4.32, respectively (Gelb, 1983; Brown and Hwang, 1997).

$$\dot{x}(t) = F(t)x(t) + w(t), \; q(t) \tag{4.31}$$

$$Q = \int_0^{\Delta t} \Phi(t)q(t)\Phi^T(t) \tag{4.32}$$

where

$x(t)$ - parameters

$F(t)$ - system dynamic matrix

$w(t)$ - white noise

$q(t)$ - spectral density matrix

Q - process noise matrix

$\Phi(t)$ - transition matrix

4.6.1.1 Case of Velocity Estimation

In the case of velocity estimation, Doppler observations are considered available and therefore the rate of change of the parameter (velocity) can be estimated. The next subsection illustrates the composition of the transition and noise matrices (Abousalem, 1996).

GPS Station Coordinates Block

Two models are presented for the station parameters: Random Walk (RW) and first order Gauss-Markov (first GM). It is worth mentioning that the velocity state is the one that will be modeled as first GM or RW. When the velocity state is not considered for estimation, the states itself (position and clock) will be modeled as first GM or RW. These two models are presented in Equations 4.33 and 4.34. Generally speaking, there is no preference between the two models in GPS applications. Both of them are well-known and applicable.

$$\dot{x} = w \tag{4.33}$$

$\dot{x}$ - state rate

w - noise

$$\dot{x} = \frac{1}{\beta} x + w \tag{4.34}$$

x - state

$\dot{x}$ - state rate

β - correlation time

w - noise

Assuming the estimation of velocity and the case of Random Walk, the positioning block

in the transition matrix will look like that given in Equation (4.35):

$$\Phi_{Position\ block} = \begin{bmatrix} 1 & \dfrac{\Delta t}{(R_m + h)} & 0 & 0 & 0 & 0 \\ 0 & 1 & 0 & 0 & 0 & 0 \\ 0 & 0 & 1 & \dfrac{\Delta t}{(R_n + h)\cos\phi} & 0 & 0 \\ 0 & 0 & 0 & 1 & 0 & 0 \\ 0 & 0 & 0 & 0 & 1 & \Delta t \\ 0 & 0 & 0 & 0 & 0 & 1 \end{bmatrix} \tag{4.35}$$

The noise matrix is shown in Equation 4.36.

$$Q_{Position\ block} = \begin{bmatrix} \dfrac{q_{V\phi}\Delta t^3}{3(R_m + h)^2} & \dfrac{q_{V\phi}\Delta t^2}{2(R_m + h)} & 0 & 0 & 0 & 0 \\ \dfrac{q_{V\phi}\Delta t^2}{2(R_m + h)} & q_{V\phi}\Delta t & 0 & 0 & 0 & 0 \\ 0 & 0 & \dfrac{q_{V\lambda}\Delta t^3}{3(R_n + h)^2} & \dfrac{q_{V\lambda}\Delta t^2}{2(R_n + h)} & 0 & 0 \\ 0 & 0 & \dfrac{q_{V\lambda}\Delta t^2}{2(R_n + h)} & q_{V\lambda}\Delta t & 0 & 0 \\ 0 & 0 & 0 & 0 & \dfrac{1}{3}q_{vh}\Delta t^3 & \dfrac{1}{2}q_{vh}\Delta t^2 \\ 0 & 0 & 0 & 0 & \dfrac{1}{2}q_{vh}\Delta t^2 & q_{vh}\Delta t \end{bmatrix}$$

$$\tag{4.36}$$

where the corresponding state vector is $\begin{bmatrix} \delta\phi & \delta\dot{\phi} & \delta\lambda & \delta\dot{\lambda} & \delta h & \delta\dot{h} \end{bmatrix}$ and

$q_{V\phi}, q_{V\lambda}, q_{vh}$ -Spectral density of velocity in each direction

R_m, R_n -Earth radius in meridian and prime meridian directions

h -Station height above ellipsoid

Δt -Time increment

ϕ - Latitude of the GPS station

For the case of first order Guass-Markov, the transition matrix position block takes the form as shown in Equation (4.37):

$$\Phi_{Position\ block} = \begin{bmatrix} 1 & \dfrac{1-e^{-\beta_{v_\phi}\Delta t}}{\beta_{v_\phi}(R_m+h)} & 0 & 0 & 0 & 0 \\ 0 & 1 & 0 & 0 & 0 & 0 \\ 0 & 0 & 1 & \dfrac{1-e^{-\beta_{v_\lambda}\Delta t}}{\beta_{v_\lambda}(R_n+h)\cos\phi} & 0 & 0 \\ 0 & 0 & 0 & 1 & 0 & 0 \\ 0 & 0 & 0 & 0 & 1 & \dfrac{1-e^{-\beta_{v_h}\Delta t}}{\beta_{v_h}} \\ 0 & 0 & 0 & 0 & 0 & 1 \end{bmatrix} \tag{4.37}$$

where

$\beta_{v_\phi}, \beta_{v_\lambda}, \beta_{v_h}$ - correlation time in each direction

Because of the numerous terms in the position block of the noise matrix, it will be presented in three small sub-matrix as illustrated in Figure 4.5. The order is for illustration purposes only.
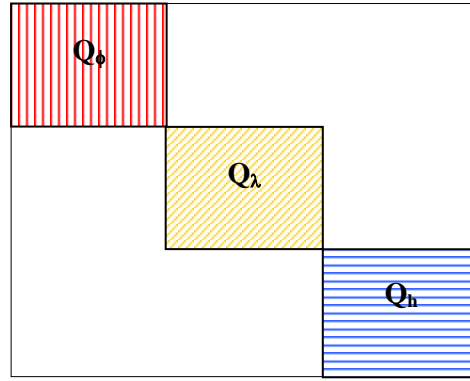
Figure 4.5 Position block

$\mathbf{Q_\phi} =$

$$\begin{bmatrix} \dfrac{q_{V\phi}((\Delta t - \dfrac{2}{\beta_{V\phi}}(1-e^{-\beta_{V\phi}\Delta t}) + \dfrac{1}{2\beta_{Vn}}(1-e^{-2\beta_{V\phi}\Delta t}))}{\beta_{V\phi}^2 (R_m + h)^2} & \dfrac{q_{V\phi}((\dfrac{1}{\beta_{V\phi}}(1-e^{-\beta_{V\phi}\Delta t}) - \dfrac{1}{2\beta_{V\phi}}(1-e^{-2\beta_{V\phi}\Delta t}))}{\beta_{V\phi}(R_m + h)} \\[3em] \dfrac{q_{V\phi}((\dfrac{1}{\beta_{V\phi}^2}(1-e^{-\beta_{V\phi}\Delta t}) - \dfrac{1}{\beta_{V\phi}^2}(1-e^{-2\beta_{V\phi}\Delta t}))}{\beta_{V\phi}(R_m + h)} & \dfrac{q_{V\phi}}{2\beta_{V\phi}}(1-e^{-2\beta_{V\phi}\Delta t}) \end{bmatrix}$$

$$(4.38)$$

$\mathbf{Q_\lambda} =$

$$\begin{bmatrix} \dfrac{q_{V\lambda}(\Delta t - \dfrac{2}{\beta_{V\lambda}}(1-e^{\beta_{V\lambda}\Delta t}) + \dfrac{1}{2\beta_{V\lambda}}(1-e^{-2\beta_{V\lambda}\Delta t})}{\beta_{V\lambda}^2 (R_m + h)^2 \cos^2(\Phi)} & \dfrac{q_{V\lambda}(\dfrac{1}{\beta_{V\lambda}}(1-e^{-\beta_{V\lambda}\Delta t}) - \dfrac{1}{2\beta_{V\lambda}}(1-e^{-\beta_{V\lambda}\Delta t}))}{\beta_{V\lambda}(R_m + h)\cos(\Phi)} \\[3em] \dfrac{q_{V\lambda}(\dfrac{1}{\beta_{V\lambda}}(1-e^{-\beta_{V\lambda}}) - \dfrac{1}{2\beta_{Vn}}(1-e^{-\beta_{V\lambda}\Delta t}))}{\beta_{V\lambda}(R_m + h)\cos(\Phi)} & \dfrac{q_{V\lambda}}{2\beta_{V\lambda}}(1-e^{-2\beta_{V\lambda}\Delta t}) \end{bmatrix}$$

$$(4.39)$$

Qₕ=

$$\left[\begin{array}{cc} \dfrac{q_{V_h}(\Delta t - \dfrac{2}{\beta_{Vh}}(1-e^{-\beta_{V_h}\Delta t}) + \dfrac{1}{2\beta_{V_h}}(1-e^{-2\beta_{V_h}\Delta t})}{\beta_{V_h}^2} & \dfrac{q_{V_h}(\dfrac{1}{\beta_{v_h}}(1-e^{-\beta_{V_h}}) - \dfrac{1}{\beta_{V_h}}(1-e^{-2\beta_{V_h}\Delta t}))}{\beta_{V_h}} \\[4ex] \dfrac{q_{V_h}(\dfrac{1}{\beta_{V_h}}(1-e^{-\beta_{V_h}} - \dfrac{1}{\beta_{V_h}}(1-e^{-\beta_{V_h}}))}{\beta_{V_h}} & \dfrac{q_{V_h}}{2\beta_{V_h}}(1-e^{-2\beta_{V_h}\Delta t}) \end{array}\right]$$

$$(4.40)$$

GPS Receiver Clock Block

Similar to the position block, the transition and the noise matrices for the receiver clock block can be formulated using Random Walk as given in Equations 4.41 and 4.42.

$$\Phi_{Clock\ block} = \begin{bmatrix} 1 & \Delta t \\ 0 & 1 \end{bmatrix} \tag{4.41}$$

$$Q_{Clock\ block} = \begin{bmatrix} \dfrac{1}{3}q_{V_{dt}}\Delta t^3 + q_{V_{dt}}\Delta t & \dfrac{1}{2}q_{V_{dt}}\Delta t^2 \\[2ex] \dfrac{1}{2}q_{V_{dt}}\Delta t^2 & q_{V_{dt}}\Delta t \end{bmatrix} \tag{4.42}$$

where $q_{V_{dt}}$ is the spectral density of receiver clock drift

The case of the first order Gauss-Markov process is given in Equations 4.43 and 4.44.

$$\Phi_{Clock\ block} = \begin{bmatrix} 1 & \dfrac{(1-e^{-\beta_{V_{dt}}\Delta t})}{\beta_{V_{dt}}} \\[2ex] 0 & 1 \end{bmatrix} \tag{4.43}$$

$$Q_{Clock\ block} = \begin{bmatrix} \dfrac{q_{V_{dt}}}{\beta_{V_{dt}}^2}(\Delta t - \dfrac{2}{\beta_{V_{dt}}}(1-e^{\beta_{V_{dt}}dt}) + \dfrac{(1-e^{2\beta_{V_{dt}}\Delta t})}{2\beta_{V_{dt}}}) & \dfrac{q_{V_{dt}}(1-e^{\beta_{V_{dt}}\Delta t})-(1-e^{2\beta_{V_{dt}}\Delta t})/2}{\beta_{dt}^2} \\ \dfrac{q_{V_{dt}}(1-e^{\Delta t})-(1-e^{2\beta_{dt}\Delta t})/2}{\beta_{V_{dt}}^2} & \dfrac{q_{V_{dt}}(1-e^{2\beta_{dt}\Delta t})}{2\beta_{V_{dt}}} \end{bmatrix}$$

$$(4.44)$$

where $\beta_{V_{dt}}$ is the correlation time of the receiver clock drift.

Tropospheric Delay Block

The nature of the troposphere allows for modeling its component as Random Walk. Therefore, the transition matrix and the noise matrix will consist of one element only as illustrated in Equations 4.45 and 4.46:

$$\Phi_{Trop} = [1] \tag{4.45}$$

$$Q_{Trop} = [q_{trop}\Delta t] \tag{4.46}$$

where q_{trop} is the spectral density of tropospheric delay parameter.

Ambiguities Block

The ambiguities are modeled as constant; therefore, there will be a nil noise matrix and an identity transition matrix.

4.6.1.2 No Velocity Estimation

In the case of no parameters rate estimation such as the velocity and clock rate, the equations above will be simplified as given herein. The transition matrix will be equal to

the identity matrix, which means no parameter prediction is applicable. However, parameters' prediction is still feasible through observing their difference over time.

GPS Receiver Coordinates Block

As mentioned above, the transition matrix for the GPS station coordinates will be the identity matrix. The noise matrix for the case of random walk is illustrated in equation 4.47:

$$Q_{Position\ block} = \begin{bmatrix} \dfrac{q_\phi \Delta t}{(R_m + h)^2} & 0 & 0 \\ 0 & \dfrac{q_\lambda \Delta t}{(R_n + h)^2 \cos^2 \phi} & 0 \\ 0 & 0 & q_h \Delta t \end{bmatrix} \tag{4.47}$$

In the case of using first order Guass-Markov, the transition matrix will be also the identity matrix and the noise matrix as depicted in Equations 4.48 to 4.51.

$$Q_{Position\ block} = \begin{bmatrix} Q_\phi & 0 & 0 \\ 0 & Q_\lambda & 0 \\ 0 & 0 & Q_h \end{bmatrix} \tag{4.48}$$

$$Q_\phi = \left[\frac{q_\phi (1 - e^{-2\beta_\phi \Delta t})}{2\beta_\phi^2 (R_m + h)^2} \right] \tag{4.49}$$

$$Q_\lambda = \left[\frac{q_\lambda (1 - e^{-2\beta_\lambda \Delta t})}{2\beta_\lambda (R_m + h)^2 \cos^2 \phi} \right] \tag{4.50}$$

$$Q_h = \left[\frac{q_h (1 - e^{-2\beta_h \Delta t})}{2\beta_h} \right] \tag{4.51}$$

GPS Receiver Clock Block

The transition matrix of the GPS receiver clock will take the form given in Equation 4.52 for the case of RW and the form depicted in Equation 4.53 for the case of first GM.

$$Q_{Clock\ block} = \left[q_{dt} \Delta t \right] \tag{4.52}$$

$$Q_{Clock\ block} = \left[\frac{q_{dt}(1 - e^{-2\beta_{dt}\Delta t})}{2\beta_{dt}} \right] \tag{4.53}$$

Tropospheric Delay Block

The estimation for the rate of change of the tropospheric delay is not considered. Therefore, no change is applicable to the noise matrix as shown in Equation 4.54.

$$Q_{Trop} = [q_{trop} \Delta t] \tag{4.54}$$

An empirical way to choose the spectral density of a parameter under consideration is to attribute the value of its spectral density to the rate of change of the parameter (velocity). For example, if a GPS receiver is attached to a vehicle moving with a speed between 60 to 100 km/h, the spectral density can be chosen to be between $(60x1000/(60x60))^2$ to $100x1000/(60x60))^2$, i.e. $2.8x10^2$ and $7.7x10^2$ m^2/sec, respectively. Another example is to assume the rate of change of tropospheric delay as 1 cm/hr, then the spectral density of the tropospheric delay can be assumed $(0.01/(60x60))^2$, i.e. $7.7x10^{-12}$ m^2/sec.

Ambiguities Block

The ambiguities are modeled as a constant, so ignoring velocity estimation has no effect on neither the transition matrix or the noise matrix.

4.7 Quality Control

One of the essential elements of navigation and positioning systems is the ability to tolerate and detect any anomaly in observations. Therefore, this section deals with the detection of cycle slip from carrier phase observations and the overall detection of any measurements with big errors.

4.7.1 Cycle Slip Detection

Cycle slip is a failure of the GPS receiver to count a small number of cycles caused by motion dynamic, scintillation, GPS firmware performance, or weak signals. Consequently, the range from receiver to satellite is erroneous up to the unaccounted cycles. Several methods can be used to detect cycle slip. Among them are monitoring the difference between code and carrier phase measurements, using Doppler observations to predict the carrier phase observations, monitoring the difference between the two carrier phase GPS observations, or observing the difference between the narrow and wide lane

combinations of L1 and L2 observations over time. For PPP, the latter technique is used because of its performance (Collins et al., 2001).

4.7.2 Blunder Detection

It is essential to have an approach that can validate and identify the assumed mathematical model from any defect. As a result, testing the performance of Kalman filter is necessary. The proper method is to use the innovation sequence. The innovation sequence can be defined as the difference between the actual and predicted outputs as shown in Equation 4.55.

$$v_k = y_k - A_k x_k^-$$
(4.55)

where

v_k - innovation sequence vector

y_k - new measurements vector

Being an optimal filter, the resultant innovation sequence must be Gaussian. Therefore, any anomaly in the Kalman filter performance will be reflected in the innovation sequence. Thus, a goodness of fit test is used to identify model consistency. If the model did not pass the test, then a local test should be conducted to identify the measurement that is likely erroneous. The observation corresponding to the maximum value of the local test is most likely the outlier. The formulas for these tests are given in Equations 4.56 and 4.57 (Teunissen and Salzmann, 1988).

Global Test:

$$T = v_k^t C_{vk} v_k \mid T < \chi_\alpha^2(m_k, 0)$$
(4.56)

Local Test:

$$w = \frac{(v_k)_i}{\sqrt{(C_{vk})_{ii}}}$$

<div align="right">(4.57)</div>

where,

$$C_{vk} = (R_k + H_k P_k(-)H_k^T)$$

α - level of significant

m_k - degrees of freedom

$\chi_\alpha^2(m_k,0)$ - upper α probability point of the Chi-squared distribution

H_k - design matrix

R_k - observations variance covariance matrix

$P_k(-)$ - predicted parameter variance covariance matrix

This chapter presented the functional and stochastic models for the proposed PPP system. Using these models, the next chapter will present numerical results based on the investigation and development of the previous models.

CHAPTER 5

PPP RESULTS UNDER VARIOUS DYNAMIC CONDITIONS

This chapter presents the positioning results and analysis for the developed PPP software. These results and analysis include static, land vehicle, marine, and airborne GPS datasets. The data has different dynamic characteristics and therefore is a good benchmark for the system. The traditional PPP model is used in this chapter.

5.1 PPP Static Results

Twelve stations from the IGS GPS network (see Figure 5.1) were used to demonstrate the positioning accuracy of PPP. A one day GPS dataset at an interval of 30 seconds was retrieved from each station on August 1st, 2004. The final IGS orbit and clock corrections at intervals of 15 minutes and 30 seconds, respectively, were used to remove the orbit and clock errors. A unified estimation scheme was adopted for all the stations. In this scheme, a Random Walk process is used for position, tropospheric delay, and receiver clock errors while a constant process is used for the ambiguities. The spectral density of the GPS station coordinates was assumed to be zero because the station is static, and the GPS station coordinate uncertainty was assumed to be 2 km. The tropospheric delay initial uncertainty was assumed to be a half meter and its spectral density was assumed to be 10^-

^{9} m^2/sec. The clock error spectral density was assumed 10^5 m^2/sec and with initial uncertainty of 10^5 m. These big values were selected for the receiver clock to account for the one-millisecond jumps, which occur when a GPS receiver does not steer its internal clock and allows it to drift controllably. These clock parameters were adopted for all the tests in this chapter. The precision of pseudorange and carrier phase observations were assumed to be 0.3m and 3mm, respectively. An elevation cut off angle of 10 degree was used in this test. The types of the used GPS receivers and antennas are shown in Table 5.1. The assumed values for the parameters are the optimum and suitable for many datasets. The selection of these values is based on the discussion given at the end of Section 4.6.
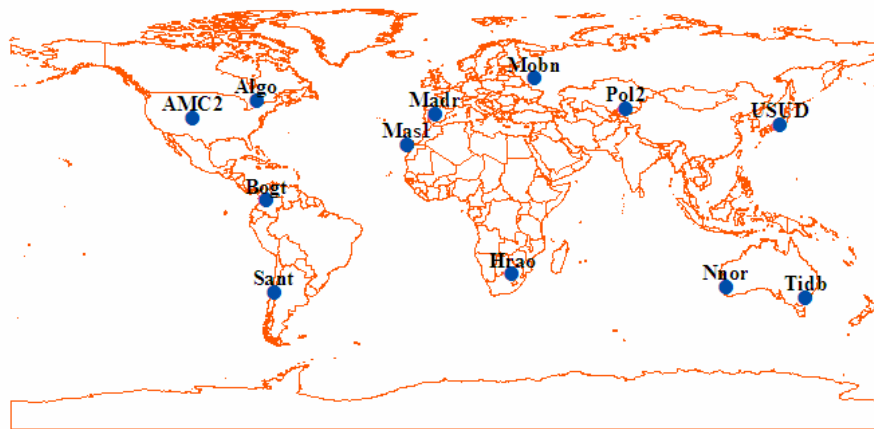
Figure 5.1 Map of the used static IGS stations

The receiver antenna phase center offset and variation obtained from IGS were used to mitigate any dependent effect in the entire chapter. The antennas of the used IGS stations are AOAD/M_T and ASH701945C_M. They have the same values of the antenna phase centers and phase center variations. These values are 110, and 128 mm for L1 and L2

respectively, where the phase center variations are zeros (IGS, 2004c). The average

Geometric Dilution Of Precision (GDOP) value for the GPS constellation at the used IGS

stations was within the range of 2.3 to 3.2. The positioning results are summarized and

illustrated in Figure 5.2. The figure also demonstrates the bias and standard deviation for

each station. It is worth mentioning that the coordinates of the IGS stations are known

and have accuracy of few millimeters. The numbers are truncated to the nearest

centimeter for simplicity.

Table 5.1 IGS GPS receivers and antenna types

Station	Receiver type	Antenna type
ALGO	AOA BENCHMARK ACT	AOAD/M_T
AMC2	ASHTECH Z-XII3T	AOAD/M_T
BOGT	ASHTECH Z-XII3	AOAD/M_T
SANT	ASHTECH Z-XII3	AOAD/M_T
MADR	ASHTECH Z-XII3	AOAD/M_T
MAS1	ASHTECH Z-XII3	AOAD/M_T
MOBN	ASHTECH Z-XII3	ASH701945C_M
HRAO	ASHTECH Z-XII3	AOAD/M_T
POL2	ASHTECH Z-XII3	ASH701945C_M
USUD	ASHTECH Z-XII3	AOAD/M_T
NOOR	ASHTECH Z-XII3	ASH701945C_M
TIDB	ASHTECH Z-XII3	AOAD/M_T
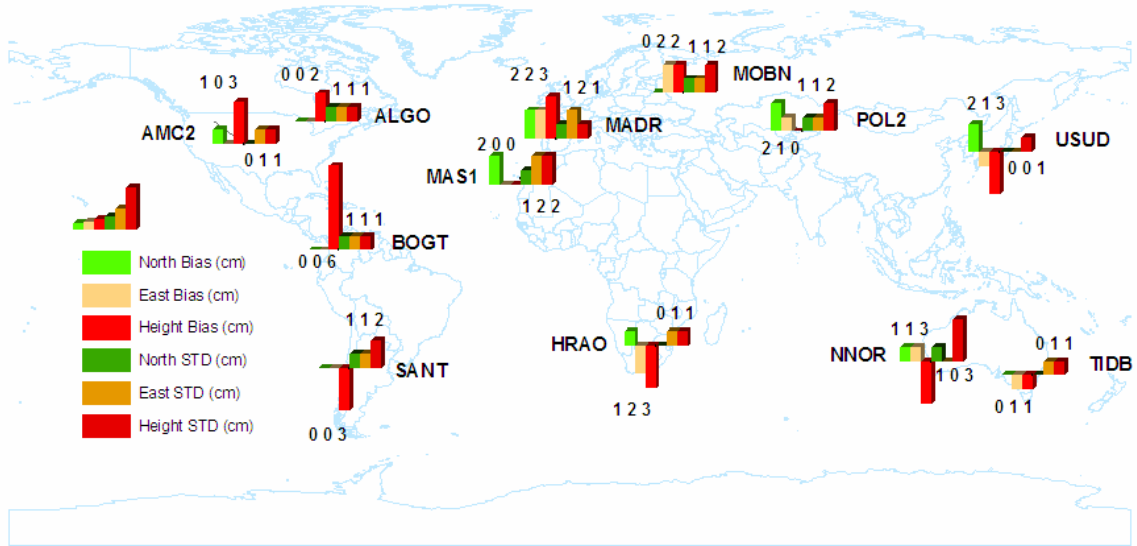
Figure 5.2 IGS stations positioning results

The largest error occurred at the IGS station BOGT. The ephemeris file of this station was missing so automatic ephemerides file was used instead. The unavailability of the ephemeris file might be caused because of receiver data corruption. The automatic ephemeredes file contains the ephemeris of all GPS satellite, despite it is visible at the tracking station or not. This automatic ephemerides file can be formed by combining several ephemerides files obtained from different places of the world. The statistics of the results show centimeter positioning accuracy and are summarized in Table 5.2.

Table 5.2 Summary of IGS station results

Station	Bias (mm)			STD (mm)		
	North	East	Height	North	East	Height
ALGO	2	0	16	4	7	13
AMC2	6	4	35	3	7	8
BOGT	4	-3	57	5	6	14
SANT	4	-4	-29	11	9	21
MADR	17	21	34	11	18	15
MAS1	20	-3	1	6	16	23
MOBN	0	17	23	12	14	17
HRAO	13	-25	-28	2	10	10
POL2	19	11	3	5	14	15
USUD	2	-11	-30	3	4	8
NNOR	8	9	-32	7	5	25
TIDB	4	-7	-5	4	6	9

These results are independent of base stations, first order ionosphere activities, troposphere variability (to some extent), location, and time. In addition, as mentioned a unified estimation scheme is used for the station coordinates, clock offset, troposphere, and ambiguity all over the data. The intention of using a single estimation scheme is to demonstrate that PPP is flexible and does not need special tuning for each data. This flexibility is important because in reality the values of the parameters are unknown. In summary, PPP virtually eliminates the need to perform any double difference baseline processing and can help in installing control points and updating spatial reference frames with centimeter accuracy.

5.2 Positioning with Land Vehicle Data

A land vehicle equipped with a Javad dual GPS frequency receiver was operated for less than two hours at Springbank near Calgary on September 30, 2003. The data has a sampling rate of 1 second and cut off angle of 10 degrees. The average GDOP value of the satellites was 2.4. The topographic nature of the area includes variations in height that reach about 160 m. This vehicle trip included several minutes of static periods. Parallel to the PPP test, a base station at a known control point was installed to allow qualitative and quantitative assessment of PPP results through the use of Double Difference (DD) software. The GrafNav™ is the software that was used to produce the reference trajectory. The software can output station positions based on different criteria such as the status of DD ambiguity and/or the precision of the solution. The second option was used because in most of the epochs the DD ambiguities were fixed and therefore epochs with DD ambiguity fixing and precision better than 10 cm were used to benchmark the PPP solutions. This threshold of precision was chosen to ensure the existence of sufficient epochs of the DD solution that can be used to assess the positioning accuracy of PPP. A smaller threshold such as 5 cm would produce a small number of DD solution epochs. The estimation scheme that was used for PPP solution assumed 2 km uncertainty for the initial GPS station coordinates. To account for the vehicle dynamic, spectral densities of 10^3 and 10^2 m^2/sec were used for the horizontal and the height parameters of the station. Tropospheric delay was assumed to be known with an uncertainty of a half meter and a spectral density of 10^{-9} m^2/sec. The Random Walk (RW) process was used to model the

dynamics of the vehicle. The selection of these values of the spectral density is based on the empirical method given at the end of Section 4.6. As mentioned in Chapter 4, the use of RW or GM process is common in the GPS field. When dealing with systems that include behaviors such as sudden trajectory variations or clock jumps, RW process can be suitable. Tropospheric delay does not, normally, change suddenly, therefore many researchers can model it as RW or GM. Actually, the noise matrices in both models are almost equivalent in the case of GPS positioning due to the long correlation time of the parameters. During the experiment, there were signal losses of lock for the GPS base station; thus, the DD solution was affected for a few minutes because the DD processing needs simultaneous signals lock for the base and the rover stations. On the contrary, the PPP solution is independent of the base station and so was unaffected. Figure 5.3 shows the trajectory of the test.
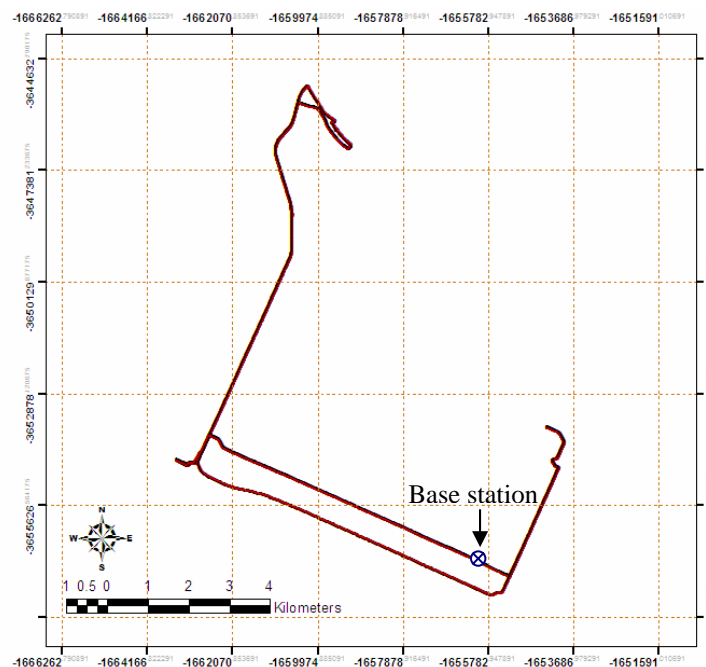
Figure 5.3 Land vehicle trajectory

Figures 5.4, 5.5, and 5.6 depict the quality of the DD solution through illustrating the rover forward and reverse DD position separations and the ambiguity fixing status for the DD forward and reverse solutions. These figures are produced by GrafNav^{TD} software. The gaps in the mentioned figures indicate that the accuracy of the DD solution was more than the 10 cm threshold.
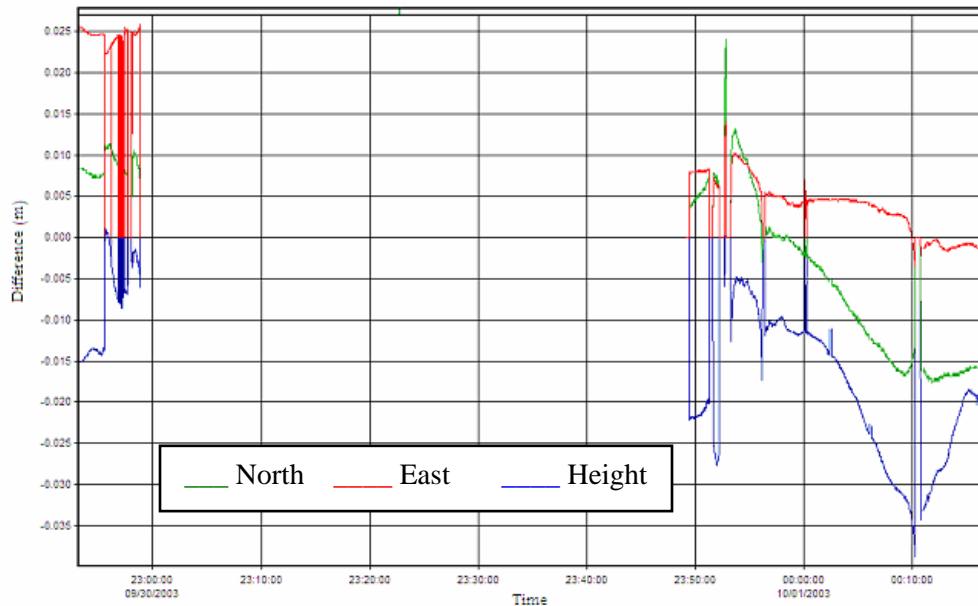
Figure 5.4 Difference between DD forward and reverse solutions
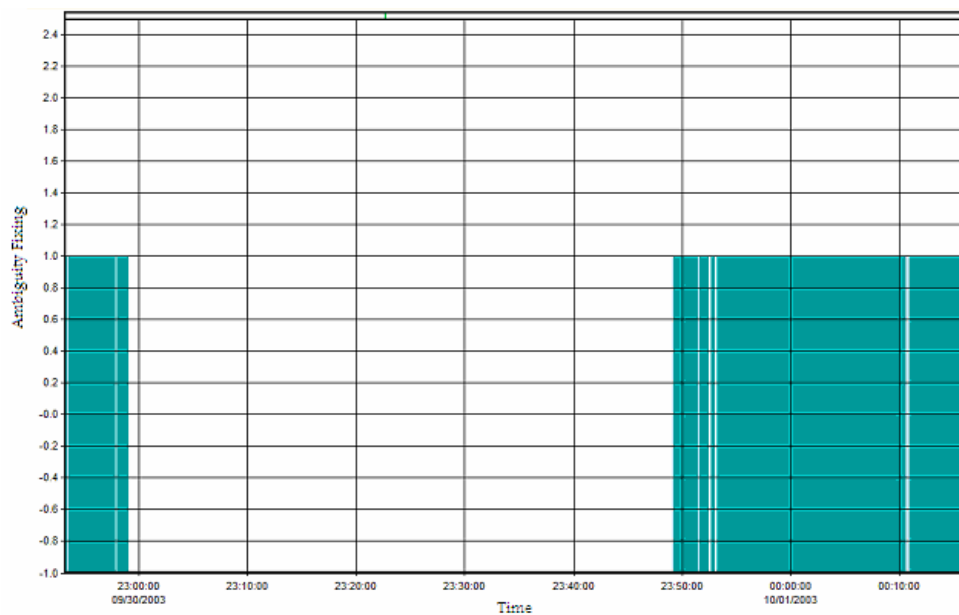
Figure 5.5 Ambiguity fixing for the forward solution
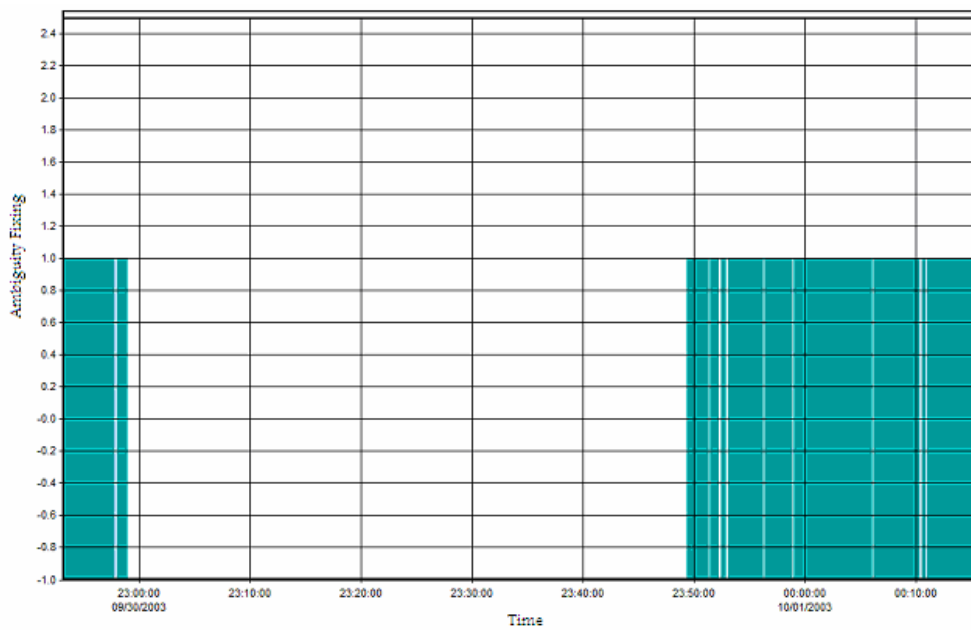
Figure 5.6 Ambiguity fixing for the reverse solution

Figure 5.7 shows the difference between the PPP forward solution and DD combined solution. The figure does not include the first 10 minutes of PPP processing, which

depicts the PPP's convergence behavior. The final IGS precise orbit and clock were used in this test and have sampling intervals of 15 and 5 minutes, respectively. The 30 second clock solution was unavailable at that date because the IGS analysis centers started to produce this clock solution on April 4, 2004, and this vehicle test was done on September 30, 2003. Therefore, the positioning results could be further enhanced with the availability of higher rate of clock corrections. The consistency between the two results excluding the first 10 minutes is shown in Table 5.3.
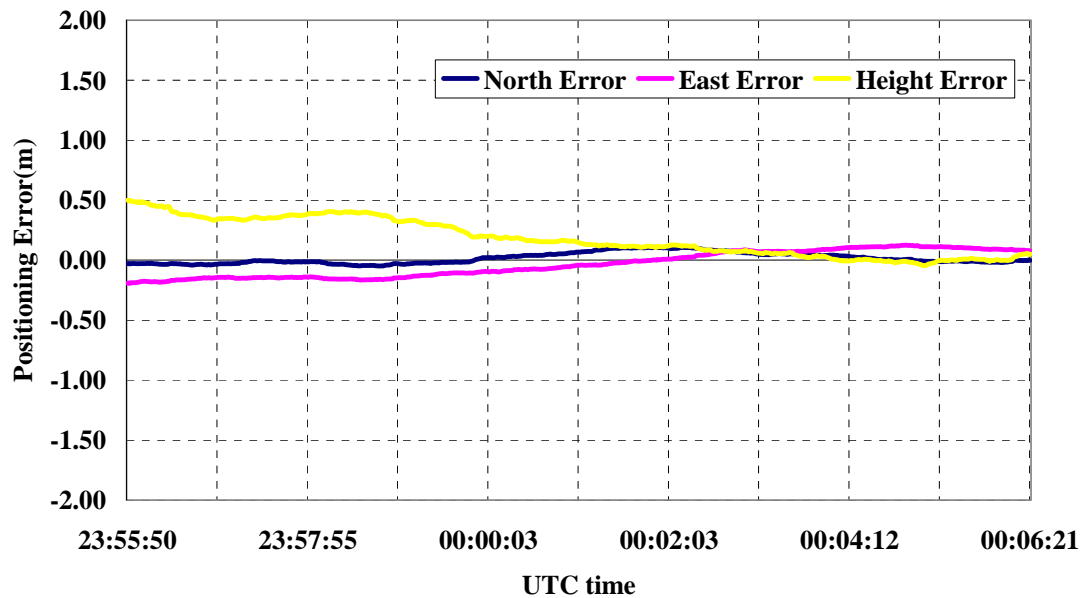
Figure 5.7 Positioning difference with respect to the DD solution

Table 5.3 Summary of vehicle positioning accuracy with respect to DD solution

	Latitude error (cm)	Longitude error (cm)	Height error (cm)
Bias	1	-3	18
STD	4	10	15

Figure 5.8 depicts the 3D positioning difference between the epochs of the GPS double difference solution that has accuracy better than 10 cm and their counterbalance from the PPP solution. The colors of the trajectory show the 3D positioning difference between the PPP forward solution and the GrafNav DD combined solution. The degradation of the colors shows the convergence behaviors of the solution. The figure shows that the positioning accuracy enhances as the time elapsed. A part of the trajectory was masked because a large portion of the DD positioning accuracy exceeded the 10 cm.
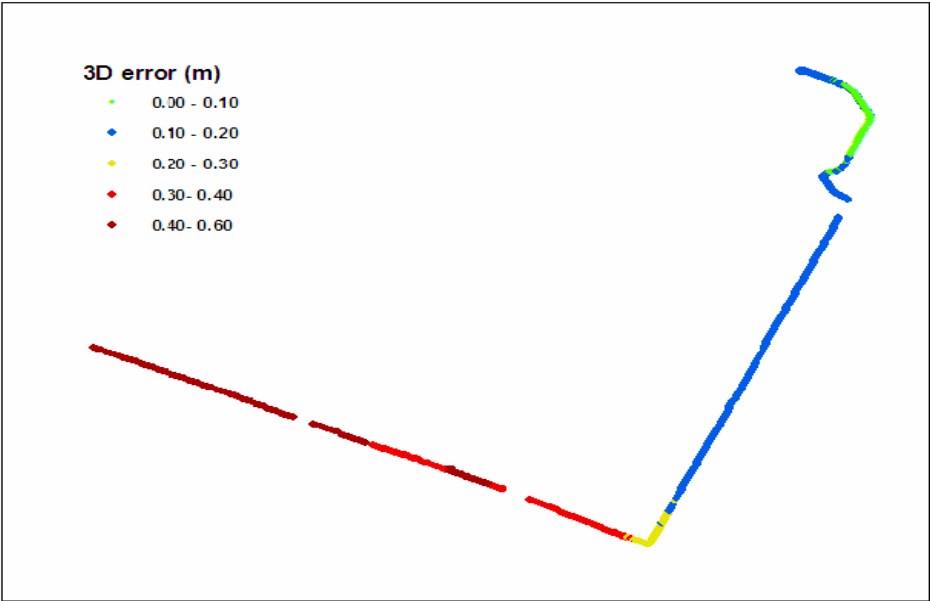
Figure 5.8 PPP-DD 3D offset of the vehicle trajectory

Accordingly, it is important to understand the expected practical accuracy of DD solution in kinematics mode. Figure 5.9 illustrates the height profile of the rover and the base-rover separation. From the figure, it can be concluded that the portion of the DD solution with base line separation less than 10 km was the one used in the comparison. In other

words, the DD solution when the baseline separation was larger than 10 km was not good. A discussion for the DD reference trajectory is presented at the end of the chapter.
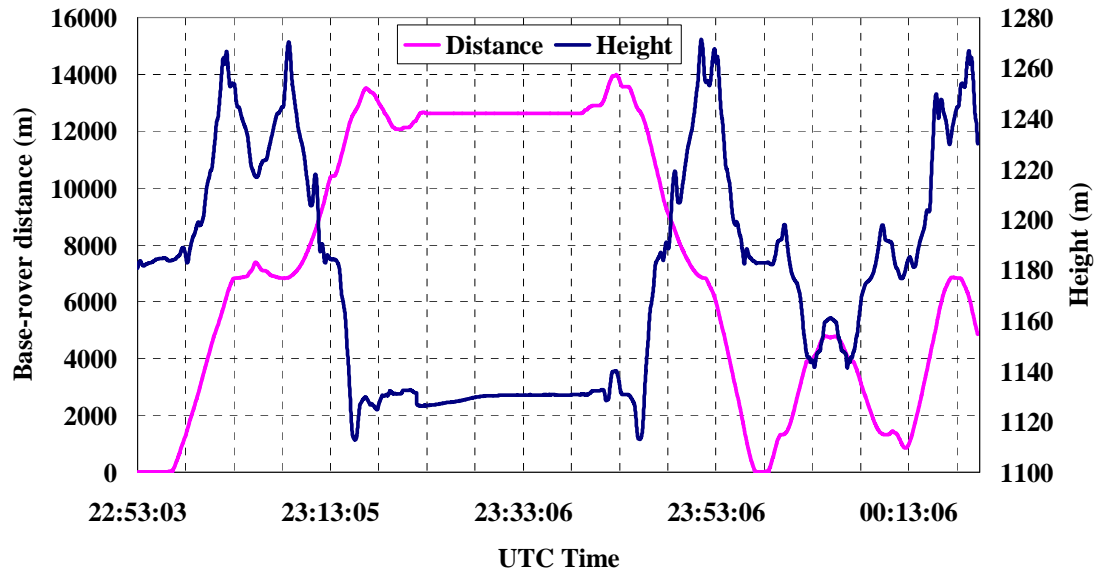
Figure 5.9 Base-rover distance and the height profile of the rover station

5.3 Positioning with Marine Data

For this purpose, 6 hours of 1 second GPS marine data were collected by C&C Technology on August 13, 2003. The receiver used in this test was C-Nav receiver. The GPS constellation during this 6 hours observations period has an average GDOP value of 2.2. An estimation scheme that assumed spectral density for the GPS station horizontal and height components of 10 and 0.2 m^2/s was used. The spectral density of troposphere was assumed to be 10^{-12} m^2/sec. Station coordinates and troposphere were assumed known with accuracy of 2 km and 0.5 m, respectively. The reasons for the selection of these values are the slow motion of the marine vehicle and the small changes in height

profile. A DD solution obtained from processing the marine vessel with respect to a known base station was used to assess the accuracy of PPP solution. The trajectory of the marine vessel is shown in Figure 5.10.
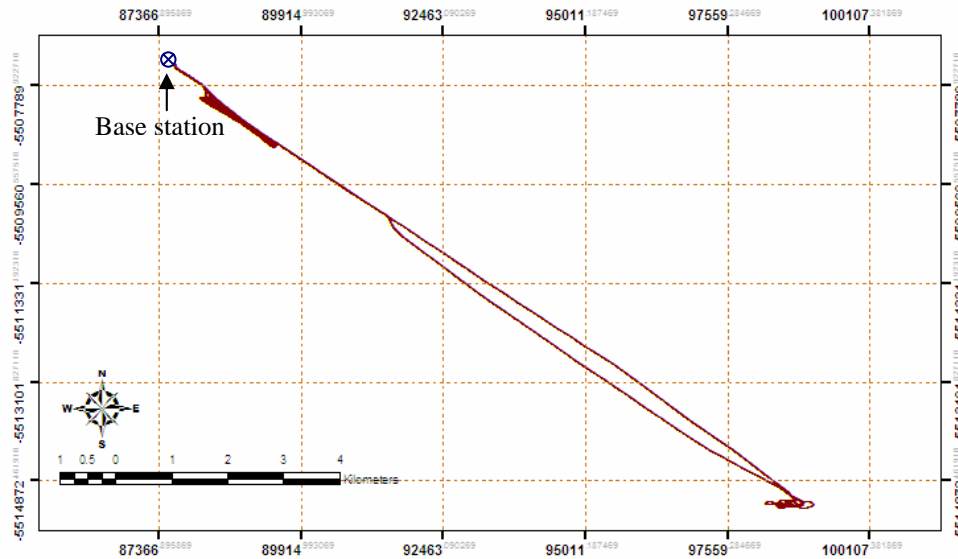
Figure 5.10 Marine vessel trajectory

Figures 5.11, 5.12, and 5.13 depict the accuracy of the DD solution in terms of forward and reverse positioning differences as well as ambiguity fixing status. These figures were obtained using GrafNav software. During this test, ambiguity fixing was successful most of the time.

Figure 5.11 Difference between DD forward and reverse position solutions
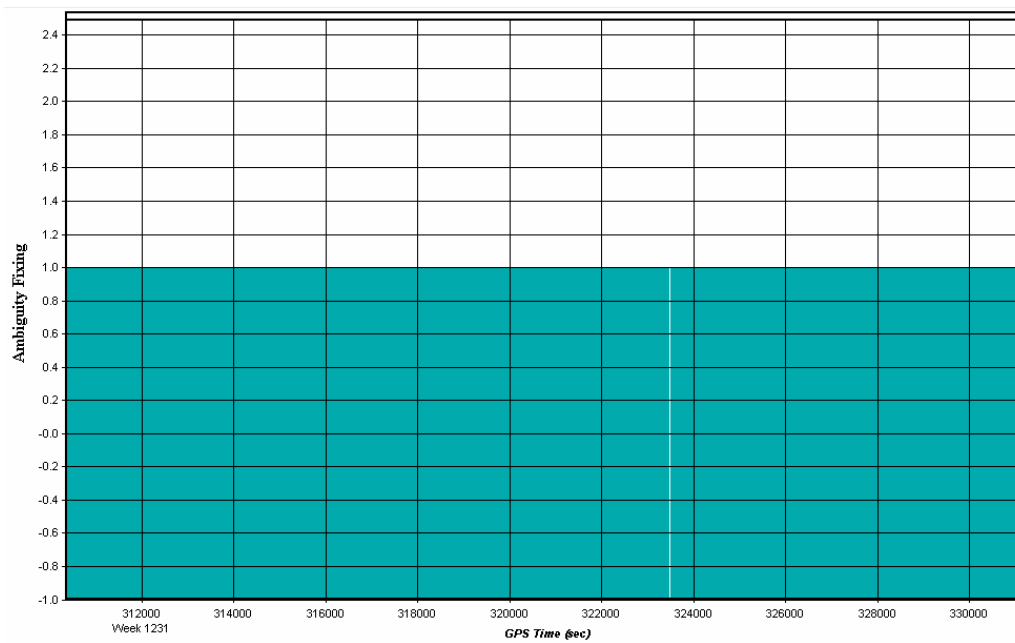
Figure 5.12 Ambiguity fixing for the forward solution

Figure 5.13 Ambiguity fixing for the reverse solution

The consistency between the DD and the PPP solutions is depicted in Figure 5.14. This figure shows the positioning differences between the PPP and DD solutions with positioning accuracy of the latter is better than 10 cm. The statistics of the results suggested biases of 1, 1, -5 cm in addition to standard deviations of 4, 10, and 14 cm for latitude, longitude, and height, respectively. A part from the position errors can be attributed to the DD solution because different GPS antenna brands were used for the rover and the base. As mentioned, the base GPS station consists of C-Nav receiver and its antenna where the base was equipped with ASHTECH UZ-12 and unknown antenna. The 3D error shown on the trajectory is provided in Figure 5.15.
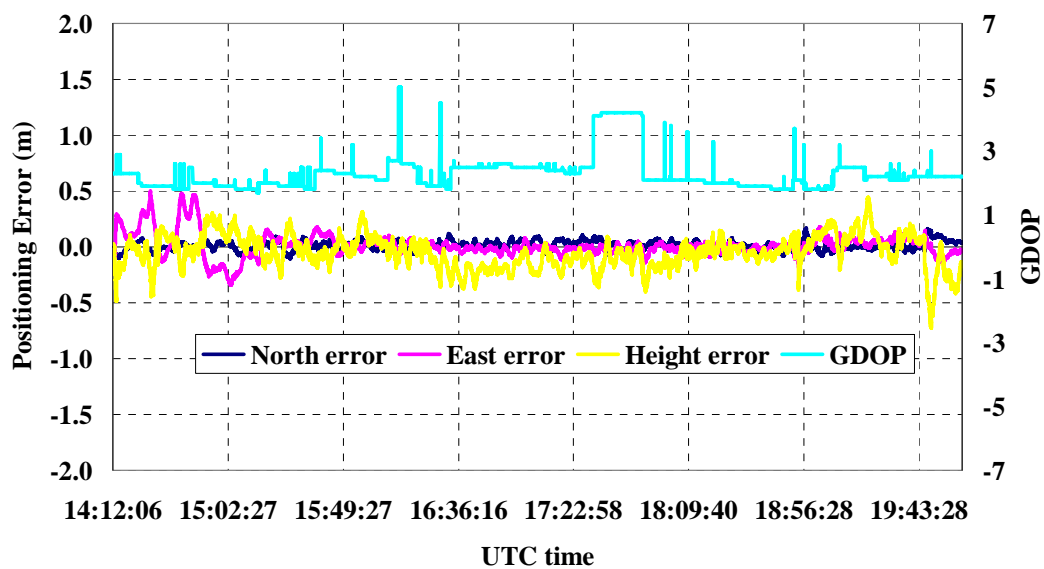
Figure 5.14 Marine dataset positioning accuracy with respect to DD solution
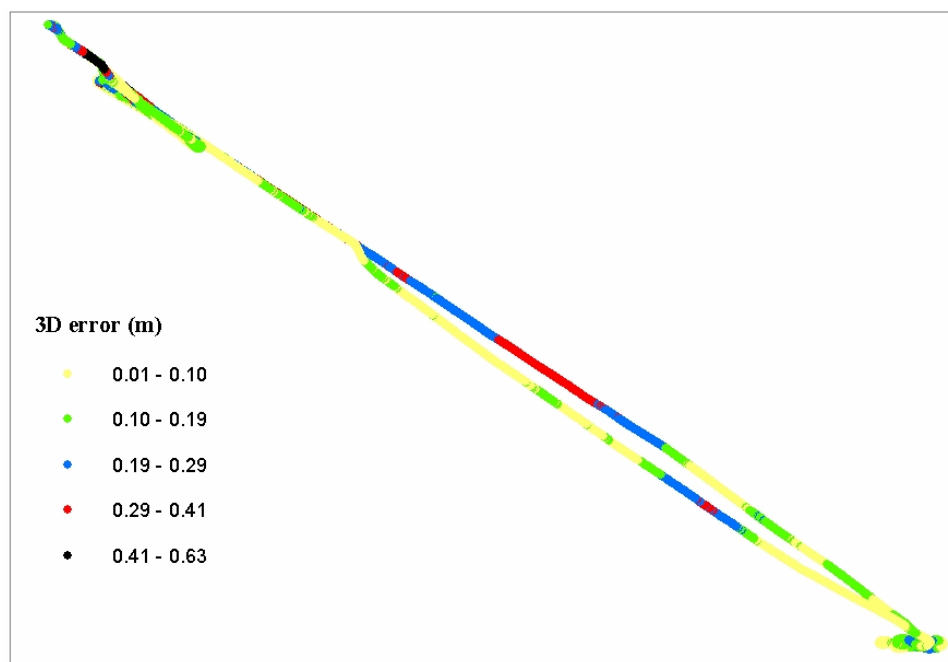
Figure 5.15 Marine trajectory PPP-DD 3D offset

The red color shown in Figure 5.15 originated, mostly, from the beginning of the vessel motion (north west to south east) which can be observed also at the beginning of Figure 5.14, where a noisy horizontal solution is observed compared with the rest of the solution. The other two remaining portions of the trajectory that are colored in red are mainly due to changes in satellites geometry.

5.4 Positioning with Airborne Data

Four hours of airborne GPS data collected on August 28, 2003 by Applanix Corporation were used in this test. The data has frequency of 1 Hz and an average GDOP value of 2.4. NovAtel GPS receiver and antennas were used at the rover stations. The trajectory of the aircraft is shown in Figure 5.16. This dataset contains several states of dynamics: static when the airplane was on the run way; high dynamics during take off, landing, and maneuvering; and high speed but stable during the remaining portions of the flight. A different estimation scheme compared to that of the land vehicle was used herein. In this scheme, large spectral densities of 10^4 and 10^3 m^2/sec were considered for the horizontal and the height parameters of the station to consider the high dynamics of the aircraft. The troposphere and clock spectral densities were chosen to be 10^{-9} and 10^5 m^2/s, respectively. The values of the chosen spectral density are corresponding to the best positioning result and the empirical method given at the end of Section 4.6. The data of the airplane are processed in DD mode with respect to a base station operating NovAtel GPS receiver using GrafNav software. The positioning results obtained from PPP were compared with the counterpart from the DD processing that has a positioning accuracy better than 10 cm

and characterized with successful ambiguity fixing. Figures 5.17, 5.18, and 5.19 illustrate

the reliability of the DD solution. Compared to the other datasets, the difference between

the forward and backward solutions is small which reflects better DD results.
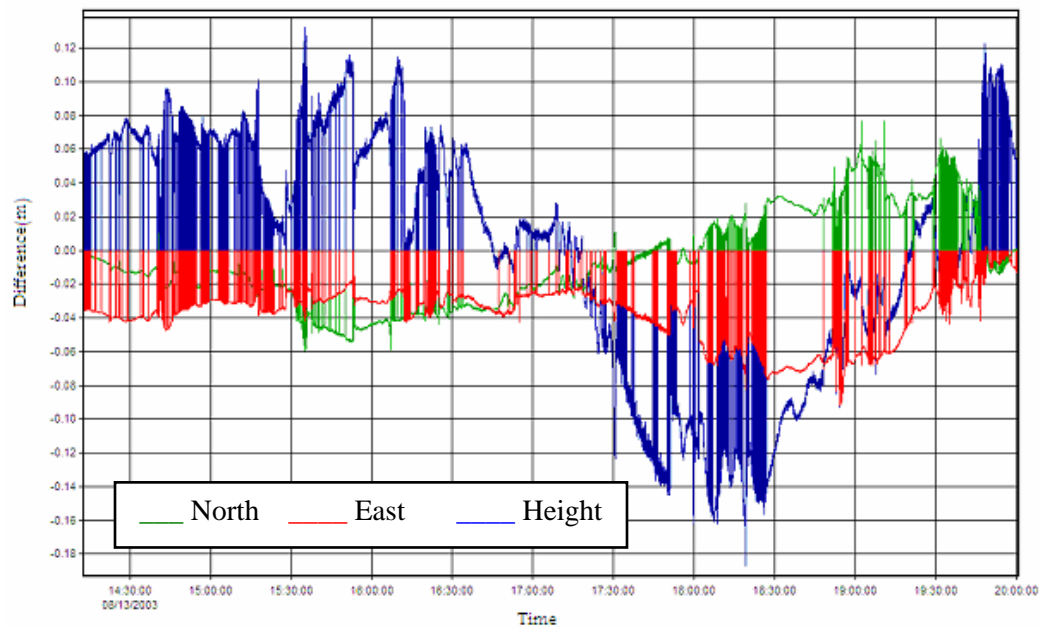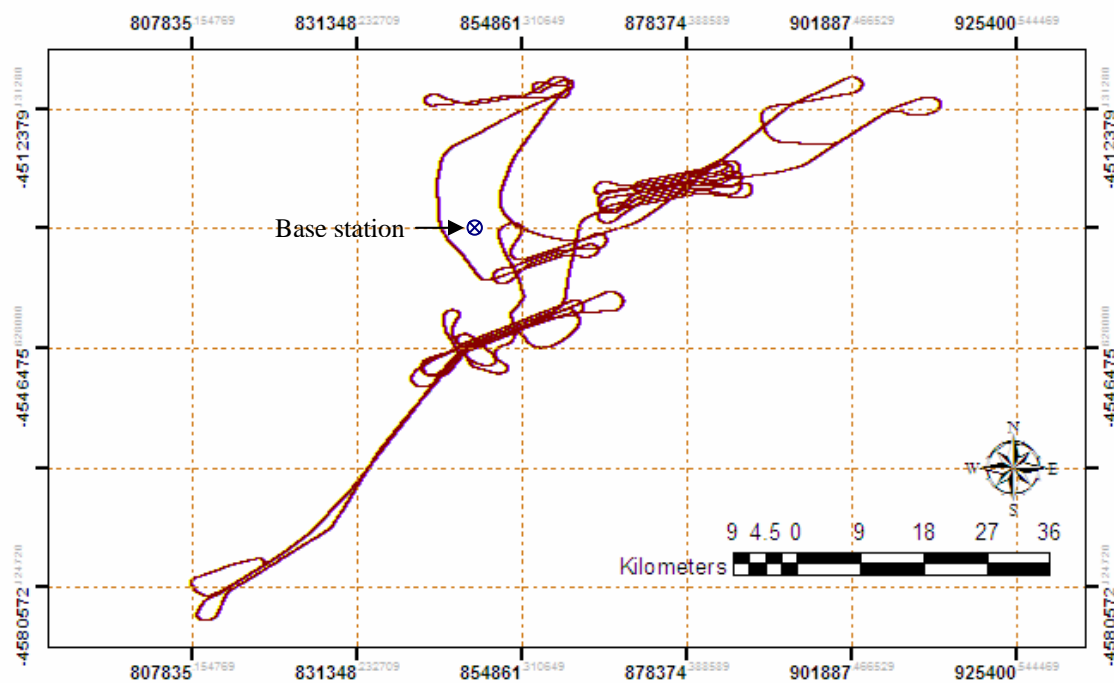

Figure 5.16 Airborne GPS station trajectory
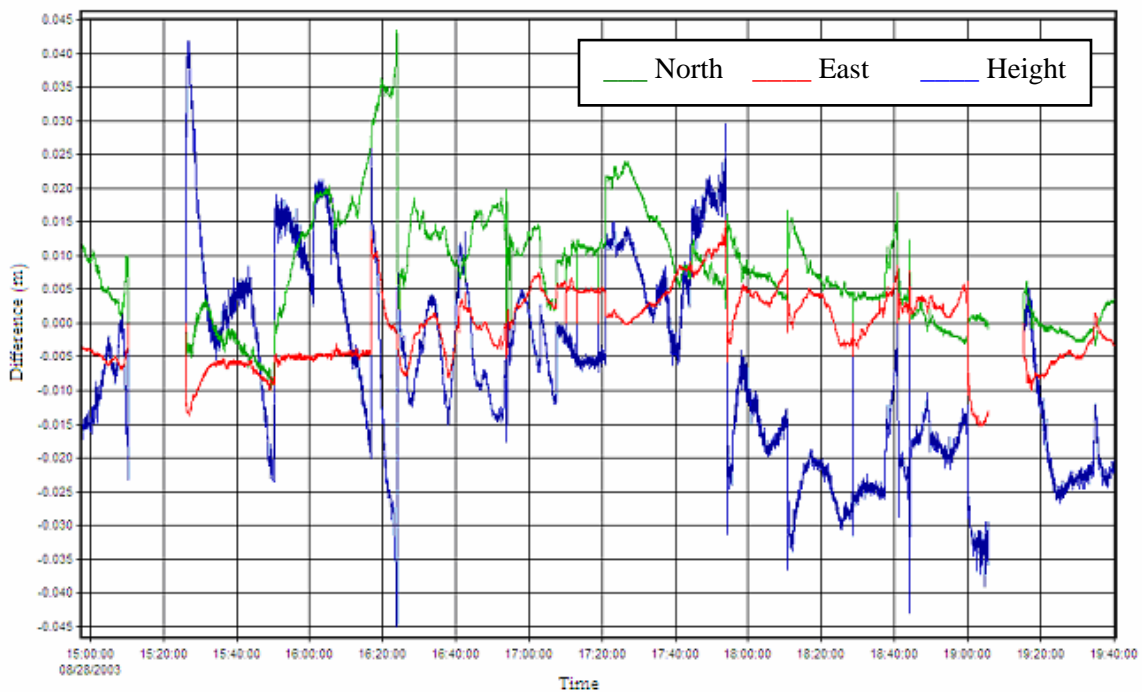
Figure 5.17 Difference between DD forward and reverse solutions
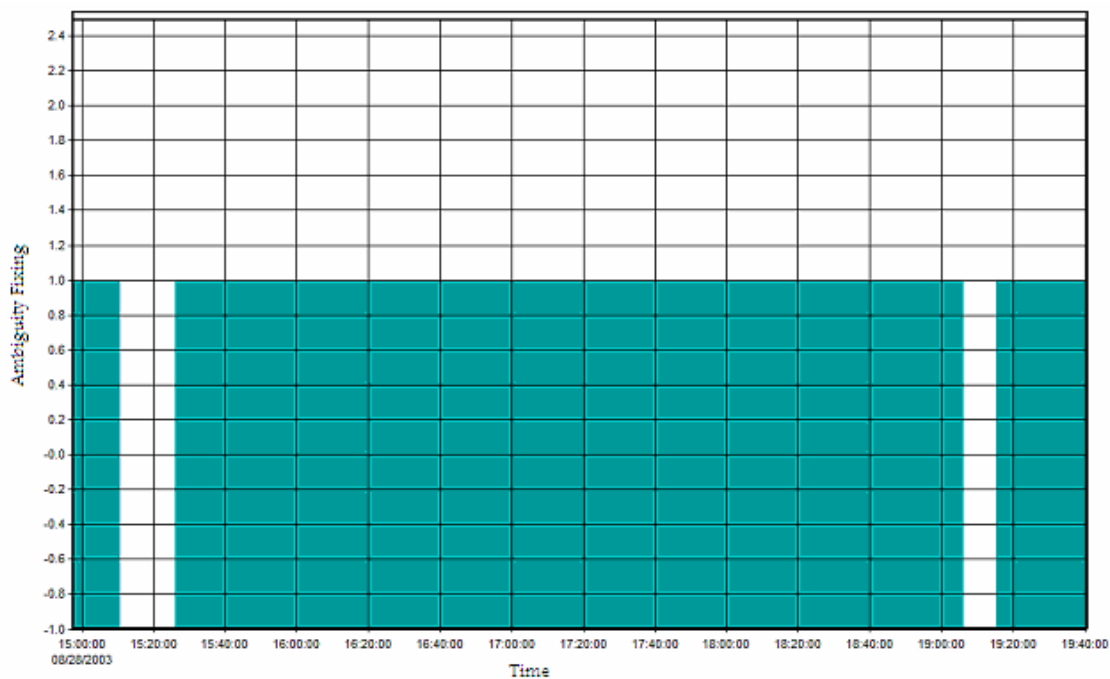
Figure 5.18 Ambiguity fixing for the forward solution

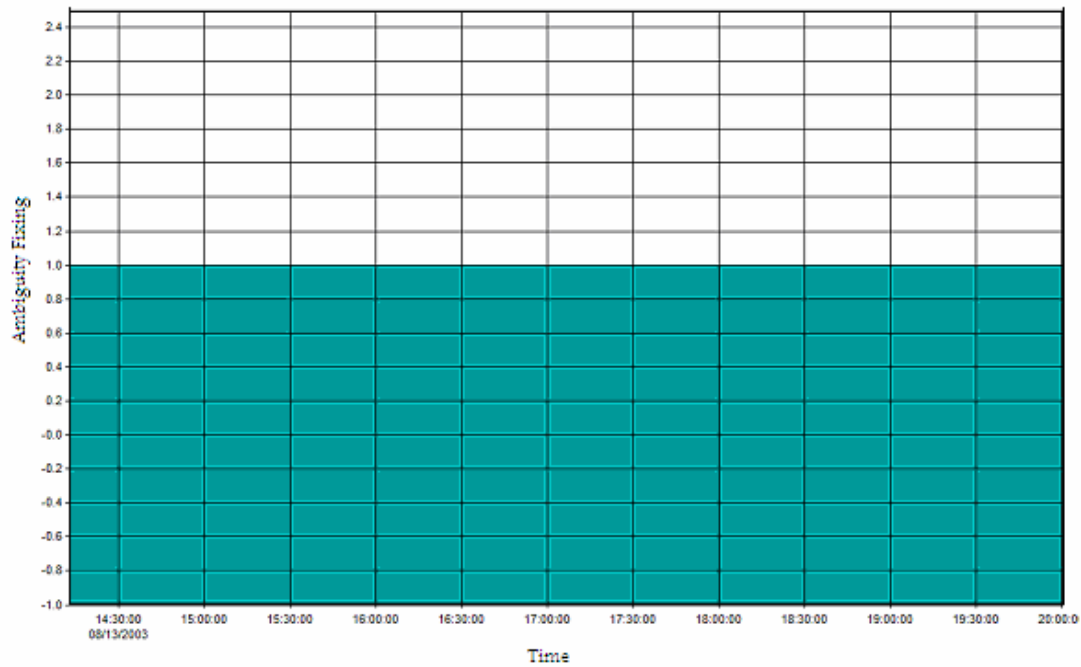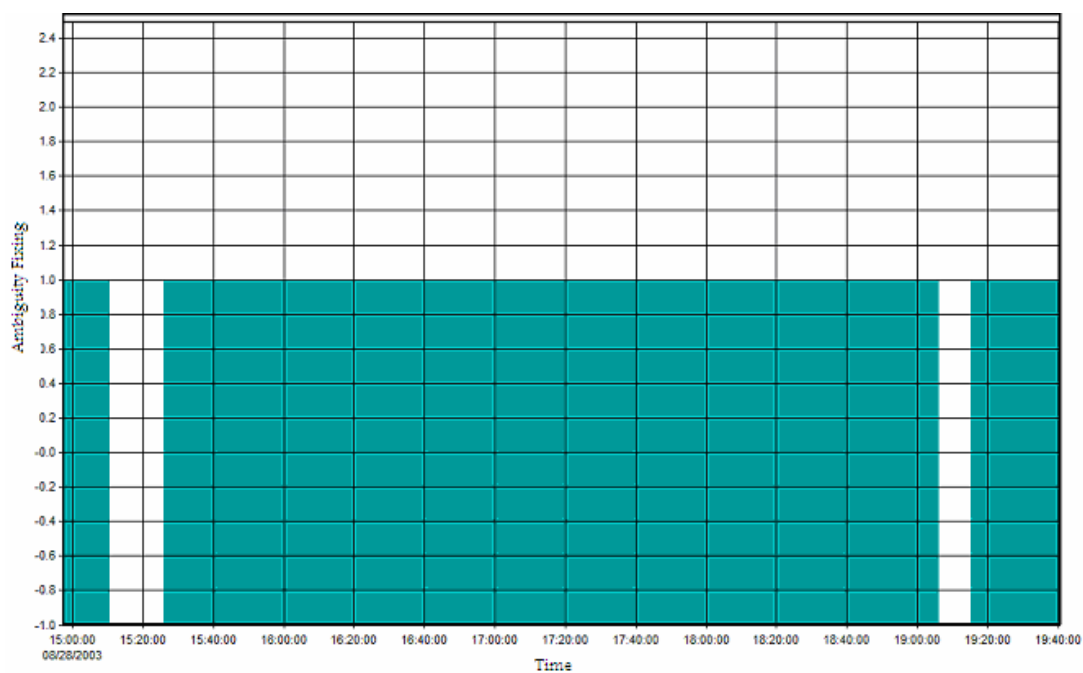Figure 5.19 Ambiguity fixing for the reverse solution

The statistics of the results shown in Figure 5.20 suggested biases of -1 cm, -1 cm, and 1 cm in addition to standard deviations of 3 cm, 6 cm, and 15 cm for latitude, longitude, and height, respectively. The trajectory overlaid by the 3D positioning error is shown in Figure 5.21.
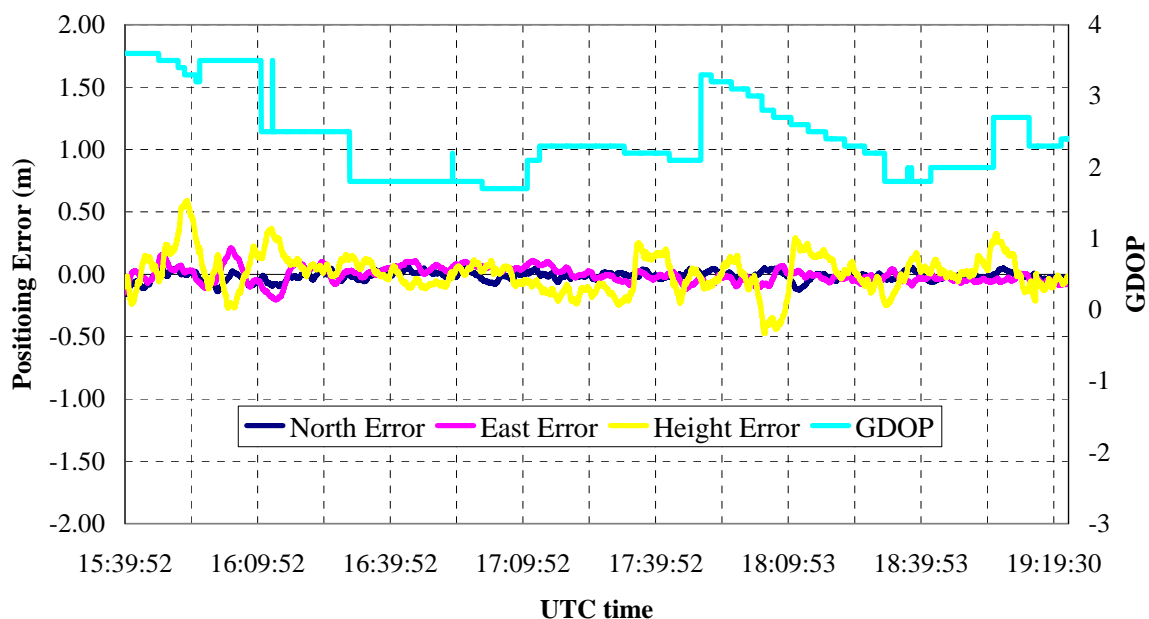
Figure 5.20 Airborne dataset positioning accuracy with respect to DD solution
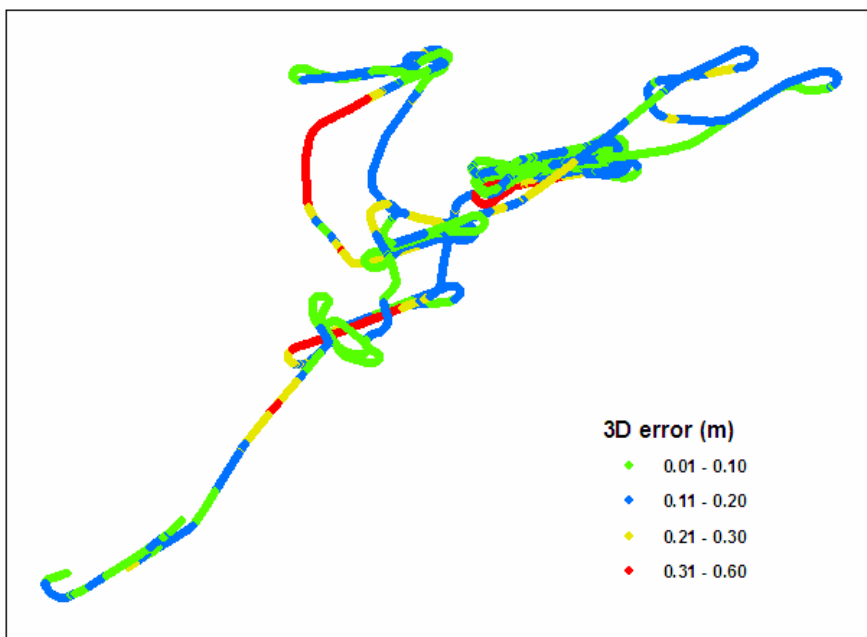
Figure 5.21 PPP-DD 3D offset of the airborne trajectory

5.5 Positioning with Helicopter Data

Two and half hours of 1 second GPS data that were obtained from a receiver carried by a helicopter is used in this section to assess the PPP performance. The GDOP value during the observations period was 2.6. The same estimation scheme that used for airborne data was used here because both of them include high dynamics. Only the spectral density of the troposphere was chosen to be 10^{-8} m^2/s. The reason for choosing larger value of troposphere spectral density compared to the airborne dataset is to allow larger tropospheric delay change because the helicopter dataset has sever and fast change of the height. The trajectory of the data is shown in Figure 5.22. The position of the GPS receiver was estimated using IGS final products at 15 and 5 minutes for orbit and clock, respectively. A base station near the site was used to perform GPS double difference positioning to determine the reference trajectory of the helicopter receiver. NovAtel GPS receivers were used at the base and rover stations. The DD solution epochs with accuracy better than 10 cm were used to produce the results. The quality of the DD solution is illustrated through the forward and backward solution separation and ambiguity fixing as shown in Figures 5.23, 5.24, and 5.25.
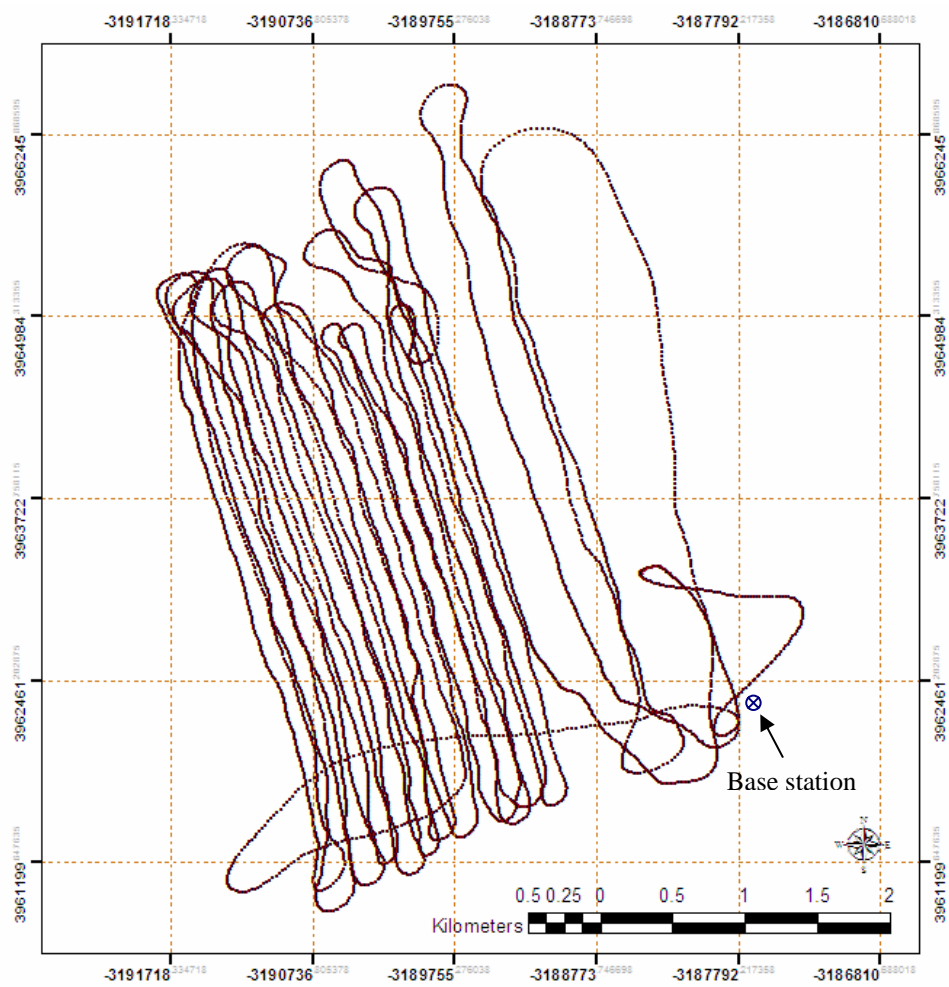
Figure 5.22 Helicopter trajectory
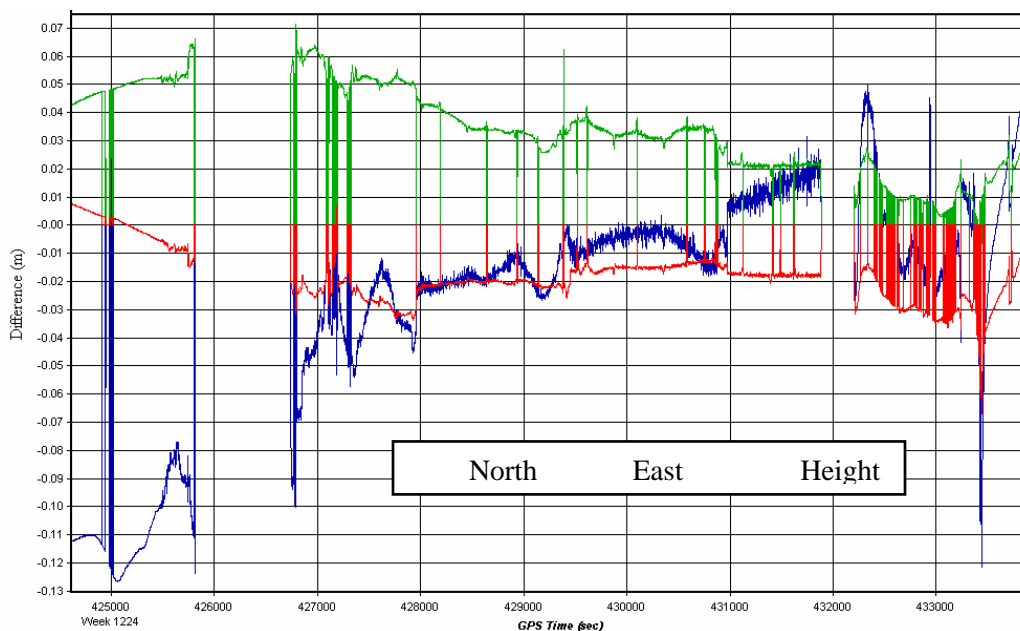
Figure 5.23 Difference between DD forward and reverse position solutions
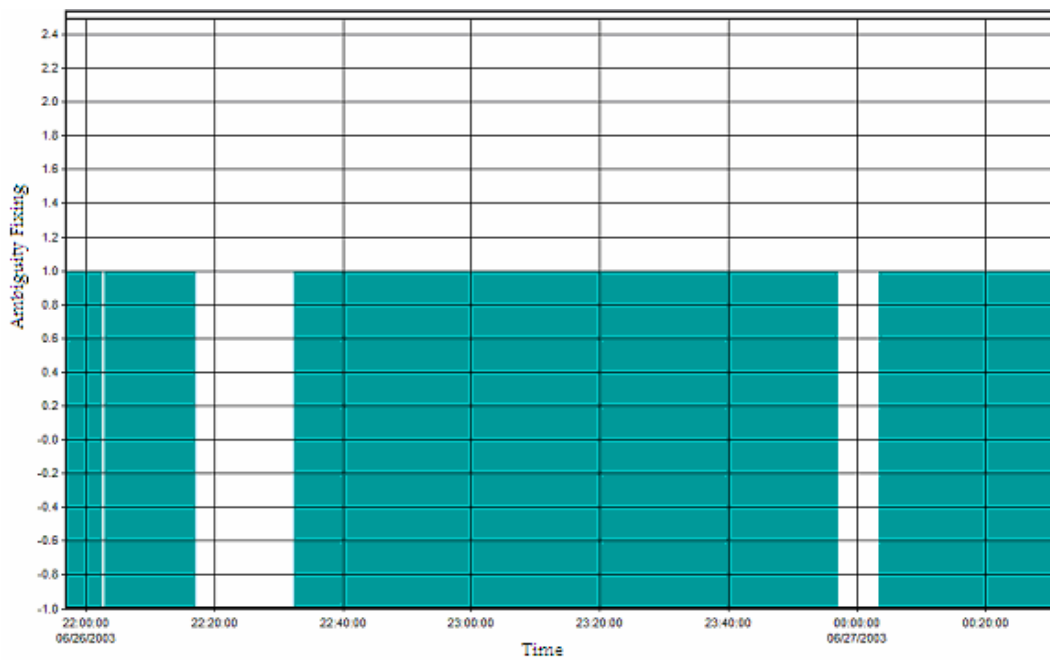
Figure 5.24 Ambiguity fixing for the forward solution
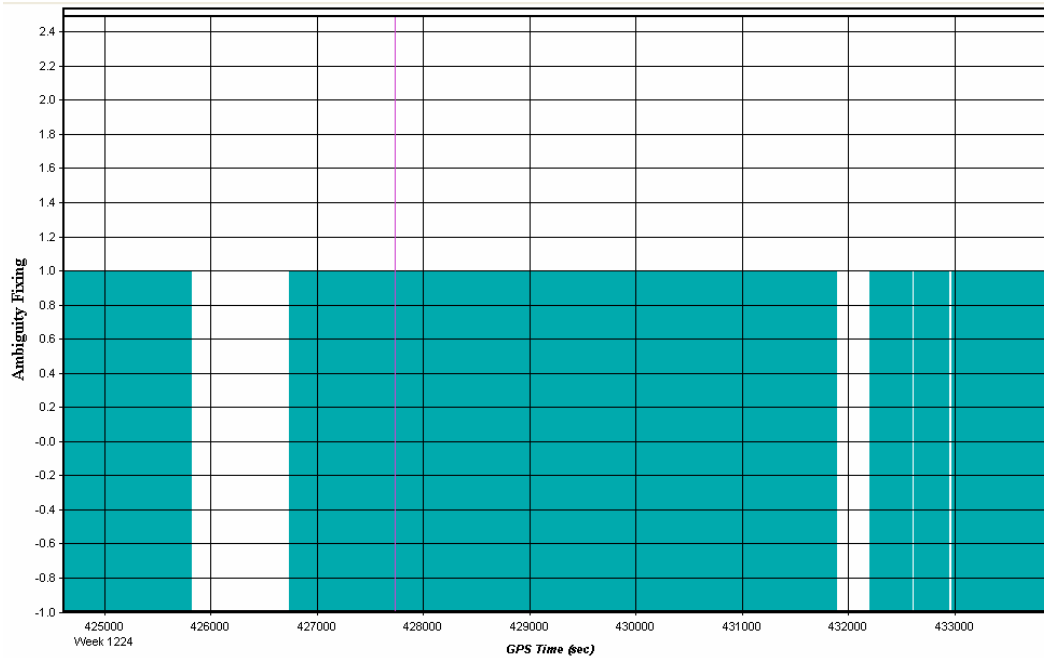
Figure 5.25 Ambiguity fixing for the reverse solution

Figure 5.26 depicts the offset between PPP and the reference trajectory. The PPP-DD's difference statistics show biases of 5 cm, 16 cm, and 12 cm in addition to standard deviations of 4, 16, and 17 cm for latitude, longitude, and height, respectively. One of the characteristic of this data set is a rapid change in height profile as shown in Figure 5.27. This variation could reach 600 meters within a few minutes. By studying Figure 5.27, it can be concluded that large positioning differences between the PPP and DD solutions occurred during the peak of the helicopter maneuverings. Also, these maneuverings includes large height change. The trajectory overlaid by the vector error is presented in Figure 5.28.
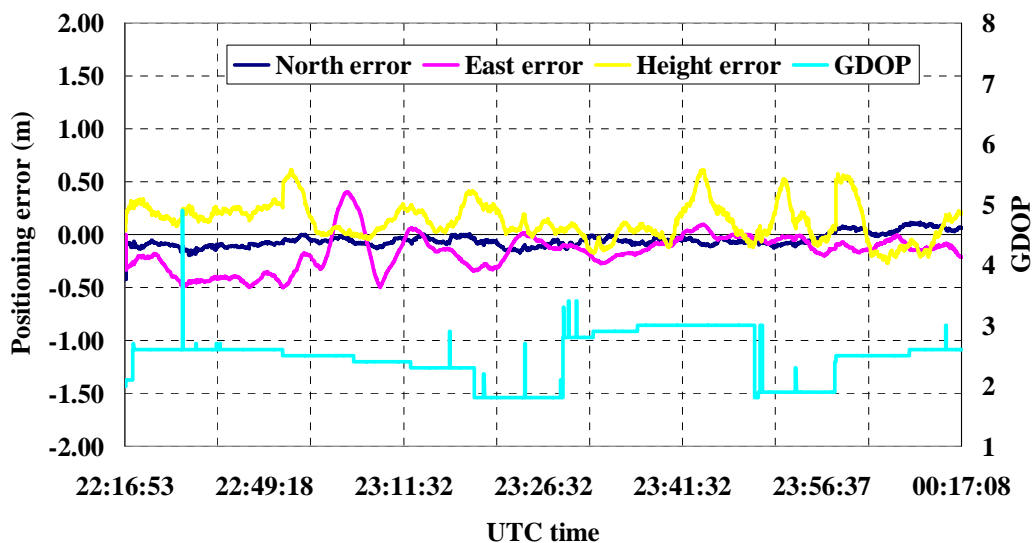
Figure 5.26 Helicopter dataset positioning accuracy with respect to DD solution
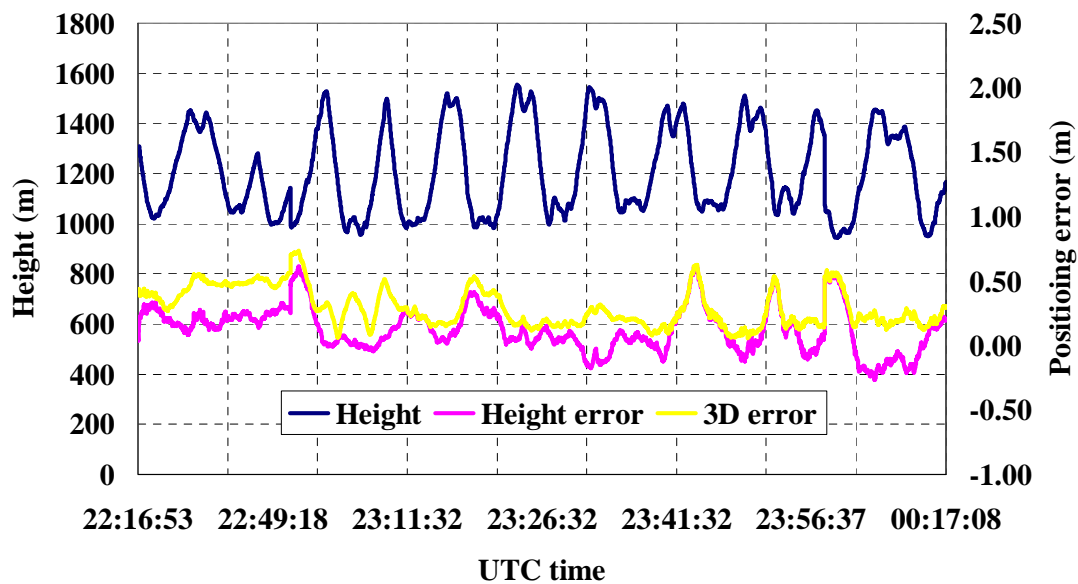
Figure 5.27 Height, height error, and 3D error for the helicopter dataset
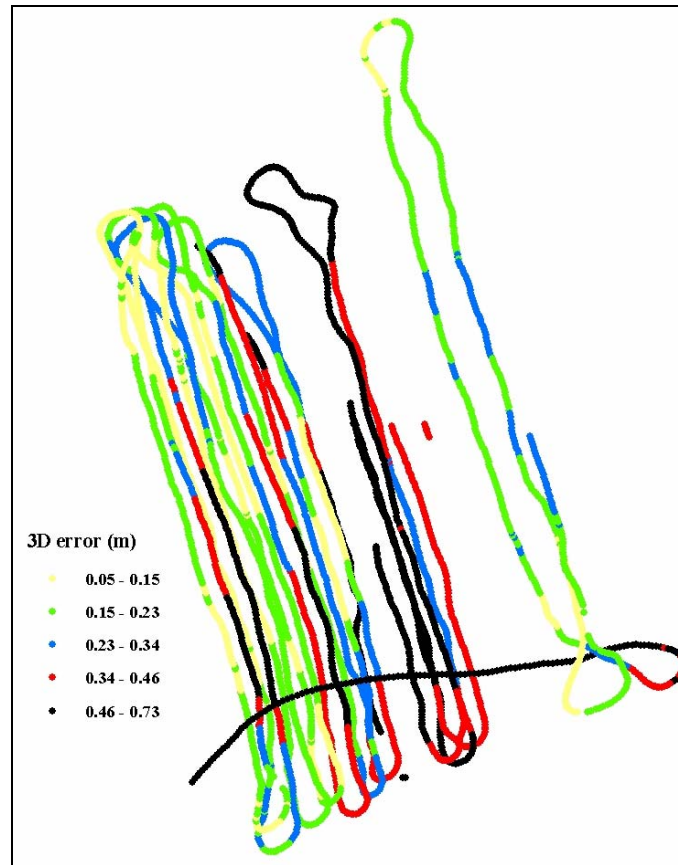
Figure 5.28 PPP-DD 3D offset of the helicopter trajectory

5.6 Summary

This chapter presented the numerical results from using PPP along with the final IGS orbit and clock products. Out of all the datasets shown in this chapter, the 5 minutes orbit and 5 minutes clock correction are used. Satellite clock corrections at 30 seconds were not available at the time of data collection. Based on the data used and considering the worst case, a bias of better than two decimeters can be achieved for the weakest

component, the height. Better accuracy could be obtained if clock corrections at short intervals were available as will be shown in Chapter 6. The kinematics results presented in this chapter are with respect to a GPS DD solution with precision of 10 cm. Processing GPS data using commercial DD software depends on the nature of the GPS data, processing parameters, and the baseline length. The baseline length for the land, marine, airborne, and helicopter datasets were about 12, 16, 30, 8 km, respectively. It is necessary to understand that part of the positioning errors (difference) can be attributed to the reference trajectory and that the accuracy of the DD solution is in fact a precision. Bruton et al. (2001) addresses the positioning accuracy and the variability of different DD commercial carrier phase differential GPS software. Based on the comparison of eight industrial carrier phase DGPS, Bruton et al. (2001) observed position differences that can reach meter level among these software. Another important issue, which will be tacked in the next chapter, is that PPP needs time to converge, especially when using clock data with large sampling intervals. This time of convergence is needed at the beginning of the solution or in the case that the solution is weakened due to geometry, undetected cycle slips, or signals loss. This can explain why long GPS datasets, the marine and the airborne datasets demonstrated high positioning accuracy compared to the shorter datasets.

CHAPTER 6

SOME ASPECTS OF PPP

This chapter addresses three aspects of PPP. The first is the ambiguity in PPP and the factors affecting it. The second is the convergence of PPP based on the analysis and investigation of several precise data products. The final aspect addresses the ambiguity equivalence of the two PPP models.

6.1 Ambiguity and Biases in PPP

GPS satellites move with a speed of about 4 km/s with respect to the GPS users on the earth's surface at a distance of about 20,000 km. Therefore, the geometry of the GPS constellation changes very slowly with respect to an observer occupying a point on the earth's surface. Consequently, GPS observations at short intervals do not add much to the GPS solution and act only as a kind of redundant or correlated measurement. This slow change poses a challenge for the estimation filters that use a sequential approach. To overcome this challenge in traditional double difference GPS processing (DD), a constraint is applied which strengths the solution instantaneously. The long established way in the case of DD is to constrain the ambiguities to integer values. However, this case is different from PPP as will be explained in detail in the following subsections.

6.1.1 Ambiguity and the Non-zero Initial Phase

The GPS receiver can observe the change in distance between a GPS satellite and a receiver after locking to the signals. Thus, at any given time, the distance to the GPS satellites consists of a number of complete cycles that appeared at the zero time (time of signals lock) of observations, the value of measurements at GPS carrier phase counter, and fractions of cycle at satellite and receiver antennas. These small fractions of cycles are known as non-zero initial phases and traditionally cancelled by double difference operations. As a result, the non-zero initial phases don not affect double difference carrier phase positioning techniques.

This section gives an explanation for the carrier phase non-zero initial phase. It might appear confusing that some GPS researchers doubt the existence of non-zero initial phase, while others think that this is an error related to the hardware (Gabor, 2000). Nevertheless, the non-zero initial phase is neither an observation error nor an equipment-related phenomena. It is a part of the basic model of carrier phase observations, simply because GPS signals reach receiver antennas at random phase, and this random phase is not necessarily nil. Propagating this signal back to the satellite antenna will produce a signal phase which does not have to be zero. Therefore, the carrier phase measurements will include a non-zero initial phase at both receiver and satellite. The value of this non-zero initial phase is constant for continuous receiver-satellite lock; however, because of the difference in the oscillators' quality at satellite and receiver, this non-zero initial phase might change with time. The value of this offset will be less than a cycle. This can

be explained mathematically using a simple model (Goad, 1997) as depicted by Equations 6.1, 6.2, and 6.3.

$$\Phi_R^S(t_r) = \Phi^S(t_r - r/c) - \Phi_R(t_r) \tag{6.1}$$

where

$\Phi_R^S(t_r)$ - satellite and receiver signal phase difference at receipt time

$\Phi^S(t_r - r/c)$ - satellite signal phase at emission time

$\Phi_R(t_r)$ - receiver signal phase at receipt time

r   - distance traveled by GPS signal

c   - speed of light

t_r - receipt time

Knowing that a perfect oscillator has the following relation,

$$\Phi(t + \Delta t) = \Phi(t) + f.\Delta t \tag{6.2}$$

where

Δt - time offset (time of propagation)

f - frequency

Equation 6.1 can be rewritten in the following form:

$$\Phi_R^S(t_r) = \Phi^S(t_r) - (f/c) \cdot r - \Phi_R(t_r) + N \tag{6.3}$$

where

N - carrier phase ambiguity

$\Phi^S(t_r)$ - satellite signal phase at receipt time

Consequently, the non-zero initial phase offset is independent from hardware or any system defect, and, because it is a part of the observation model, it will always exist in the un-differenced carrier phase equations.

6.1.2 The Observability of Non-zero Initial Phase Offset by Different GPS Receivers

The receiver non-zero initial phase will be different for each GPS receiver depending on the location and time (Abdel-salam, 2004). This difference is illustrated in Figure 6.1. The figure depicts a GPS satellite sending a signal at time t^s; different receivers acquire the signal at a sampling time t_r. Therefore, the distance between satellite and receiver at any epoch can be expressed in term of an initial phase offset at satellite and receiver at the first time of signals' lock, a number of complete cycles, and the value of carrier phase in the receiver counter. By using this concept, the non-zero initial phase can be considered unique for each satellite receiver pair or a constant value inherited from the first instant of receiver signal lock.
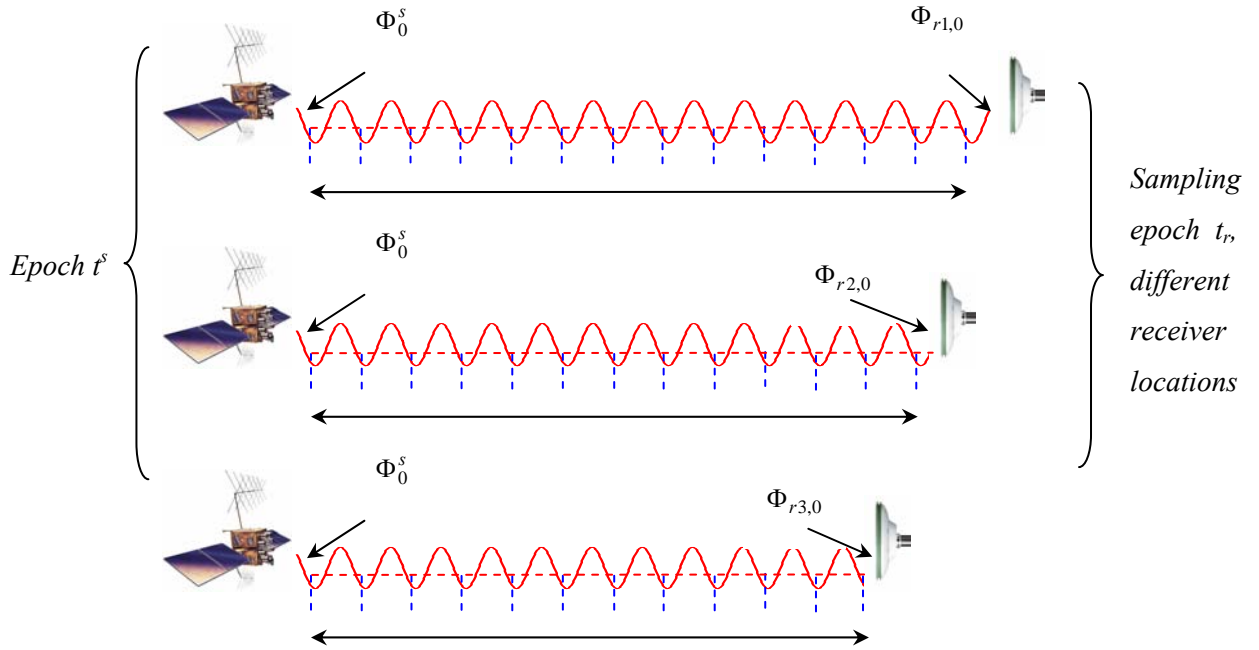
Figure 6.1 Initial phase offset at different receivers (*r1*, *r2*, and *r3*)

This explanation above can fit the case of standalone GPS receiver; hence, the non-zero initial phase can be understood as a constant part from the first instance of acquiring the signals. Any change of satellite and/or receiver position can be sensed by the receiver carrier phase counter as shown in Equation 6.4.

$$\Phi_R^S(t_{ri}) = \Phi^S(t_{r0}) - (f/c) \cdot r_i - \Phi_R(t_{r0}) + N_0 \qquad (6.4)$$

where

t_{ri} - time of an epoch at the GPS receiver

t_{r0} - receipt time (time of signals lock)

Another case, we can consider, is the non-zero initial phase as a variable quantity which changes every epoch. Consequently, the range distance will consist of two varying non-

zero initial phases, an ambiguity, and the value of the carrier phase in the receiver counter. However, the meaning of the non-zero initial phase will be different, and precise time synchronization for both satellite and receiver is necessary. This case fits the DD process, as every GPS receiver will observe the same non-zero initial phase. This can be expressed in Equation 6.5:

$$\Phi_R^S(t_{ri}) = \Phi^S(t_{ri}) - (f/c) \cdot r_i - \Phi_R(t_{ri}) + N_0 \tag{6.5}$$

6.1.3 Satellite Antenna Phase Offset

The GPS measurements refer to the electronic center of the antenna. As stated in Section 3.3.1, the precise orbit product refers to the center of mass, not the electronic center. Each GPS frequency has a different antenna phase center. The values of this offset are "somehow" agreed on for Blocks II, IIA, IIR for the purpose of IGS clock solution consistency (Zhu, 2003). An example of the discrepancy of these values is given in NGA (2004); Mader, (2001); Ray and Senior (2005); and Kouba and Heroux, (2000). In addition to the discrepancy, the antenna phase center has a variable component, which functions in the off-axis angle.

6.1.4 Inter-frequency Bias

The inter-frequency bias is a delay of L1 and L2 signals because of the different modulation of the L1 and L2 signals. The broadcast ephemeredes message provides values for this inter-frequency bias, while a more precise value can be obtained from JPL. This term must be applied to any autonomous GPS observation models except for the

ionosphere free combination (IDC, 2001). The day-to-day stability of the inter-frequency

bias is 0.1 ns (Hugentobler et al., 2000).

6.1.5 Precise Satellite Clock Correction

As shown by the GPS interface document and the IGS analysis centers, the satellite clock

correction corresponds to the ionosphere-free frequency. The reason is related to the

method by which the orbit and clock correction is estimated. For precise orbit and clock

determination, the orbit is first estimated through constructing a double difference

ionosphere-free combination, then the orbit is fixed and GPS clock corrections are

estimated by using zero differencing (Zumberge et al., 1995; NGA, 2004). Another

technique to estimate the orbit and clock is to use an ionosphere-free zero difference in

one step to estimate all parameters simultaneously. Both of these techniques are used by

IGS. The reason for using the ionosphere-free combination in both cases is that it has the

ability to mitigate the ionospheric delay and the uncertainty of the inter-frequency bias. It

is worth mentioning that each Analysis Center (AC) derives the clock corrections relative

to individual reference clock which leads to different results. The IGS combined these

clock corrections and aligned them with IGS time. Therefore, the uncertainty from the

satellite phase center and the non-zero initial phase will be absorbed by the clock and

ambiguities. It is evident, therefore, that only one clock correction will be available from

the estimation process at ionosphere-free frequency and this correction should fit the GPS

pseudocode and carrier phase observations on the GPS L1 and L2 frequencies.

Consequently, the precise clock cannot be considered as an inherent representative of the non-zero initial phase for the L1 and L2 carrier phases.

6.1.6 Ambiguity Resolution in PPP

One of the limitations of precise point positioning is that long time of convergence is necessary to achieve the targeted positioning accuracy. Ambiguity resolution is the fastest way to achieve fast convergence. In this section, we will discuss the possible models of PPP and its ability to perform any ambiguity resolution, but, first, the concept of constraint optimization is briefly highlighted.

In double difference GPS processing, the estimated parameters can be classified into two different sets. The first is the baseline parameters, and the second is the ambiguities. The second can be characterized with its integer nature. This integer nature is met in the case of double difference when certain conditions are satisfied, such as the absence of multipath and negligibility of atmospheric conditions difference for both the base and rover stations. Mathematically, the constrained estimation process can be expressed as given in Equation 6.6.

$$\min f(x_1, x_2) | x_2 \in N \tag{6.6}$$

where

x_1 - the baseline parameters

x_2 - the ambiguity parameters

N   - the integer numbers domain

The applicability of the integer condition to the ambiguity parameters will strengthen the solution only if the vector x_2 belongs to the integer numbers. This holds true for the case of double difference GPS processing but not for the case of un-differenced observation because the ambiguities are not integers as will be shown in the next two subsections.

Ionosphere-free Code and Carrier Phase Combination

The model as previously shown in Section 4.1 has two interesting characteristics. It can mitigate the errors caused by the ionosphere and the uncertainty resulting from the inter-frequency bias. However, the ambiguities on the two frequencies are estimated as a lump term. Thus, the lump sum ambiguities become real number and a constraint such as ambiguities are integers is void. Therefore, the float nature of the ambiguities to be estimated in PPP prevents the applicability of ambiguity resolution.

The UofC Model

The UofC model, shown in Equations 4.10 to 4.12, has the capability to estimate the ambiguities on L1 and L2 separately. However, the two unaccounted quantities for non-zero initial phase and inter-frequency difference for pseudocode and carrier phase observations do not cancel in general. These errors will be observed into the ambiguity estimate making the ambiguity parameter no longer integers. Moreover, one value for the satellite antenna phase center is adopted by IGS. This contradicts the fact that every satellite has different phase center offsets as mentioned in Section 3.3.1. Consequently,

these biases will prevent the applicability of ambiguity resolution. Both PPP models in the best case will not be able to resolve the ambiguity.

6.2 PPP Convergence Analysis

In this section, the convergence of PPP solution is analyzed by addressing three aspects. The first is the effect of observations and precise data intervals on convergence; the second aspect investigates the effect of stopping estimating the accurate ambiguities on convergence time. The third aspect tackles the convergence behavior through investigating the effect of tropospheric delay estimation and modeling on the convergence time.

6.2.1 Effect of Observations and Satellite Sampling Intervals

To study the first aspect, the effects of observation and precise data intervals on convergence, two types of GPS datasets are used. The first data set is from twelve IGS stations distributed around the world as shown in Figure 6.2.
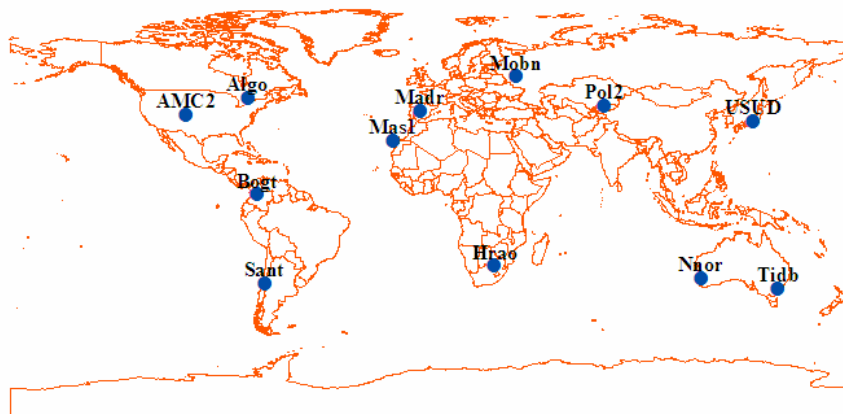
Figure 6.2 Map of the IGS stations

These IGS datasets are high quality GPS observations with intervals of 30 seconds and collected on June 1st, 2004. The second set of data consists of 6 days with a data rate of 1 Hz collected in Calgary on May 10 through 15, 2004. The receiver antenna phase center was considered for the two datasets. The PPP static estimation scheme that used in section 5.1 is adopted because the GPS datasets are static. For precise data, the available IGS precise products are shown in Table 6.1. The use of this precise data will be divided into three cases according to the satellite clock intervals. The reason for the existence of several clock-sampling intervals is the demand of GPS community for higher satellite clock rate. Satellite clock corrections at sampling intervals of 15 and 5 minutes are obtained from the IGS orbit and clock estimation process, while the satellite clock corrections at sampling rate of 30 seconds are obtained based on "an efficient phase-consistent interpolation of 5-minute precise clock results using phase time differences" (IGSmail #4913, 2004).

Table 6.1 Types of precise data

Type of precise data		Accuracy	Sample interval	latency
Case-1 , Final	Orbit	<5 cm	15 min	~13 Days
	Clock	< 0.1 ns	30 sec	
Case-2, Final	Orbit	< 5 cm	15 min	~13 days
	Clock	< 0.1 ns	5 min	
Case-3, Final	Orbit	< 5 cm	15 min	~13days
	Clock	< 0.1 ns	15min	

6.2.1.1 IGS Stations: Case-1

Figures 6.3 through 6.5 depict the convergence behavior of PPP for latitude, longitude

and height when using the IGS orbit and clock at sampling intervals of 15 minutes and 30

second, respectively.

Figure 6.3 IGS Case-1: Latitude error repeatability
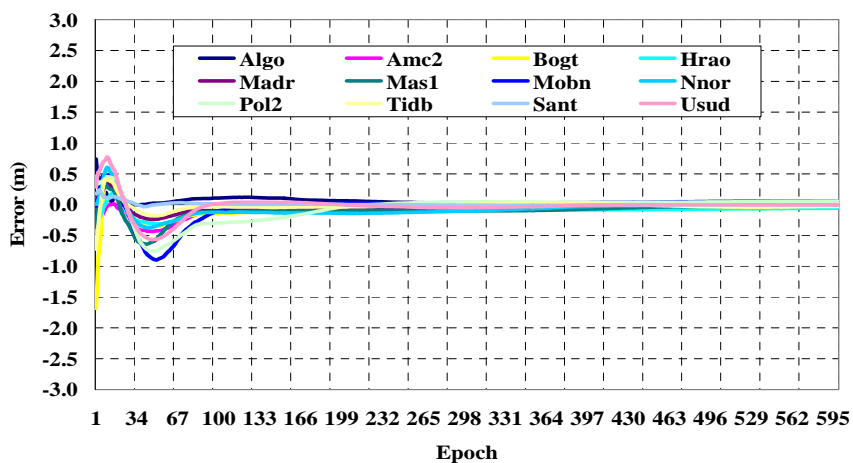
Figure 6.4 IGS Case-1: Longitude error repeatability
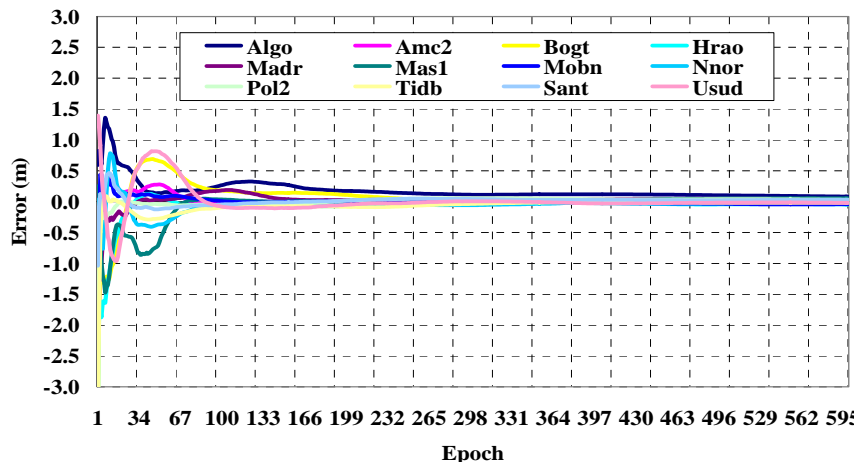
Figure 6.5 IGS Case-1: Height error repeatability

The time required for each coordinate component to converge to better than 50, 30, 20, and 10 cm is given in details in Table 6.2. The calculation of the convergence time is defined in a way that no single epoch of positioning errors exceeds the threshold. Accordingly, when interpreting these results, it should be understood that the convergence time can be less than the tabulated values because the positional errors can oscillate around the threshold with a very small amplitude. In Table 6.2, the values in the brackets are the average with the extreme values excluded.

Table 6.2 IGS Convergence time statistics (Case-1, units: epochs)

	Algo	AMC2	Bogt	Hrao	Madr	Mas1	Mobn	Nnor	Pol2	Sant	Tidb	Usud
Latitude <50cm	12	1	3	1	7	1	1	1	3	2	1	4
	Average:3 epochs											
Latitude <30cm	18	15	12	1	13	11	67	8	4	5	1	18
	Average:14 epochs											
Latitude <20cm	30	56	19	3	18	15	73	10	4	46	7	65
	Average:29 epochs											
Latitude <10cm	36	68	25	4	28	26	84	17	5	74	20	79
	Average:39 epochs											
Longitude <50cm	4	1	6	1	1	54	71	15	71	4	1	58
	Average:24 epochs											
Longitude <30cm	7	68	62	58	15	64	81	59	100	18	1	70
	Average:50 epochs											
Longitude <20cm	11	79	75	73	60	71	90	74	157	20	6	75
	Average:66 (54) epochs											
Longitude <10cm	156	109	166	158	82	338	102	311	184	67	21	82
	Average:148 (113) epochs											
Height <50cm	29	6	64	19	7	55	3	16	4	4	3	67
	Average:23 epochs											
Height <30cm	138	17	77	21	12	59	12	60	5	5	15	73
	Average:41 (32) epochs											
Height <20cm	177	60	92	25	25	62	15	68	11	66	19	77
	Average:58 (47)epochs											
Height <10cm	521	67	206	50	132	66	46	81	16	99	62	162
	Average:119 (90) epochs											

( ) indicates averaging excluding the red values

6.2.1.2 IGS Stations: Case-2

Figures 6.6 to 6.8 show the convergence behavior when using the second case of precise data (Case-2). The figures show an increase in the convergence time compared to Case 1. Table 6.3 summarizes these figures.

Figure 6.6 IGS Case-2: Latitude error repeatability

Figure 6.7 IGS Case-2: Longitude error repeatability

Figure 6.8 IGS Case-2: Height Latitude error repeatability

Table 6.3 IGS Convergence time statistics (Case-2, units: epochs)

	Algo	AMC2	Bogt	Hrao	Madr	Mas1	Mobn	Nnor	Pol2	Sant	Tidb	Usud
Latitude <50cm	14	10	9	17	9	14	43	7	11	20	7	60
	18 epochs											
Latitude <30cm	18	30	9	29	31	20	55	16	23	23	11	67
	28 epochs											
Latitude <20cm	29	33	12	33	33	21	57	31	40	27	31	79
	36 epochs											
Latitude <10cm	36	81	18	49	52	44	58	34	44	64	34	148
	56 epochs											
Longitude <50cm	23	63	26	23	12	49	54	22	78	54	21	65
	41 epochs											
Longitude <30cm	24	65	44	25	13	61	57	32	92	77	52	75
	51 epochs											
Longitude <20cm	53	105	76	31	53	64	57	73	94	157	56	82
	75 epochs											
Longitude <10cm	220	134	210	135	64	99	102	235	192	306	60	155
	160 (118) epochs											
Height <50cm	118	50	26	30	35	59	32	57	33	39	22	68
	47 (45) epochs											
Height <30cm	186	53	27	49	54	62	33	65	34	65	32	143
	67 (57) epochs											
Height <20cm	227	71	33	53	133	71	72	68	35	85	41	182
	105 (81) epochs											
Height <10cm	623	142	227	867	146	181	185	88	161	124	52	187
	257 (160) epochs											

( ) indicates averaging excluding the red values

6.2.1.3 IGS Stations: Case-3

Figures 6.9 to 6.11 illustrate the convergence behavior using the third case of precise data, Case-3. There are an increase in the convergence time compared to Case-1 and Case-2. The convergence behavior is summarized is given in Table 6.4
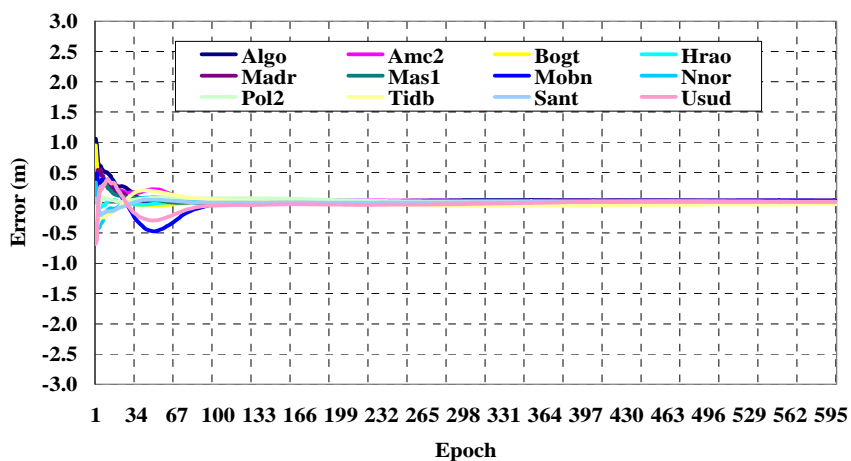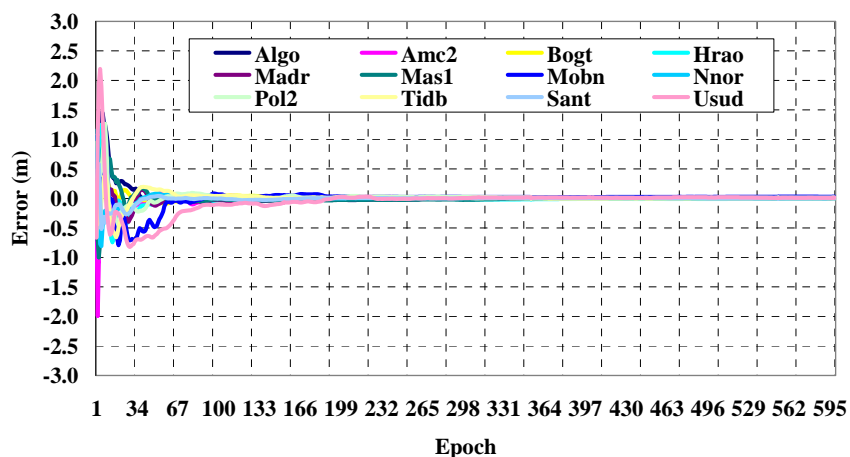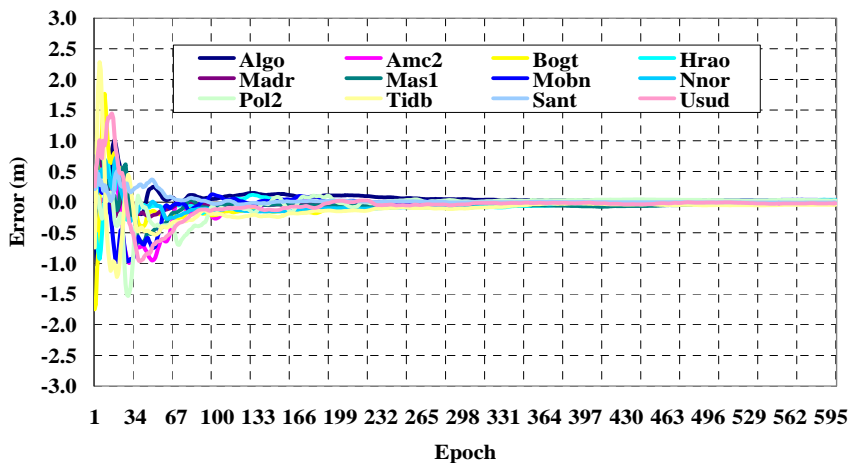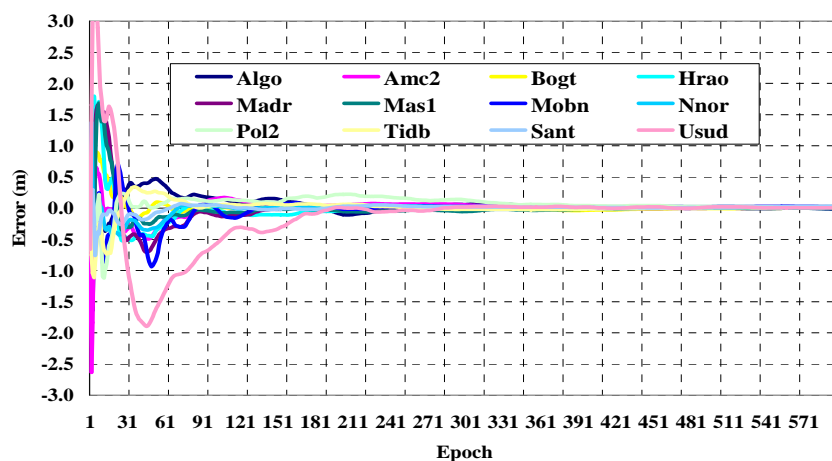

Figure 6.9 IGS Case-3: Latitude error repeatability
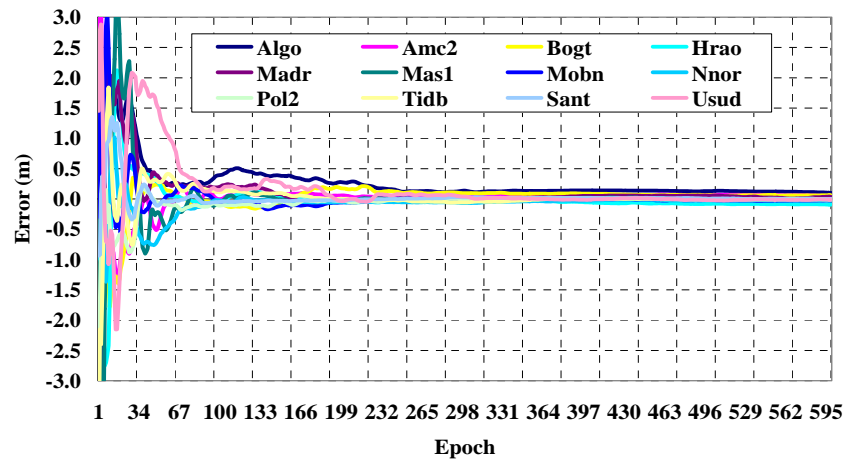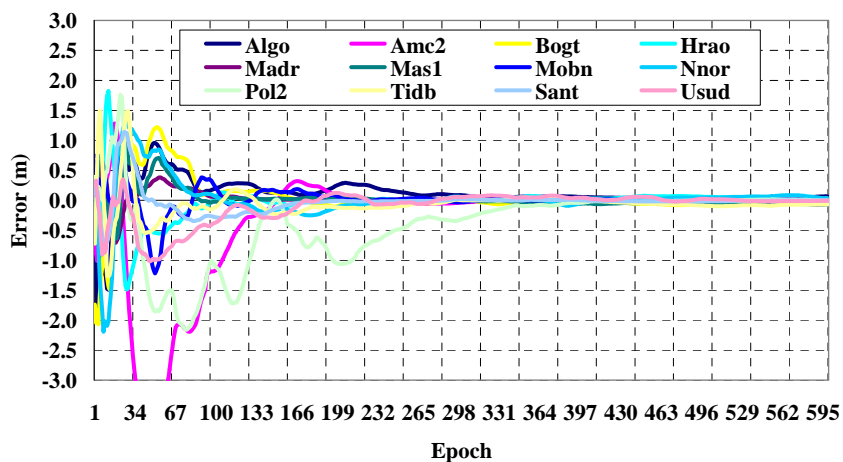

Figure 6.10 IGS Case-3: Longitude error repeatability
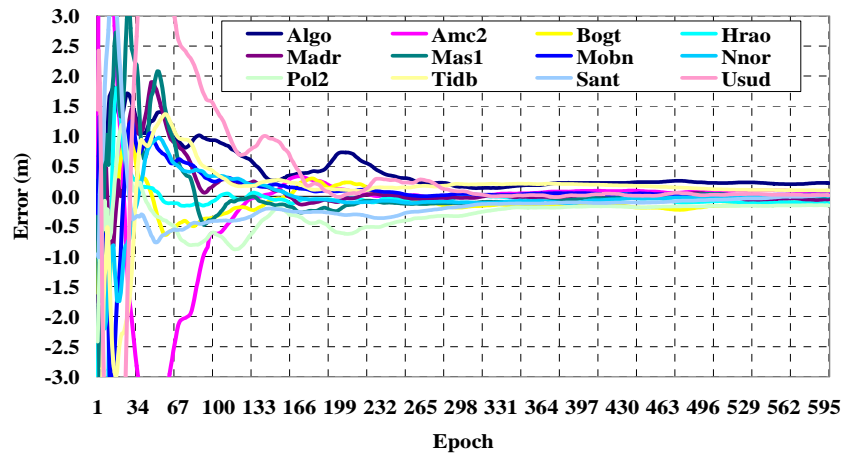
Figure 6.11 IGS Case-3: Height error repeatability

Table 6.4 IGS Convergence time statistics (Case-3, units: epochs)

	Algo	AMC2	Bogt	Hrao	Madr	Mas1	Mobn	Nnor	Pol2	Sant	Tidb	Usud
Latitude <50cm	5	10	16	37	55	21	59	4	19	20	8	107
	31											
Latitude <30cm	65	58	19	59	75	35	78	57	21	42	10	155
	57											
Latitude <20cm	90	62	26	68	81	54	81	62	217	64	30	164
	84 (71) epochs											
Latitude <10cm	213	129	44	156	131	80	125	67	316	79	53	173
	131(104) epochs											
Longitude <50cm	76	118	81	61	23	61	59	65	247	49	37	85
	80 (65) epochs											
Longitude <30cm	83	172	84	74	62	67	98	71	304	64	90	106
	106 (89) epochs											
Longitude <20cm	233	118	86	78	73	80	101	189	321	170	143	160
	142 (120) epochs											
Longitude <10cm	286	198	200	110	93	84	182	203	342	250	156	205
	192 (168) epochs											
Height <50cm	227	107	67	27	80	70	81	69	235	89	77	164
	108 (84) epochs											
Height <30cm	256	174	179	31	83	101	112	110	306	106	251	170
	157 (118) epochs											
Height <20cm	612	191	489	37	134	202	126	128	1087	397	286	282
	331 (262) epochs											
Height <10cm	768	561	572	1008	181	314	228	396	2635	599	459	292
	668 (400) epochs											

( ) indicates averaging excluding the red values

Examining the results of the three cases of precise clock corrections, it can be concluded that the satellite clock correction interval is a major factor that affects the convergence behavior. Accordingly, the satellite clock correction at sampling intervals of 30 seconds is recommended compared to other sampling intervals, 5 and 15 minutes. An interesting observation can be also drawn when comparing the results of Algo and Pol2 IGS stations to the other used IGS stations as shown in Table 6.4. These stations showed worse convergence degradation when using clock corrections at sampling intervals of 15 minutes compared to the other stations. This could be attributed to the irregularities of the clock corrections of some of the GPS satellites that are observed at this station. Because of the large distances among the used IGS station, these irregularities may not affect the other IGS station convergence results because different satellites are observed at different IGS stations. These irregularities of satellite clock corrections when occur between the clock sampling points become hard to be interpolated. More general factors that affect convergence can be pseudocode quality and satellite geometry. The following section will study the convergence behavior using GPS datasets with a sampling rate of 1Hz.

6.2.1.4 Calgary Datasets: Case-1:

In this section, the convergence behavior of 1 second datasets is investigated. For this purpose, a GPS station was installed at the University of Calgary for six days. The data of this station has a sampling interval of 1 second and an elevation cut off angle of 10 degrees. The estimation scheme of Section 5.1 was also used to process the Calgary datasets. The same three sets of precise data that are shown in Table 6.1 used in this investigation. Figures 6.12 to 6.14 show the convergence behavior for these 1 second GPS datasets.

Figure 6.12 Calgary Case-1: Latitude error repeatability
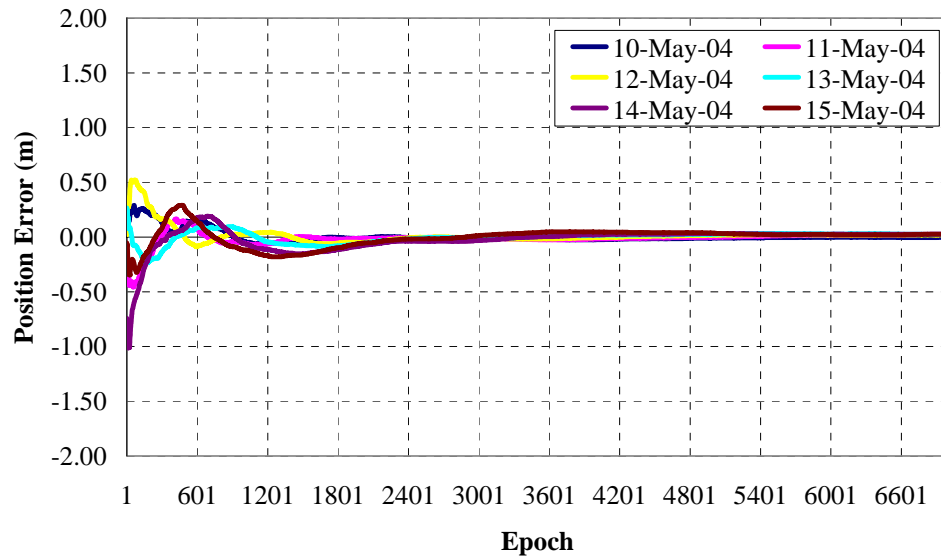
Figure 6.13 Calgary Case-1: Longitude error repeatability

Figure 6.14 Calgary Case-1: Height error repeatability

It can be concluded from the last three figures that a large number of epochs are needed compared to the case of IGS datasets that have a sampling rate of 30 second intervals, but a smaller convergence time is needed. The summary of the convergence behavior is shown in Table 6.5.

Table 6.5 Calgary Convergence time statistics (Case-1, units: epochs)

	10-May	11-May	12-May	13-May	14-May	15-May
Latitude <50cm	144	2	118	5	160	58
	81 epochs					
Latitude <30cm	200	67	278	246	346	192
	222 epochs					
Latitude <20cm	380	73	595	382	462	266
	360 (313) epochs					
Latitude <10cm	568	427	736	485	668	1022
	651(577) epochs					
Longitude <50cm	2	2	86	2	94	2
	31 epochs					
Longitude <30cm	4	129	178	2	145	98
	93 epochs					
Longitude <20cm	247	174	237	229	184	546
	270 (214) epochs					
Longitude <10cm	733	579	402	331	1885	1788
	953 (511) epochs					
Height <50cm	220	73	95	96	113	73
	112 epochs					
Height <30cm	357	228	389	117	1535	1512
	690 (273) epochs					
Height <20cm	474	285	587	1779	1922	1885
	1155 (449) epochs					
Height <10cm	570	571	2139	2256	4987	4941
	2577 (1384) epochs					

( ) indicates averaging excluding the red values

6.2.1.5 Calgary Datasets: Case-2

Using the second set of precise data, Case-2, the convergence of the 1 second GPS data
was investigated. The convergence behavior is illustrated in Figures 6.15 to 6.17.
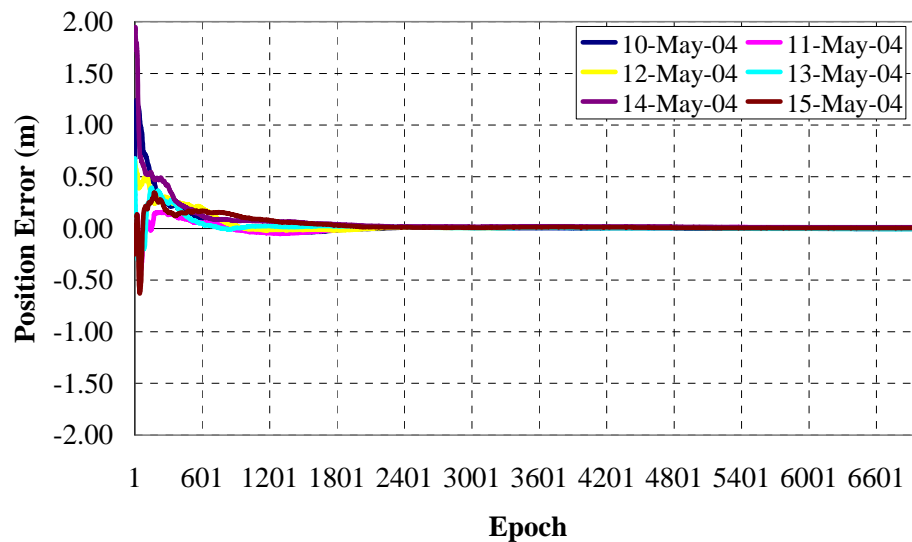

Figure 6.15 Calgary Case-2: Latitude error repeatability

Figure 6.16 Calgary Case-2: Longitude error repeatability

Figure 6.17 Calgary Case-2: Height error repeatability

Table 6.6 IGS Convergence time statistics (Case-2, units: epochs)

	10-May	11-May	12-May	13-May	14-May	15-May
Latitude <50cm	182	455	880	276	795	606
	532(378) epochs					
Latitude <30cm	482	497	1123	301	1485	1502
	898(427) epochs					
Latitude <20cm	1120	515	1438	961	1600	1580
	1202(866) epochs					
Latitude <10cm	1309	1643	1825	2232	1674	1665
	1725(1542) epochs					
Longitude <50cm	136	125	704	544	30	680
	370(208) epochs					
Longitude <30cm	169	1821	924	765	1575	1039
	1049(317) epochs					
Longitude <20cm	381	1979	1004	849	2249	1191
	1275(857) epochs					
Longitude <10cm	1287	2583	2998	2500	3404	1306
	2346(1919) epochs					
Height <50cm	621	586	651	498	783	1512
	775(628) epochs					
Height <30cm	1834	813	692	1253	976	2216
	1297(934) epochs					
Height <20cm	1991	849	1481	1808	1855	2466
	1742(1597) epochs					
Height <10cm	2218	2245	1740	4890	10249	4440
	4297(2067) epochs					

6.2.1.6 Calgary Datasets: Case-3

This section discusses the results using the third set of precise data, Case-3. Figures 6.18 to 6.20 illustrate the convergence behavior. The summary of the convergence of these datasets are shown in Table 6.7.
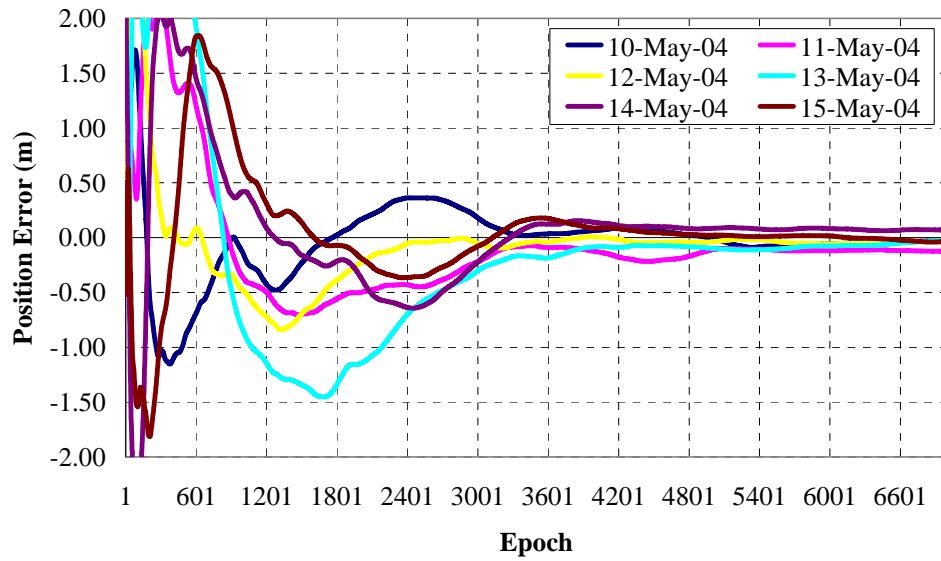
Figure 6.18 Calgary Case-3: Latitude error repeatability

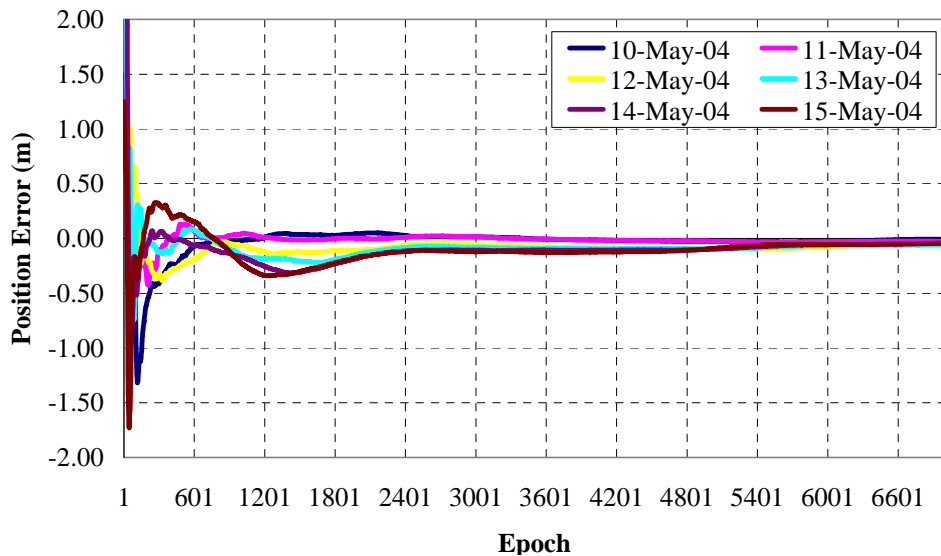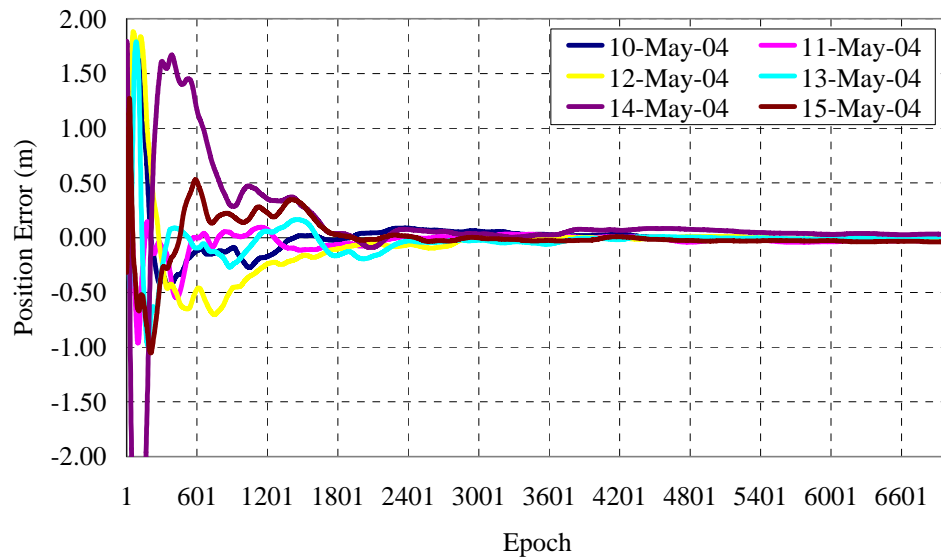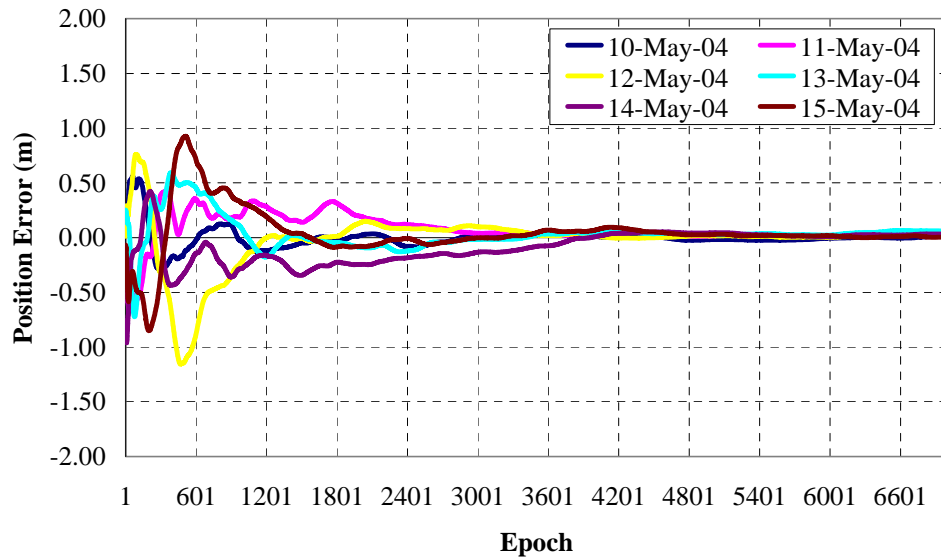

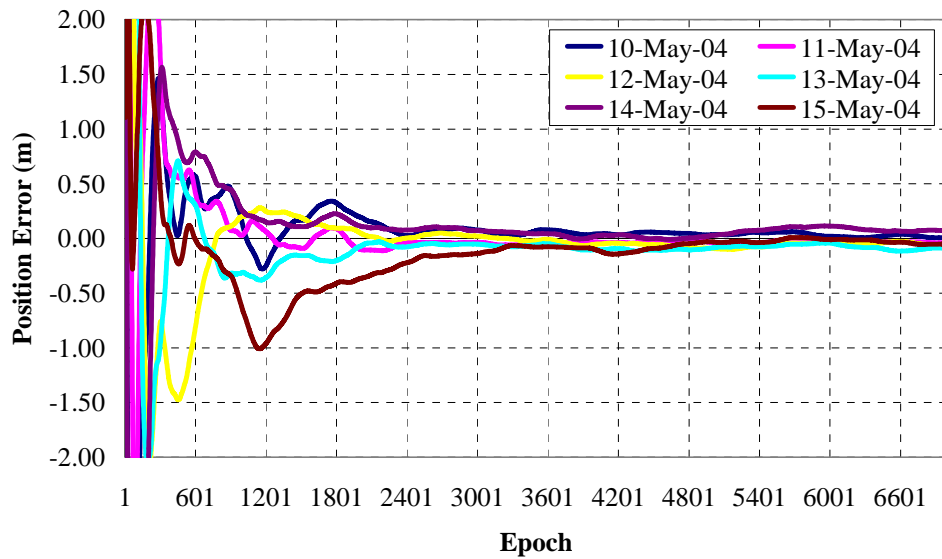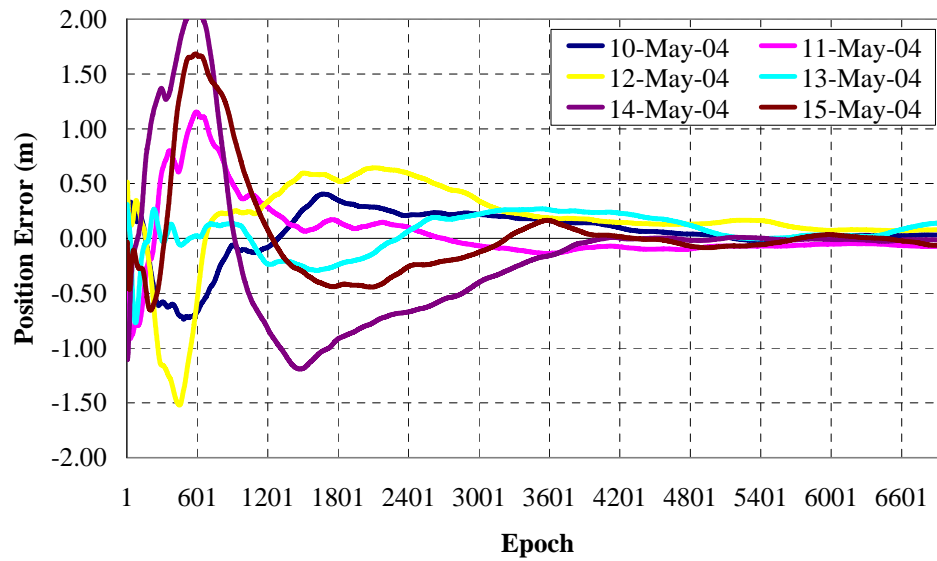Figure 6.19 Calgary Case-3: Longitude error repeatability
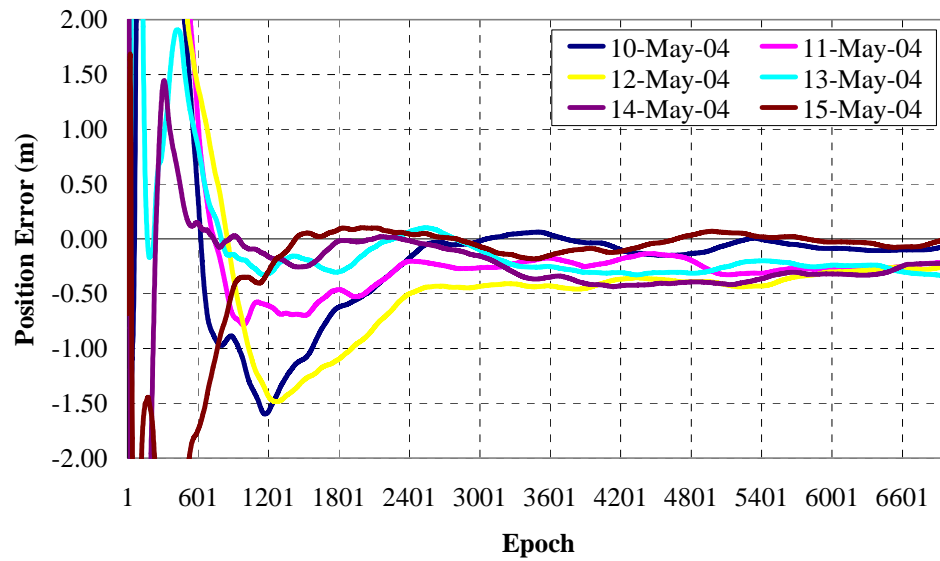
Figure 6.20 Calgary Case-3: Height error repeatability

Table 6.7 Calgary Convergence time statistics (Case-3, units: epochs)

	10-May	11-May	12-May	13-May	14-May	15-May
Latitude <50cm	700	2003	1689	2664	2692	1115
	1850 epochs					
Latitude <30cm	2799	2851	1910	3006	2916	2640
	2687(2624) epochs					
Latitude <20cm	2977	4635	2053	3232	3024	2818
	3123 epochs					
Latitude <10cm	3132	8405	2312	5620	4588	3913
	4662(3119) epochs					
Longitude <50cm	691	902	2624	104	2862	1036
	1370(684) epochs					
Longitude <30cm	1958	1183	3083	117	3228	2342
	1985(1400) epochs					
Longitude <20cm	3235	1312	3484	4384	3446	2748
	3101(2848) epochs					
Longitude <10cm	4190	4767	5701	4862	3743	3772
	4506 (4267) epochs					
Height <50cm	621	2021	2405	659	448	889
	1174 (655) epochs					
Height <30cm	2264	11010	6084	7746	6486	1201
	5798 (4009) epochs					
Height <20cm	2378	13314	8615	9390	8087	1256
	7173 (3065) epochs					
Height <10cm	4983	16413	9443	19494	10249	4263
	10807 (6229) epochs					

One of the observations for the Calgary datasets convergence results is the short time of convergence needed compared to IGS GPS datasets. This difference in convergence time is attributed to the small sampling intervals of the Calgary datasets. Also, the convergence time varies form one day to another and this variation could be attributed to the difference in precise data for each day and the exclusion of one satellite during some days (May 12 and 14 in Table 6.5). The first two days of the data achieved height positioning accuracy better than 10 cm in less than 10 minutes.

6.2.1.7 Convergence Summary

The last six subsections gave a detailed description of the convergence behavior. The following paragraph presents an overall summary and analysis. First, it is evident that the effect of small observation and precise satellite clock correction intervals on the convergence is large. The effect of observation intervals can be observed by comparing the results obtained from IGS and Calgary datasets when the same precise data is used. It is also worth mentioning that the effect of satellite clock correction is large. This can be observed from the convergence time needed when using different types of precise data. The available 30 second corrections are definitely the best. In PPP, the orbit and satellite clock corrections are interpolated at the corresponding observation time. The error from orbit interpolation is negligible because the orbit has a very smoothed behavior. Conversely, clock interpolation is critical because the satellite clock corrections lack any smooth trend. Accordingly, there is a strong demand for high rate clock correction in all

space state based systems. In contrast to orbit interpolation, satellite clock corrections interpolation may be not accurate because of the high level of irregularity. This irregularity cannot be attributed to the defect of the interpolation strategy but to the nature of clock corrections. A study of broadcast and precise orbit and satellite clock are presented in (Roulston et al., 2000; Abdel-salam et al., 2002). An example for the nature of these irregularities is given in Figure 6.21. The figure illustrates the satellite clock corrections at sampling rate of 5 and 15 minutes. Only clock corrections at the mentioned sampling intervals can be compared because they have the same reference time. The satellite clock corrections at sampling intervals of 30 seconds have a different time reference.
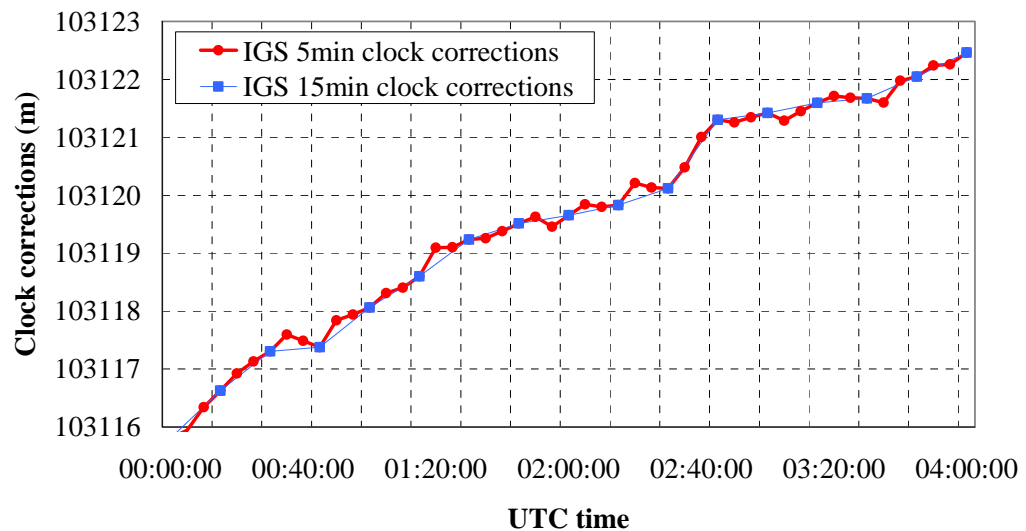
Figure 6.21 Irregularity of satellite clock corrections

6.2.2 Effect of Tropospheric Delay Modeling Instead of Estimation on the Convergence

One of the characteristics of standalone positioning is the existence of a strong correlation between height and tropospheric delay components. This correlation can be seen in Figure 6.22 for the first four IGS stations that have been used in the previous section.
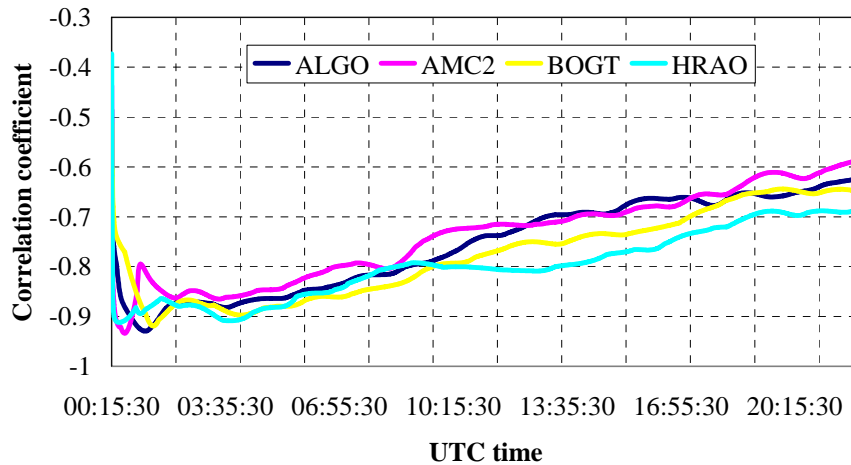
Figure 6.22 Height and tropospheric delay correlation coefficient resulting from the IGS static data

Accordingly, this section describes an investigation of the effect of using surface meteorological parameters to model the troposphere for the first 10 minutes of the solution. It is assumed that within these ten minutes the surface meteorological parameters will not change. This assumption will give users some flexibility and will help in avoiding using any expensive surface meteorological instruments; instead, these parameters can be retrieved for free from many meteorological websites. The Hopfield model and Niell mapping function is used to model the tropospheric delay (Misra and

Enge, 2001; Leick, 2004). The models of the Hopfield model and Neill mapping function are presented previously in Section 3.2.2. The details of troposphere estimation using PPP will be discussed in Chapter 7.

The data used for this section are 1 second interval GPS datasets collected in August 10 to 15, 2004. Precise orbit and clock corrections at sampling intervals of 15 minutes and 30 seconds were used. An elevation cut off angle of 10 degrees was used. A static processing scheme similar to the one given in section 5.1 was used. Figures 6.23 through 6.28 depict the results of this investigation. Surface meteorological parameters are necessary for troposphere modeling and were obtained using a *MET3A* sensor.
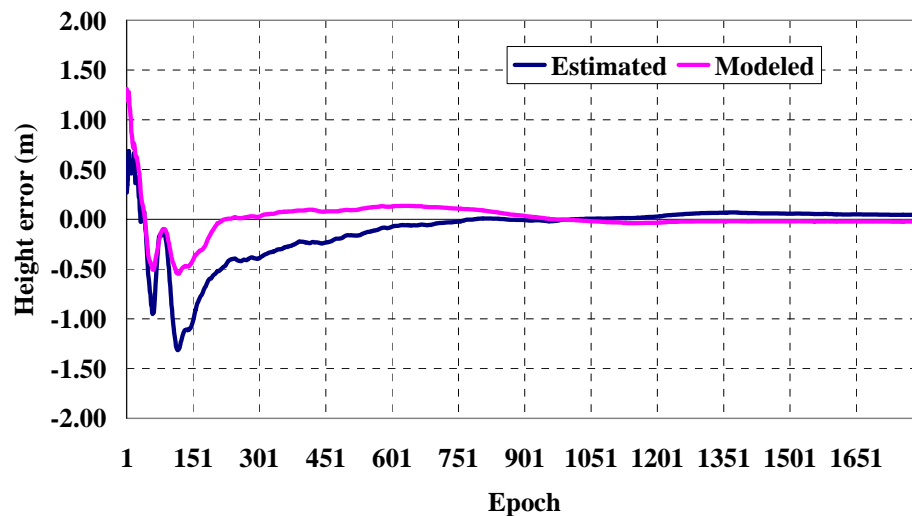
Figure 6.23 Height convergence for May 10 dataset
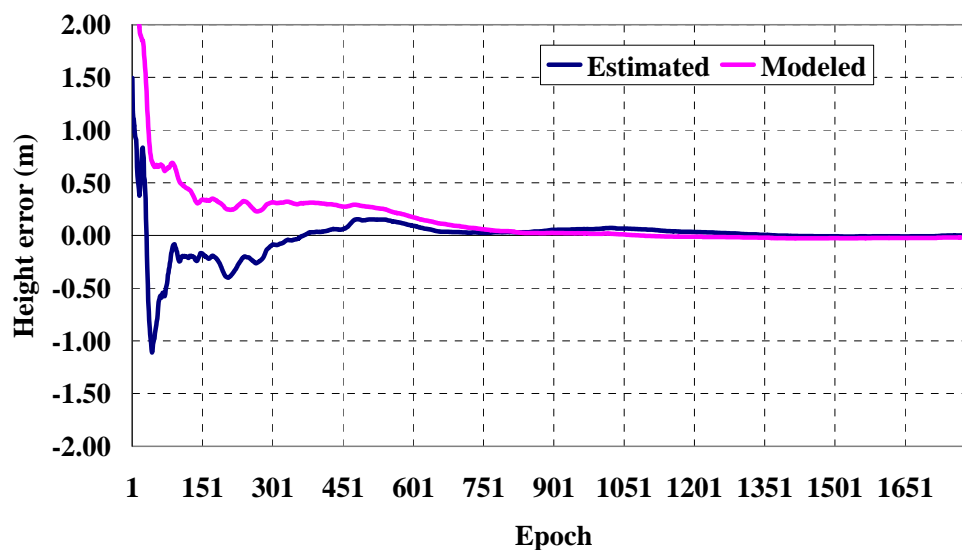
Figure 6.24 Height convergence for May 11 dataset
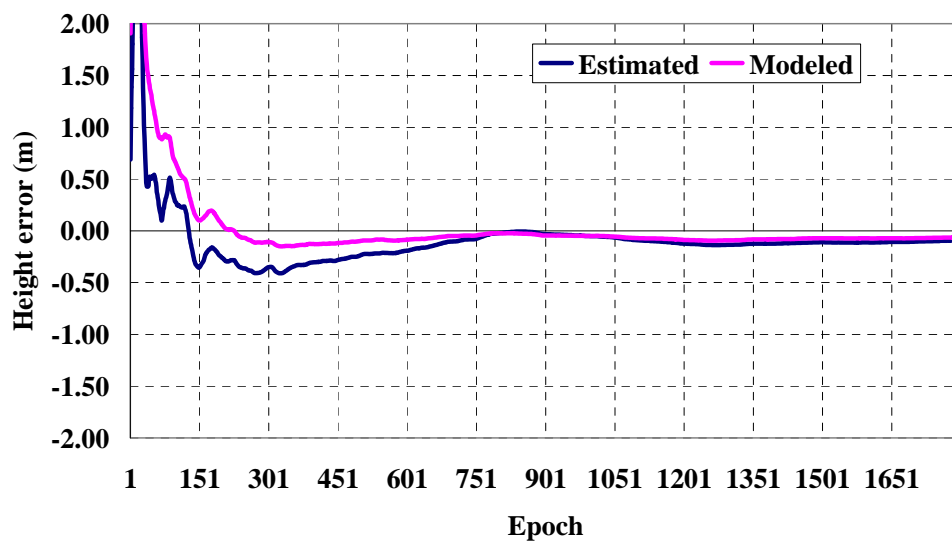
Figure 6.25 Height convergence for May 12 dataset
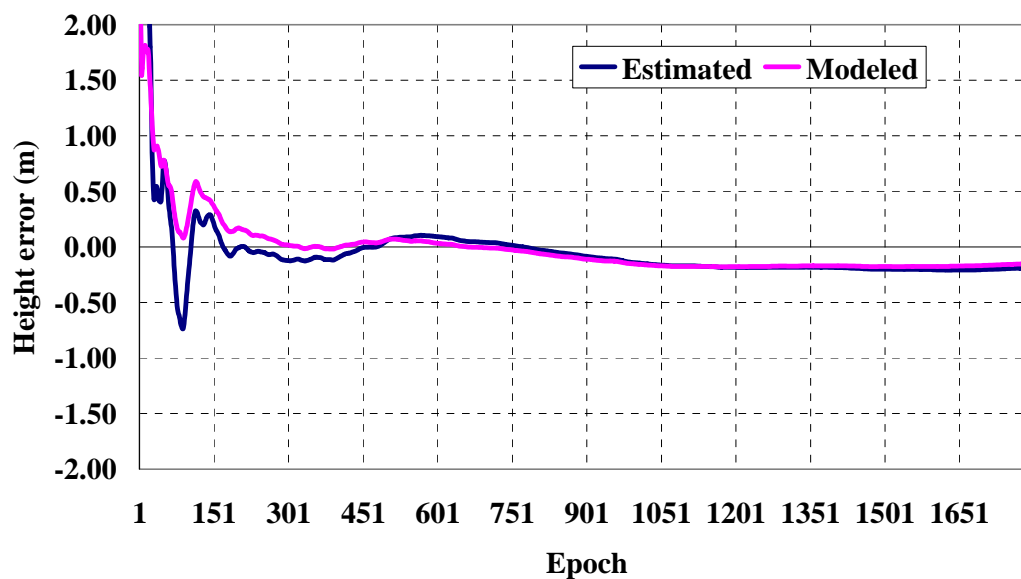
Figure 6.26 Height convergence for May 13 dataset
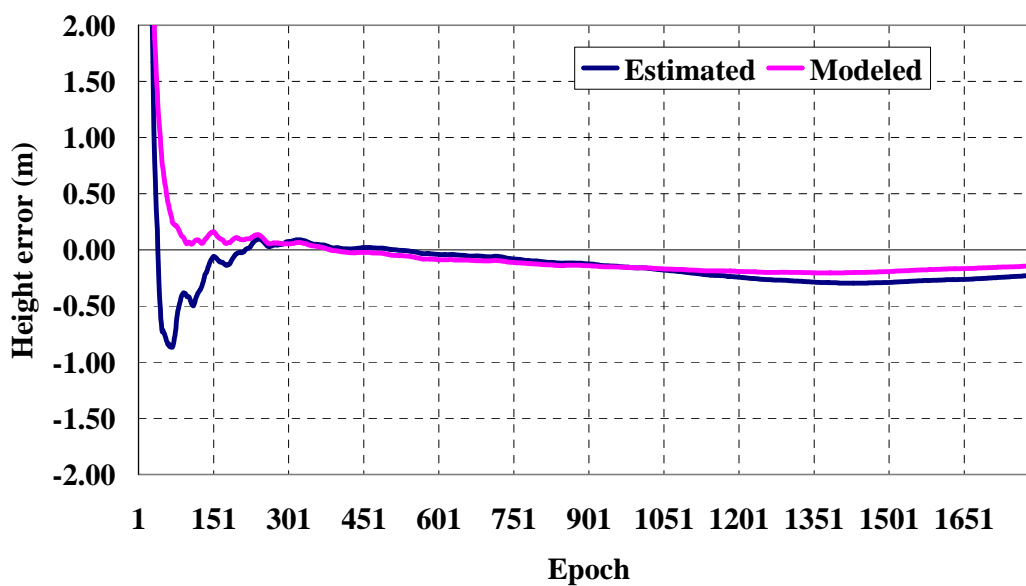
Figure 6.27 Height convergence for May 14 dataset
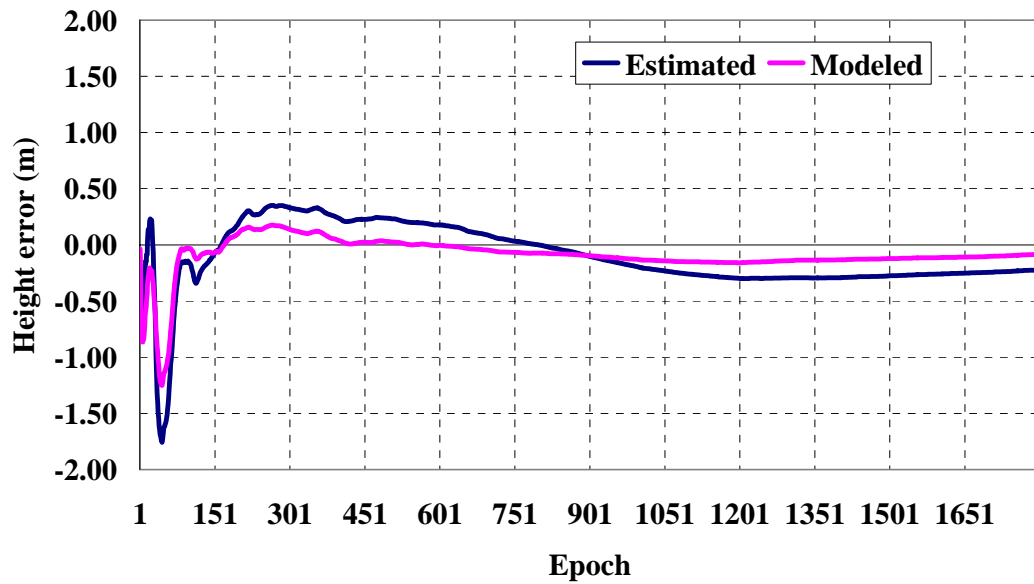
Figure 6.28 Height convergence for May 15 dataset

From comparing Figures 5.23 through 5.28, it can be concluded that modeling the troposphere at the beginning of the processing instead of the estimation can enhance the convergence slightly. However, it is highly unlikely that it could have a great potential effect on convergence time.

6.2.3 Proposed Hybrid Solution

Because of the non-integer nature of PPP ambiguity and the slow change in GPS geometry constellation, a long time of convergence is necessary. In this section, the concept, results, and limitations of a proposed method to accelerate the convergence at the beginning of the solution are presented (Abdel-salam, 2004). PPP suffers from a long time of convergence, but after the convergence, the positioning results become highly accurate. Therefore, if a few decimeters of positioning accuracy can be secured at the

beginning of the processing, this can present a solution for the long time of convergence. The idea of this hybrid solution is not to wait for the complete convergence of the ambiguities but to stop estimating any ambiguities that are believed to be not far from the final solution. Stopping estimating the ambiguities implies removing the successful ambiguities on L1 and L2 from the state vector. This process will have two impacts: the first is to increase the observability of the system because the number of parameters decreases, and the second is to enhance the accuracy because the removed ambiguity is at a sufficient accuracy. It is worth mentioning that this solution will be biased, but this bias should not be a problem because the biased solution could be better than the available float solution.

There are two proposed strategies to integrate this solution with the original solution of PPP. The first is to use the biased solution for a predefined convergence time, then switch directly to PPP, as shown in Figure 6.29. However, this strategy can suffer from position jump owing to the difference between the two solutions.
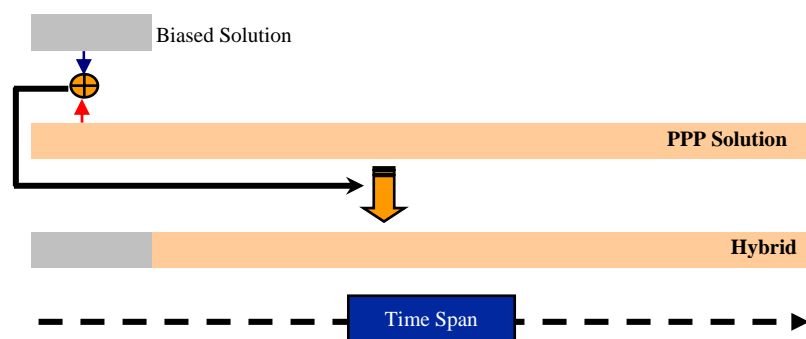
Figure 6.29 The first integration strategy

The second strategy includes the use of a weight scale (0-1) between the two solutions, giving a high weight to the biased solution at the beginning of processing and gradually

reducing this weight to zero at the predefined convergence time. Simultaneously, the PPP solution will have zero weight at the beginning and gradually be increased to one at the predefined convergence time. This strategy is illustrated in Figure 6.30.
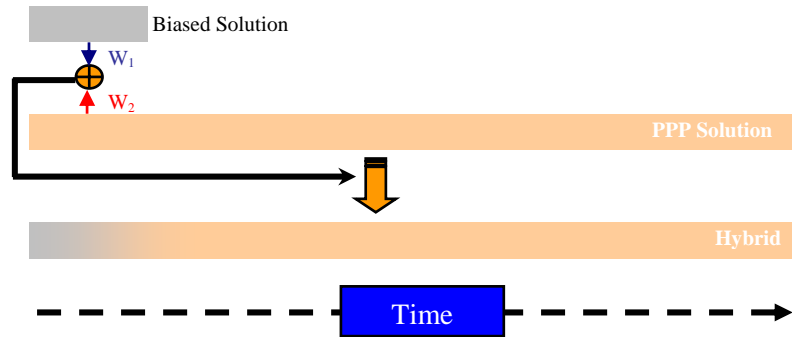
Figure 6.30 The second integration strategy

The hybrid solution can be calculated from Equations 6.7 to 6.9.

$$X = W_1 \cdot X_{Biased} + W_2 \cdot X_{PPP} \tag{6.7}$$

$$W_1 = (1 - t / T_{Pr}) \tag{6.8}$$

$$W_2 = (t / T_{Pr}) \tag{6.9}$$

where

X - hybrid position vector

X_{Biased} - biased position vector

X_{PPP} - PPP position vector

T_{Pr} - predefined convergence time (10 minutes)

W_1 - weight of the biased solution

W_2 - weight of the PPP solution

t - elapsed time which should be less than the predefined convergence time

The following numerical results are based on the testing of three static datasets. Two of them were obtained from the IGS network on January 1st, 2003 while the third was collected at Calgary on September 30, 2003. The two IGS GPS datasets belong to CHUR and WHIT IGS stations with a sampling interval of 30 seconds, while the Calgary dataset has an interval of 1 sec. An elevation cutoff angle of 10 degrees was used. The static data processing scheme that is used in Section 5.1 was employed in this section. Figures 6.31 to 6.34 present the PPP float and biased solutions of the first two IGS static datasets; Figures 6.35 and 6.36 show the results of the Calgary static dataset. The figures also provide statistics about the positioning accuracy.
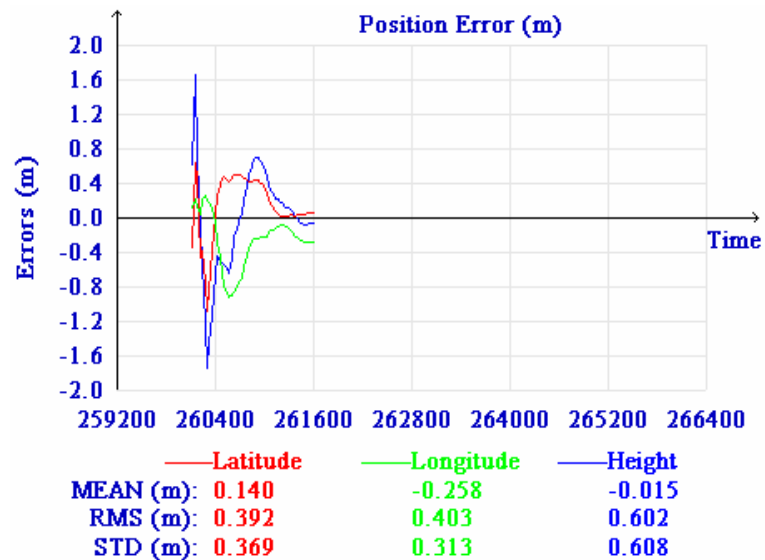
Figure 6.31 PPP solution for the CHUR IGS static dataset
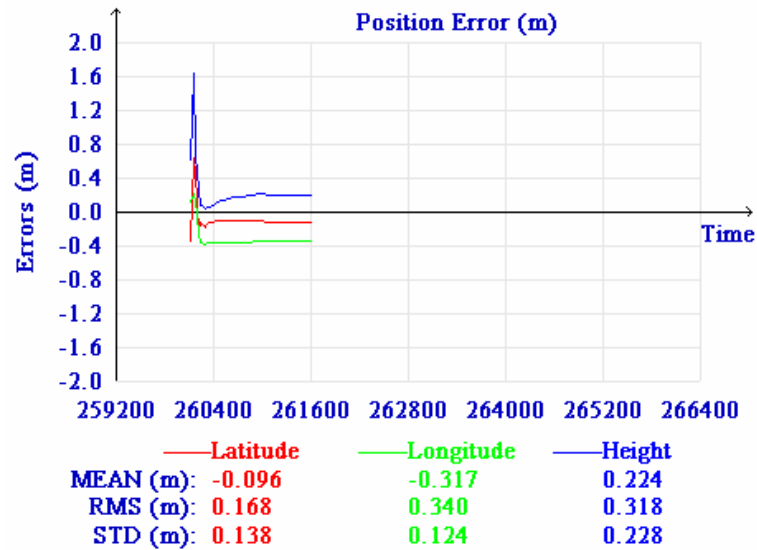
Figure 6.32 Biased solution for the CHUR IGS static dataset

By comparing Figure 6.31 with 6.32, it is evident that the proposed biased solution has reduced the positioning error in latitude and height to half their original values, while it reduced the positioning errors in longitude direction by 15%. At the same time, the biased solution has converged within a few epochs. Figures 6.33 and 6.34 show similar results in the position and time domains. The reduction of the errors in the position domain was almost 50% of the corresponding PPP float solution. Figures 6.33 and 6.34 present the result of the second IGS static dataset.
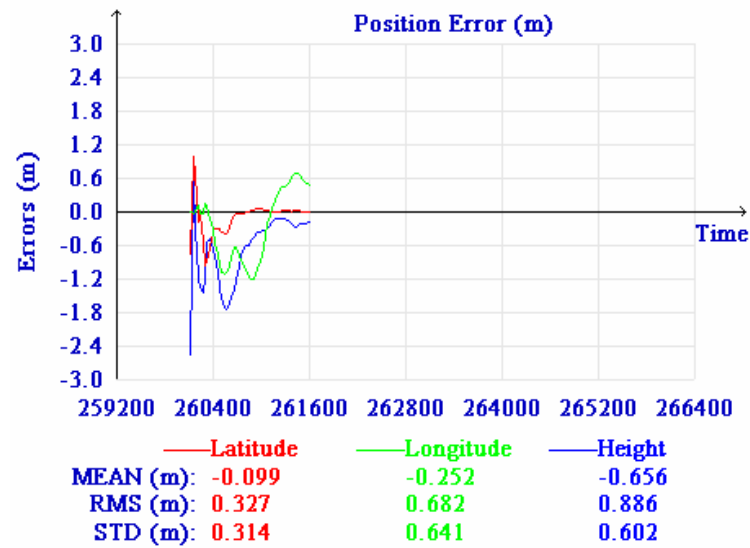
Figure 6.33 PPP solution for the WHIT IGS static dataset
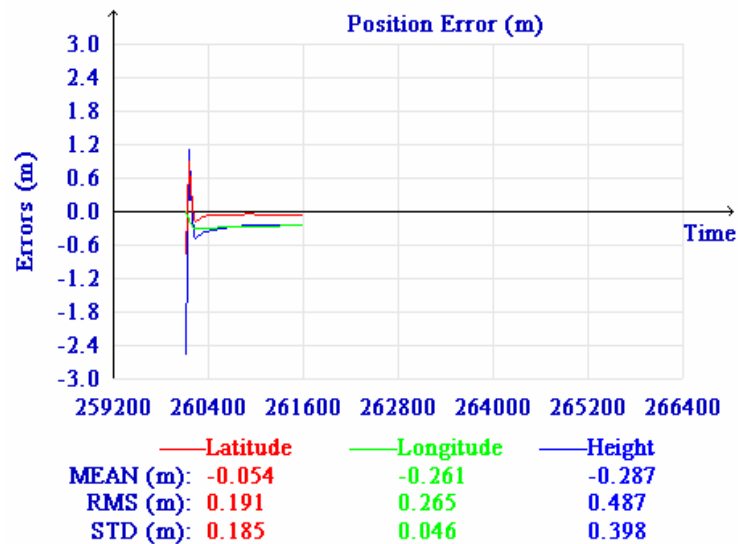
Figure 6.34 Biased solution for the WHIT IGS static dataset

For the two IGS datasets, when the estimated variance of the float ambiguities was in the range of 10 cycles, the proposed biased solution produced positioning results comparably better than the PPP float solution. However, for ranges far from this variance, the

accuracy could be significantly different. As a result, the selection of the variance value is a challenging task and can be achieved by testing several variance values.

The results obtained from the Calgary static dataset showed a better biased solution in latitude and longitude directions compared with the PPP float solution as shown in Figures 6.35 and 6.36. There is a reduction in latitude and longitude errors of 3% and 63%, respectively. However, a positioning error increase in the height direction was observed. This increase could be caused by the improper selection of the variance value. It is worth mentioning that a different variance value is used for this dataset. The reason for changing the variance value is the dissimilarity in observation intervals and data quality between the IGS and Calgary datasets. Experimental results show that a unit value (cycle) for the variance corresponds to the best biased solution.
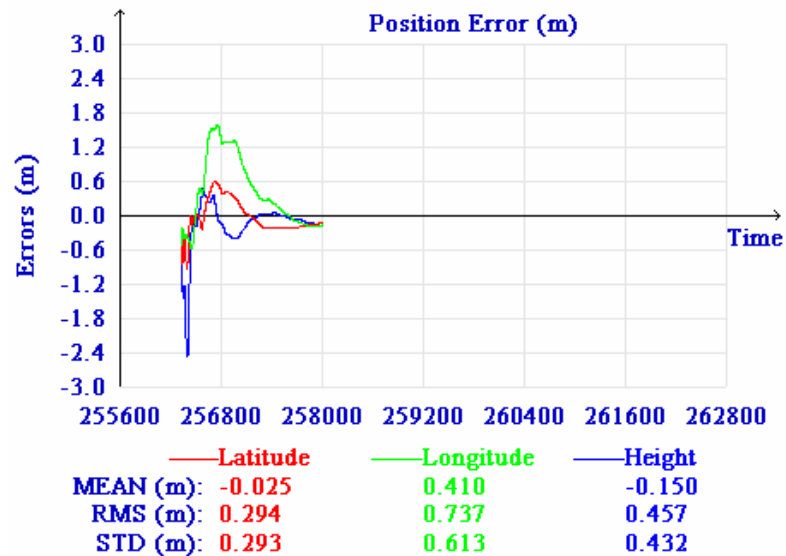
Figure 6.35 PPP solution for Calgary static dataset
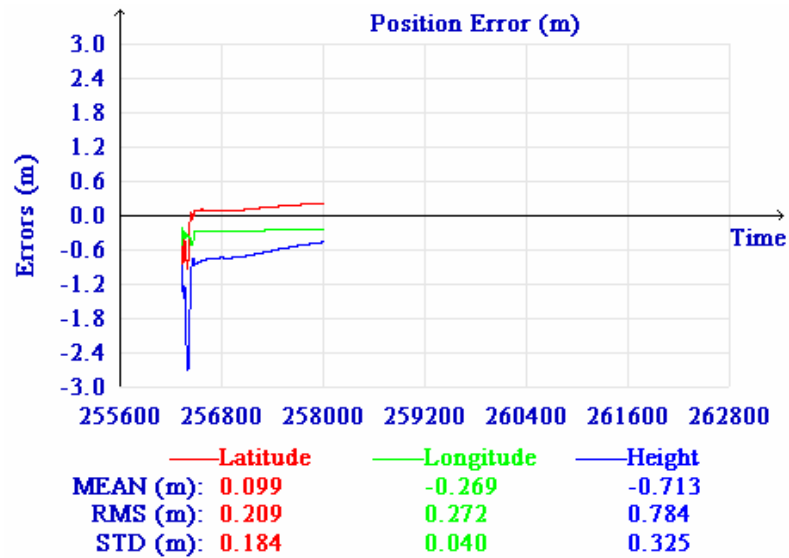
Figure 6.36 Biased solution for Calgary static dataset

The numerical results show an interesting characteristic of the stochastic properties of the PPP parameters. These stochastic properties need scaling to express the accuracy of the parameters. This is the reason why constraining an ambiguity with a variance value of 10 produces good positioning results. Nevertheless, this proposed biased solution depends on the optimum value of the variance. As can be observed from the results, this method will always be a function of the chosen variance threshold. Consequently, this method is not general and works only in some datasets, so it is not recommended.

6.3 Ambiguity Comparison in the two PPP Models

This section describes an investigation to compare the ambiguities obtained from the traditional and the UofC models. This comparison was done by transforming the absolute ambiguities on L1 and L2 from the UofC model (Section 4.3.2) to the traditional model (Section 4.3.1) as illustrated in Equation 6.10.

$$N_{Traditional} = \frac{f_1^2 N_1 - f_2^2 N_2}{f_1^2 - f_2^2}$$
(6.10)

where

N_1	- Ambiguity on L1
N_2	- Ambiguity on L2
f_1	- L1 frequency
f_2	- L2 frequency
$N_{Traditional}$	- Reconstructed ambiguities for the traditional model

Data from the IGS station AMC2 collected on August 1, 2004 was used for this purpose. Precise orbit and clock data at intervals of 15 minutes and 30 seconds were used. An elevation cutoff of 10 degrees was chosen. A static estimation scheme similar to the one used in Section 5.1 was adopted. Figures 6.37 and 6.38 show the results of the ambiguity transformation for the case of two satellites. The two figures show that the two models are essentially equivalent in ambiguities parameterization. The difference between the ionosphere free ambiguities obtained from UofC and the traditional models is negligible. This can be interpreted in two ways. The first interpretation is that the inter-frequency bias on L1 and L2 of the UofC model joined the ambiguity in the estimation process and

cancelled when constructing the ionosphere-free ambiguities. This interpretation can contradict itself because on one hand it implies that the ambiguities in Equations 4.22, 4.23, and 4.24 are the same in the estimation filter. On the other hand, it assumes the ambiguities in Equations 4.22 and 4.23 are different from 4.24. The ambiguities in Equations 4.22 and 4.23 contain the inter-frequency bias whereas the ambiguities in 4.24 are free from the inter-frequency bias. Accordingly, the difference of the ambiguity re-parameterization should show up in Figures 6.37 and 6.38, even if the given weight of Equation 4.24 is assumed large. The second interpretation is that the inter-frequency bias of code and carrier phase may have the same value but with different sign. This fading effect will be confirmed in Chapter 7 when analyzing the results of a new approach for estimating the ionospheric delay.
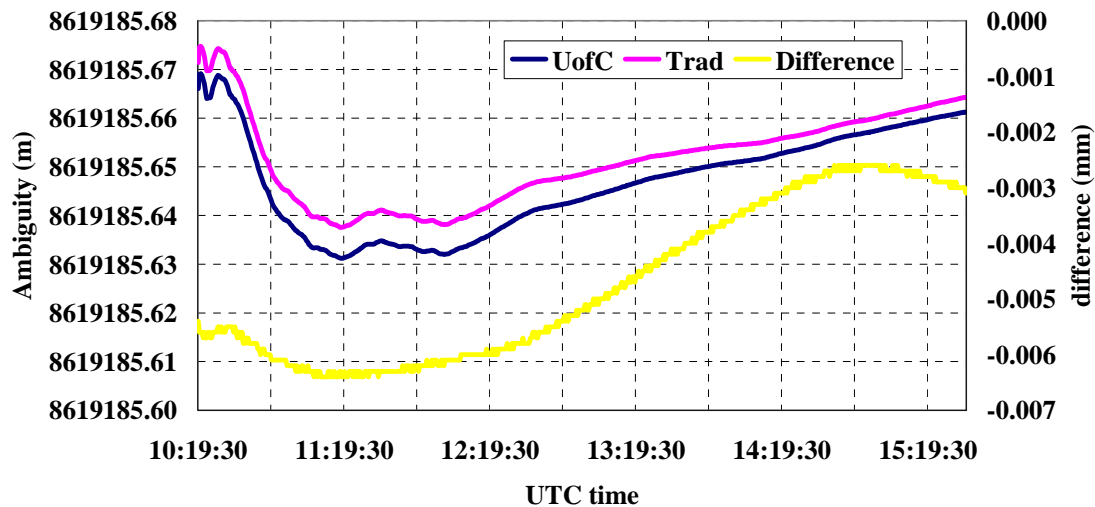
Figure 6.37 PRN 5 ionosphere-free ambiguity representation
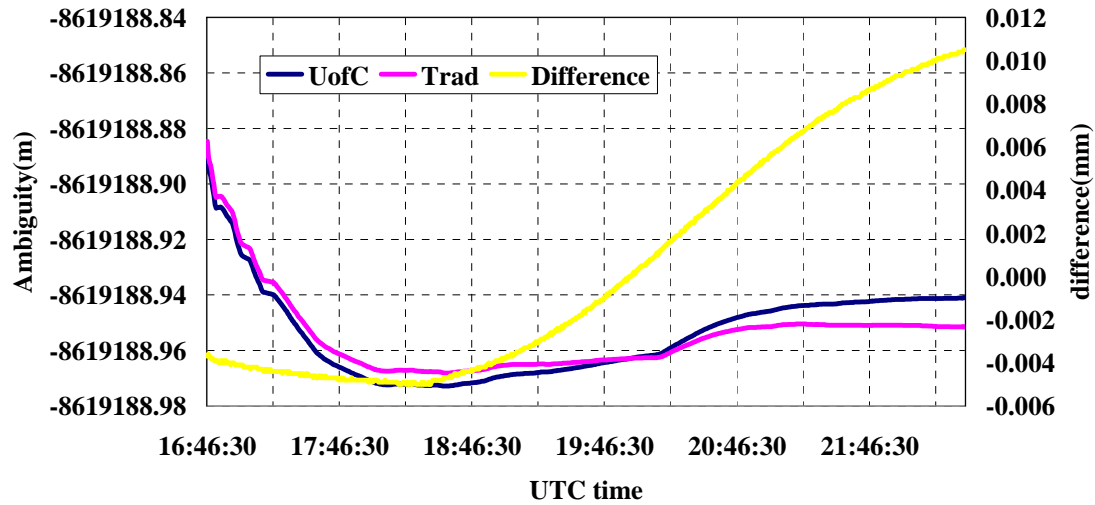
Figure 6.38 PRN 15 ionosphere-free ambiguity representation

6.4 Summary

In this chapter, several aspects have been investigated and analyzed. These aspects include the non-zero initial phase of carrier phase, the applicability of ambiguity resolution in PPP, the convergence, and the ambiguity representations in both PPP models. It has been concluded that it is highly unlikely that the un-differenced ambiguity can be fixed because it lost its integer nature due to the non-zero initial phase and the other systematic errors such as satellite antenna phase center offset. The use of satellite clock corrections and observation measurements at small intervals enhance the convergence of PPP. Stopping estimating the accurate ambiguity can, in some cases, enhance the convergence and the accuracy but it is highly unlikely to be a generic solution. Modeling the troposphere instead of estimating it at the beginning of the

solution can enhance the solution slightly. The two functional PPP models showed the equivalences of the ambiguity representation.

CHAPTER 7

PRECISE ATMOSPHERE SENSING FROM PPP

7.1 Introduction

Recent research has shown that GPS can be used as a powerful sensor to monitor tropospheric and ionospheric delays (Abdel-salam and Gao, 2004). Numerous applications rely on these delays, including weather forecast, wireless communication, and many geophysical applications such as earthquake prediction (Abdel-salam, 2005). This chapter, therefore, investigates PPP based absolute tropospheric and ionospheric delay estimation and their associated accuracies.

7.2 PPP Zenith Tropospheric Delay Estimation Scheme

Troposphere is a major source of GPS errors and can cause delays of a few meters at zenith to a couple of meters at low elevations (Jense, 2002; Mendes, 1999; Misra and Enge, 2001). It can be considered as the largest error in PPP after the mitigation of ionosphere, orbit, and clock errors. In order for PPP to obtain a high positioning accuracy, the delay error caused by the troposphere must be accounted for through

estimation. Therefore, a combination of stochastic and functional models for the tropospheric delay was developed. The functional model uses Niell's mapping function and the Hopfield model, while the stochastic model considers the tropospheric delay error as a Random Walk. The Niell mapping function and Hopfield model are given in Section 3.2.2. The selection of this functional model is based on several publications and recommendations as well as on the merits of the Niell's Mapping function, such as its ability to perform well in both low and high elevations and its independence from meteorological parameters (Leick, 2004; Witchayangkoon, 2000). The deterministic and stochastic models are presented in Equations 7.1 and 7.2 for convenience.

$$\Delta_{\text{Trop}} = \Delta_{\text{wet}} \, M_{\text{wet}} + \Delta_{\text{dry}} \, M_{\text{dry}} \tag{7.1}$$

$$\dot{\Delta}_{Trop} = w(t) \tag{7.2}$$

where,

Δ_{wet} - the wet component

Δ_{dry} - the dry component

M_{wet} - the wet mapping function

M_{dry} - the dry mapping function

$w(t)$ - white noise

From the Kalman filter's implementation point of view, this model takes on a slightly different form. First, at the first epoch of processing an initial total zenith tropospheric delay can be estimated based on rough surface meteorological parameters. Afterwards, a correction part estimated from the Kalman filter is added to the total zenith tropospheric delay at each epoch. The Kalman filter's state vector includes one value for the

tropospheric delay correction. Either the wet or dry mapping function can be used to map the tropospheric delay correction. The wet tropospheric delay component is usually hard to model; therefore, the state vector element corresponding to the tropospheric delay correction can be considered as a correction to the wet component as well as to the total tropospheric delay when using a wet mapping function. By this way, a single correction value is considered each epoch for the tropospheric delay. The Niell's wet mapping function was used in the functional model to map the zenith value of the tropospheric correction to slant delay, as given in Equation 7.3. This method of tropospheric delay estimation was used in Chapter 5 and in Section 6.2.7 to compare the effect of tropospheric delay estimation and modeling on the convergence behavior.

$$\Delta_{\text{Trop Slant Delay Correction}} = \Delta_{\text{wet correction}} \, M_{\text{wet}} \qquad (7.3)$$

where

$\Delta_{\text{wet correction}}$ _ kalman filter troposphere state element

7.3 Effect of Input Parameters on the Estimated ZTD

This section addresses the effect of stochastic and initial meteorological parameters on the accuracy of zenith tropospheric delay. First, zenith tropospheric delay estimated using different initial meteorological parameters is addressed. Afterwards, the effect of stochastic parameter selection is investigated and analyzed. A one-day static GPS dataset from the IGS ALGO station was used for this purpose. The used dataset was collected on January 31, 2003, and the sampling interval of the observations is 30 seconds.

7.3.1 Initial Meteorological Parameters

This section describes the results of using two sets of initial meteorological parameters to study their influence on the zenith tropospheric delay estimation. These two sets are illustrated in Table 7.1. Using the IGS ALGO dataset, collected on January 31, 2004, the zenith tropospheric delay was estimated for the two sets of meteorological parameters. A cutoff angle of 10 degrees was used. Position, receiver clock bias, and ambiguity parameters are modeled according to the static estimation scheme used in section 5.1.

Table 7.1 Two sets of initial meteorological parameters

	Pressure	Temperature	Humidity	A priori variance	Spectral density
Met-I	1010 mbar	15 c	50%	40 cm	10e-9 m^2/s
Met-II	800 mbar	-15 c	70%	40 cm	10e-9 m^2/s

Figure 7.1 shows the resulting ZTD using both meteorological datasets. The figure illustrates that the initial meteorological parameters have an effect only on a couple of epochs at the beginning of processing. For the used dataset, this effect extends to about 10 epochs but afterward there is no remarkable effect. However, this conclusion should be observed along with the value of the *a priori* variance given to the tropospheric delay. The independence of the estimated ZTD from the initial meteorological parameters gives additional merit to PPP. Therefore, users using PPP do not need to worry about deploying any meteorological sensors or guessing accurate meteorological parameters. However, if a user is interested in retrieving the tropospheric wet delay component, meteorological data would be essential.
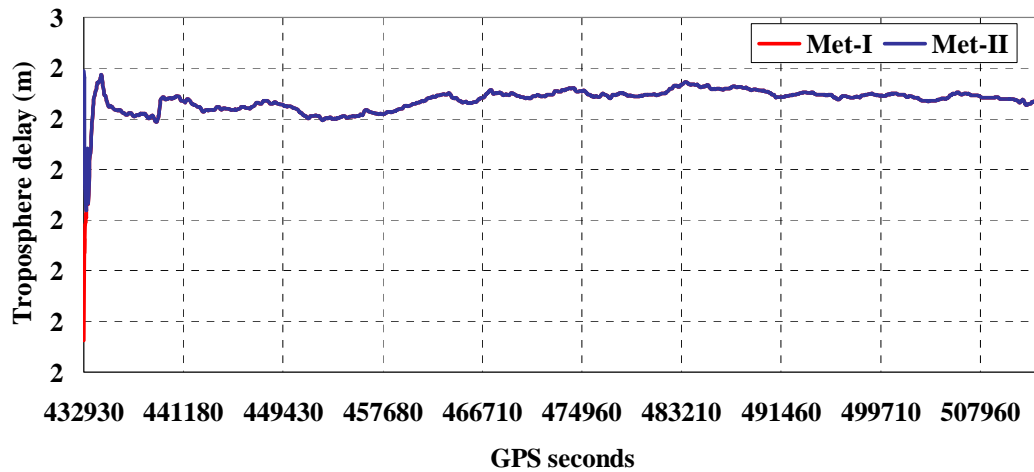
Figure 7.1 ALGO ZTD using two sets of meteorological parameters

7.3.2 Stochastic Parameters

This section gives the analysis of the tropospheric zenith delay that was estimated using four scenarios of stochastic parameters. The analysis done shows the difference in the estimated zenith tropospheric delay when using values of 10^{-10} m^2/s, 10^{-9} m^2/s, and 10^{-8} m^2/s for the troposphere spectral density and values of 40 cm and 10 cm for the ZTD *a priori* variance. These values of spectral density are the common value used by many research works to model the stochastic properties of tropospheric delays (Zumberge et al.., 1998; Kouba and heroux, 2000; Jin and Wang, 2004; Niell et al.., 2001). These parameters are summarized in Table 7.2.

Table 7.2 ZTD initial and stochastic parameters

	Pressure	Temperature	Humidity	A priori variance	Spectral density
Stoch-I	1010 mbar	15 c	50%	40 cm	10e-10 m^2/s
Stoch-II	1010 mbar	15 c	50%	40 cm	10e-9 m^2/s
Stoch-III	1010 mbar	15 c	50%	40cm	10e-8 m^2/s
Stoch-IV	1010 mbar	15 c	50%	10cm	10e-9 m^2/s

Based on the analysis of ZTD for the ALGO dataset, Figure 7.2 shows the difference in ZTD when Stoch-I and Stoch-II are applied; Figure 7.3 shows the difference in ZTD when Stoch-I and Stoch-III are applied. The graphs show nearly the same trend, with the latter showing a noisier trend. Therefore, it is important to choose the right spectral density based on the meteorological characteristics of the region containing the GPS station and the mode of observations. A spectral density of value 10e-9 m^2/s for the troposphere was observed to perform well with many datasets.
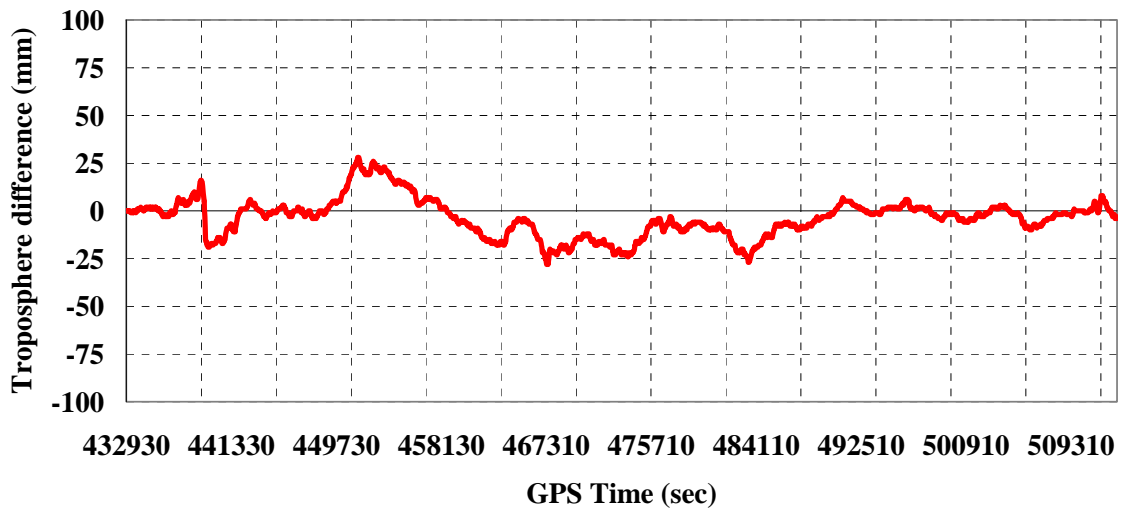
Figure 7.2 ZTD difference between the Stoch-I and Stoch-II
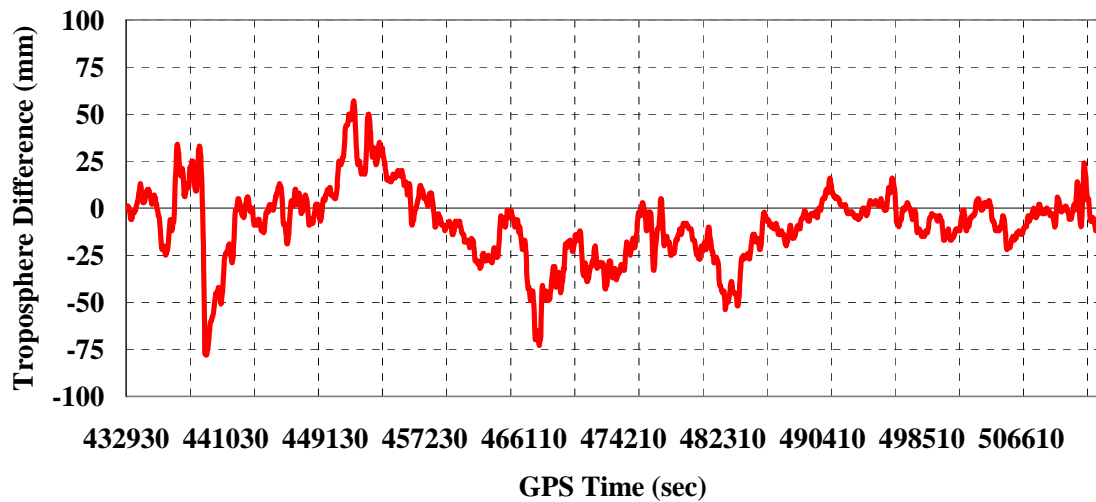
Figure 7.3 ZTD difference between the Stoch-I and Stoch-III

The statistics corresponding to Figure 7.3 show a bias of -3.73 mm and a standard deviation of 10 mm, whereas the statistics corresponding to Figure 7.4 show a bias of -8.37 mm and a standard deviation of 19.4 mm. Generally speaking, larger difference in the spectral density will result in larger difference in the estimated ZTD.

Figure 7.4 shows that there is an insignificant difference in ZTD delay from using different values of the ZTD *a priori* variance. The statistics show a bias of -4 mm and a standard deviation of 11.5 mm. It is worth mentioning that the effect of the initial *a priori* variance can cause problems, especially if the chosen value was very small. This is because the Kalman filter will tend to allow very little tropospheric delay variation from the initial values. Thus, the situation can look more like modeling than estimation. It is preferable to use a large *a priori* variance (50 cm) for tropospheric delay if meteorological data is not available.
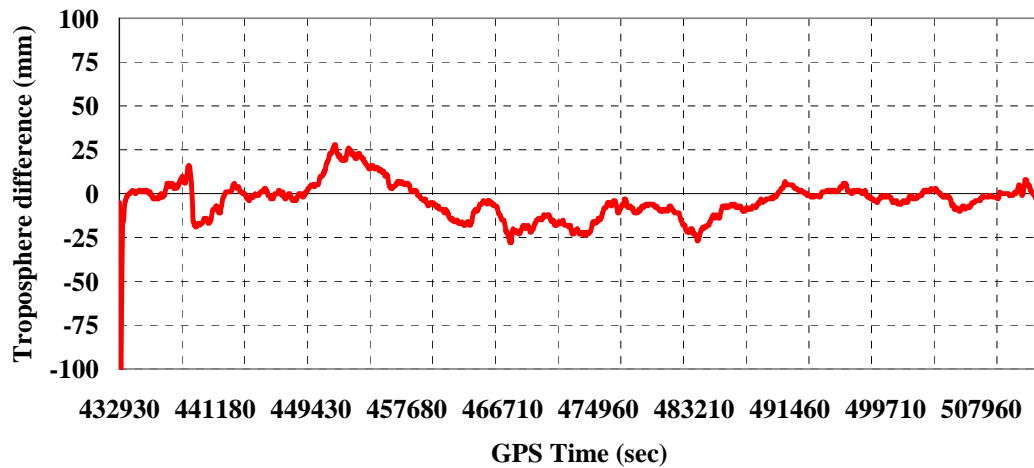
Figure 7.4 ZTD difference resulting from the Stoch II-IV parameter set

7.4 Troposphere Estimation from PPP and IGS Analysis Centers

IGS produces several tropospheric delay products. The most accurate one is the final product, which has an accuracy of 4 mm at an interval of two hours, and a latency of four weeks. The tropospheric delay format is known as SINEX_TROPO; it contains tropospheric zenith delay and its accuracy every two hours (IGS, 2004b; SINEX_TROPO, 2004). When meteorological surface parameters are available at the IGS station, their values appear in the SINEX_TROPO file as well as the corresponding precipitable water vapor (IGS, 2004b). However, it seems that this format is designed for future expansion. Currently, it contains only the zenith tropospheric delay and its accuracy, whereas the meteorological surface parameters are recorded in a different file when the IGS site is equipped with instruments that measure them. The three IGS stations marked in Figure 7.5 are used here.
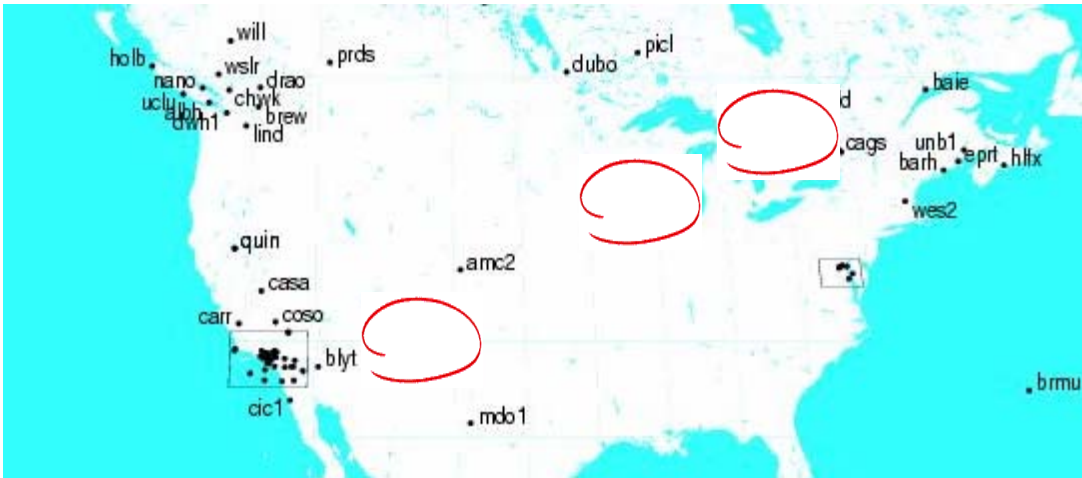
Figure 7.5 Used IGS stations (http://igscb.jpl.nasa.gov/images/nam.jpg)

The zenith tropospheric delay of the three IGS stations was estimated for the period of time from January 1 to January 31, 2003. The resulting tropospheric delay from PPP was compared with the corresponding IGS final zenith tropospheric delay for each of the three IGS stations. The used IGS datasets have a sampling interval of 30 seconds and an elevation cutoff angle of 10 degrees was used. The static processing scheme that was used in Section 5.1 is adopted in this section. The IGS final orbit and clock corrections at intervals of 15 and 5 minutes were used. The stochastic and meteorological parameters used for this purpose are shown in Table 7.3.

Table 7.3 Troposphere initial and stochastic parameters

Parameter	Pressure	Temperature	Humidity	A priori variance	Spectral density
Value	1010mbar	15c	50%	40 cm	10e-9 m^2/s

7.4.1 IGS ALGO Station' ZTD

Figure 7.6 shows the consistency of the zenith tropospheric delay obtained from the PPP UofC model and IGS. The graph illustrates a bias of 13.7 mm and a standard deviation of 18.8 mm.
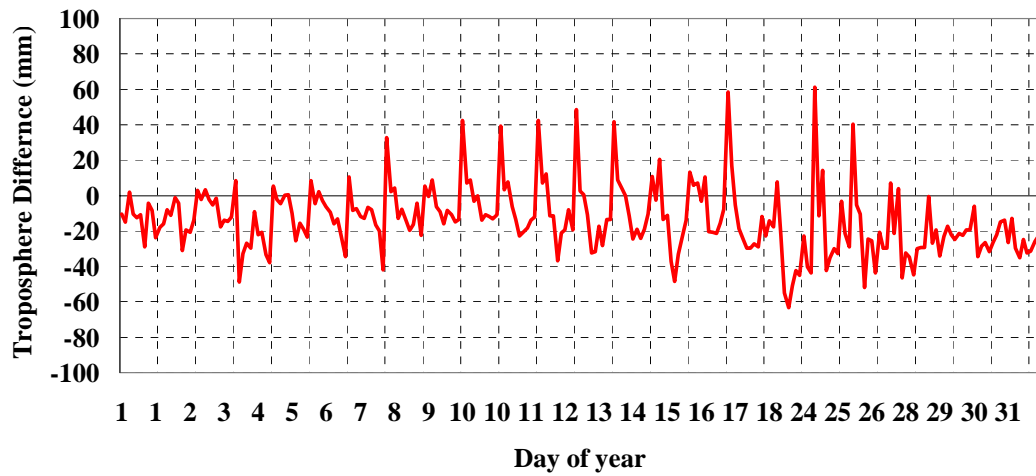
Figure 7.6 ZTD Difference for ALGO station using UofC model

In contrast, the ZTD difference resulting from the PPP traditional model shows a bias of 3.3 mm and a standard deviation of 18 mm, as shown in Figure 7.7. When conservative spectral density values are used, or when long parts of the data are excluded at the beginning, the bias and standard deviation could be greatly reduced. In this section, two hours of data were excluded at the beginning of each day.
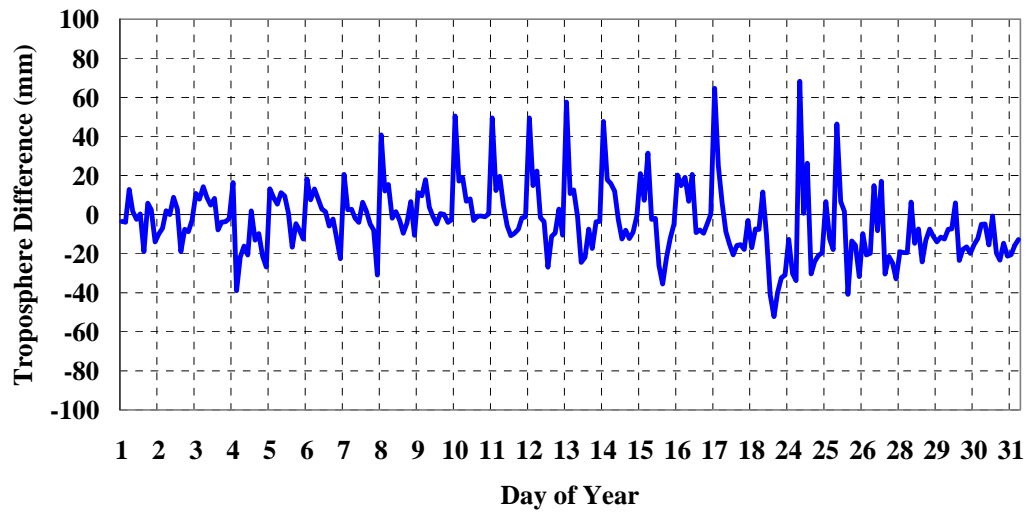
Figure 7.7 ZTD Difference for ALGO station using traditional model

7.4.2 IGS AMC2 Station' ZTD

Figure 7.8 shows the ZTD difference between PPP and IGS zenith tropospheric delay for

the month of January 2003 using the UofC model.
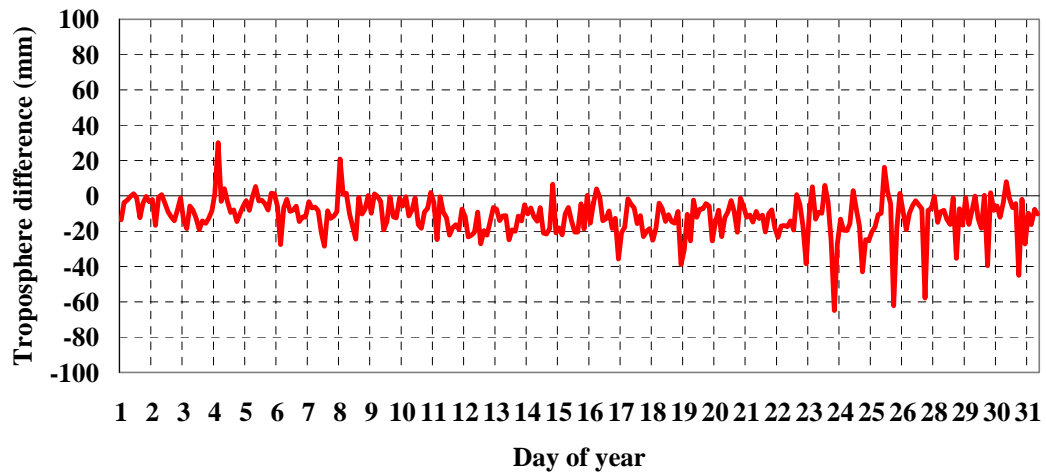
Figure 7.8 ZTD Difference for AMC2 station using PPP UofC model

The AMC2 station zenith tropospheric delay difference shows a better agreement with

IGS compared with the previous results for the ALGO IGS station. The bias is -11.3 mm,

and the standard deviation is 10.8mm. For the case of the PPP traditional model, as illustrated in Figure 7.9, the bias was -2.2 mm and the standard deviation was 10.7 mm.
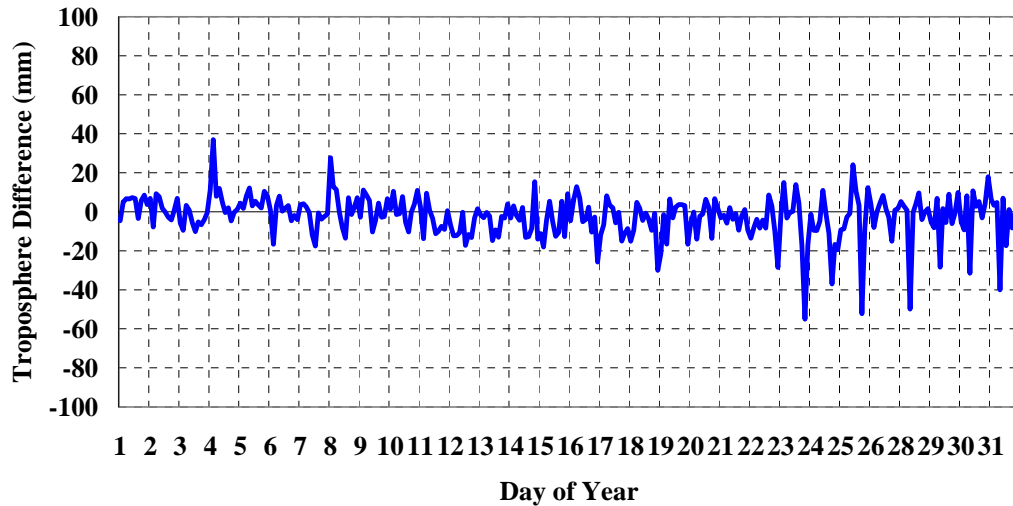
Figure 7.9 ZTD Difference for AMC2 station using PPP traditional model

7.4.3 IGS PIE1 Station' ZTD

In this section, the zenith tropospheric delay was estimated for the whole month of January and compared with the final product obtained from IGS for the IGS PIE1 station. The results shown in Figure 7.10 show a bias and a standard deviation of -13.8 mm and 14.5 mm, respectively.
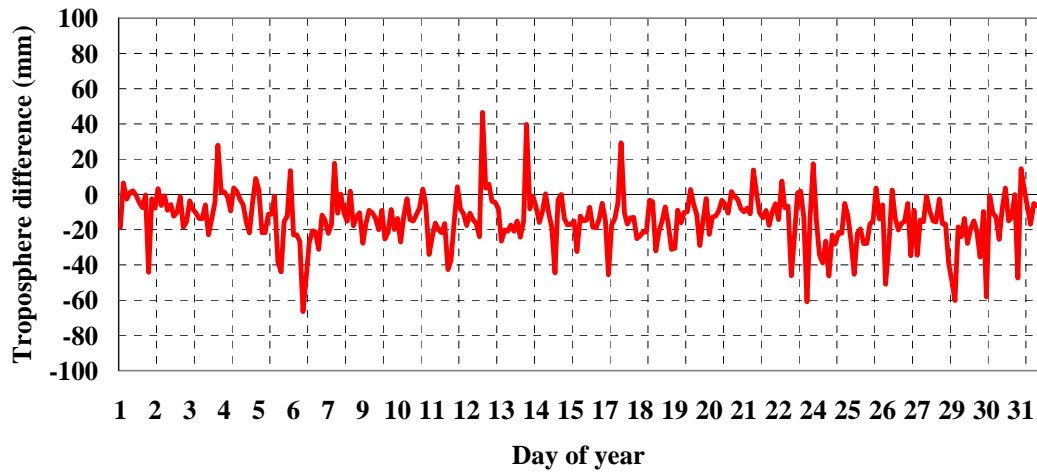
Figure 7.10 ZTD Difference for PIE1 station using PPP UofC model

Using the PPP traditional model, a bias of 1.4 mm and a standard deviation of 19 mm are achieved. The ZTD difference is shown in Figure 7.11.
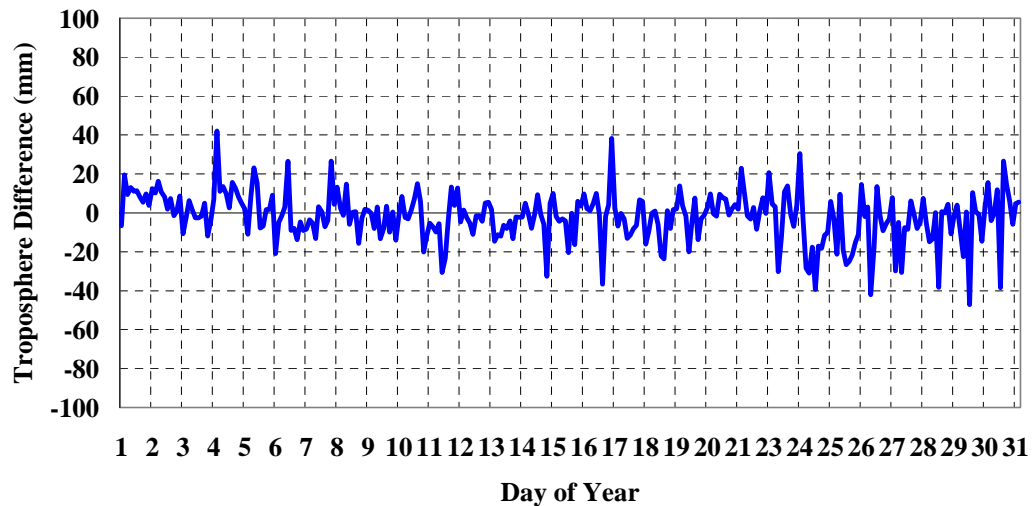
Figure 7.11 ZTD Difference for PIE1 station using PPP traditional model

The results of zenith tropospheric delay obtained from the three stations show differences better than two centimeters. Troposphere zenith delay obtained from the ALGO station performs poorly compared with the other two IGS stations. The reason for this could be

attributable to the difference in satellites geometry and the exclusion of five days of ALGO station data that suffered from multiple short periods of insufficient numbers of satellites. It is worth mentioning that the biases resulting from the PPP traditional model are significantly less than that of the UofC model, while the standard deviations of the two models are comparable. This bias difference can be attributed to the long convergence time needed for ZTD obtained based on the UofC model. The big values appeared during several days can be attributed to GPS datasets and the 5 minutes clock corrections. The 4 mm accuracy reported for the final IGS tropospheric delay is actually the precision of different IGS troposphere solutions with respect to each others and is not an absolute accuracy. The tropospheric delay convergence is a function of many issues such as the PDOP values, quality of code observations, and cycle slips. Depending on these issues, the convergence can vary from day to day. This day to day variation can be observed in Figures 7.6 to 7.11 above. Figure 7.12 shows the difference of the number of satellites and the PDOP values for AMC2 station on January 1st and 31, 2004.
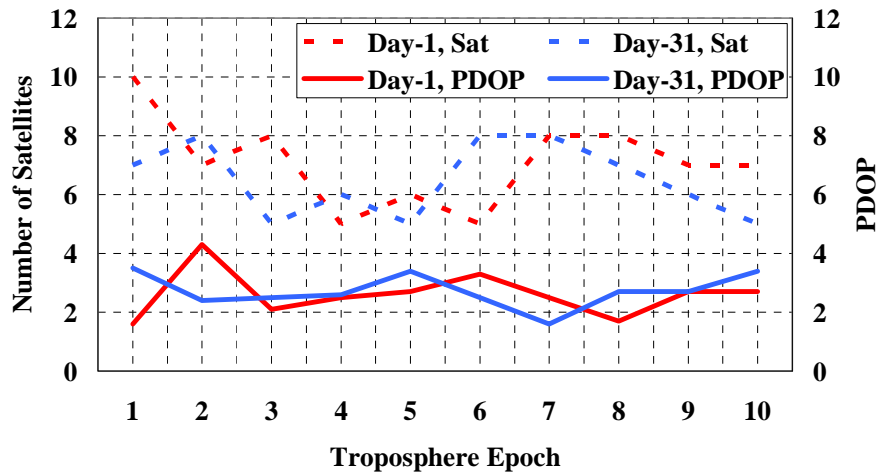
Figure 7.12 PDOP and the number of satellite at AMC2 station

It can be concluded from Figure 7.12 that January 31 dataset has a weaker geometry at the beginning of the day compared to January 1st. This difference in geometry could be the cause for the big tropospheric delay difference that is observed during January 31 as depicted in Figures 7.8 and 7.9.

7.5 Tropospheric Delay from PPP and WVP

The atmosphere particles radiate microwave signals that can be retrieved at the Earth's surface. These emitted microwave signals have different characteristics based on their height from the Earth's surface. A water vapor profiler (WVP) is a passive sensor that receives these microwave radiations at several frequencies. By observing this radiation at selected frequencies, accurate atmospheric temperature, water vapor and cloud liquid distribution up to a height of 10 km can be obtained (Radiometric Corporation, 2004).

At the University of Calgary, a GPS station was installed beside a WVP and a meteorological sensor (*MET3A*). Data from the three mentioned instruments was collected and the wet zenith tropospheric delay was derived. The difference between the two solutions is compared as will be shown in the next sections.

7.5.1 Wet ZTD Obtained from WVP

The University of Calgary has a water vapor profiler, WVP-1500, Radiometrics Corporation. The WVP observes five frequency channels between 22 and 30 GHz to determine the vertical water vapor distribution. In addition to the WVP, a surface

meteorological sensor is available that allows for the observation of temperature, pressure, and humidity. To compare the zenith tropospheric delay obtained from PPP and the WVP, the WVP retrieves the wet tropospheric delay component for the GPS constellation by aiming at each individual GPS satellite. The WVP can provide the wet tropospheric delay every several minutes for the same satellite and about one minute for different satellites. The accuracy of zenith wet tropospheric delay obtained from WVP can reach few millimeters when WVP instrument is subjected to continuous calibration and maintenance (Niell et al.., 2001). Figures 7.13 and 7.14 show the WVP slant and zenith tropospheric delay as well as the satellite elevation with respect to time for PRN 1 and 29. The two figures illustrate that the Wet Zenith Delay (WZD) changes by a few centimeters with respect to the elevation angle. Conversely, the Wet Slant Delay (WSD) is significantly affected by the elevation angle. A close look at the slant and zenith delays shows that the used mapping function is "sin(elevation)"
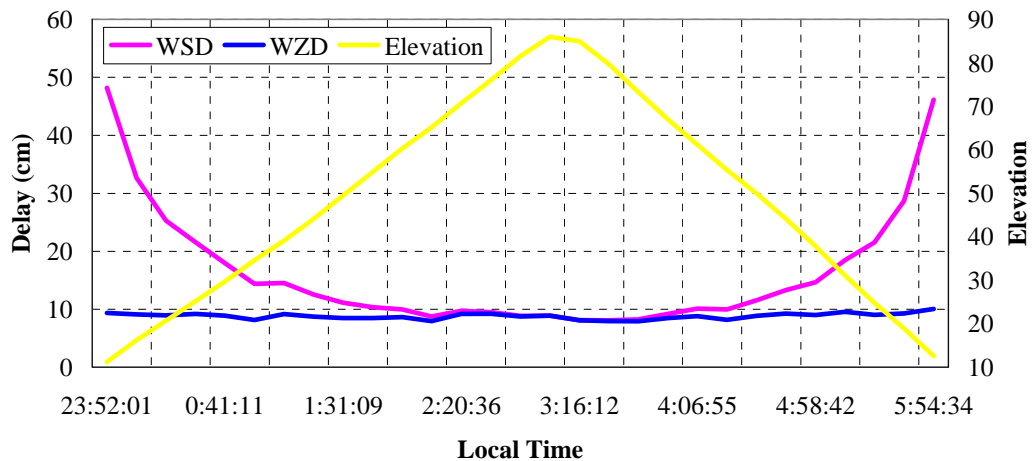
Figure 7.13 Zenith and slant WVP data for PRN1
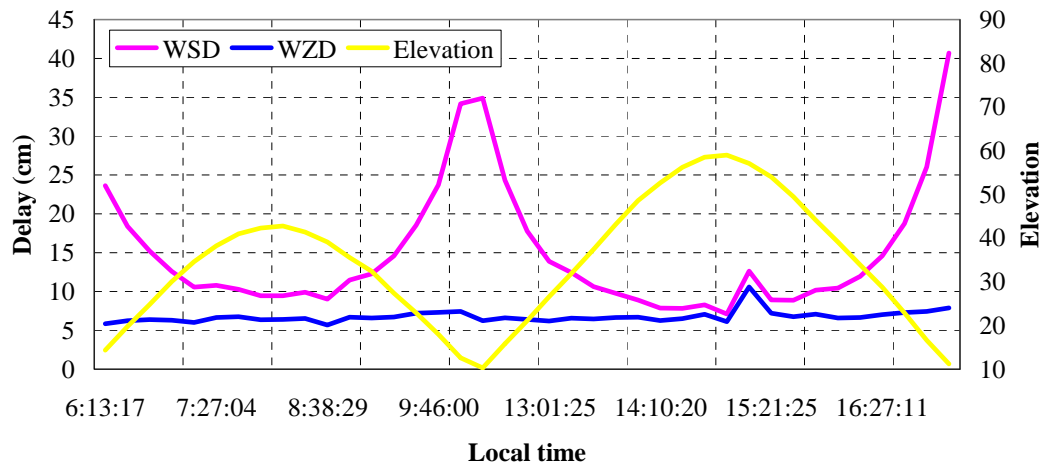
Figure 7.14 Zenith and slant WVP data for PRN29

7.5.2 Wet PPP and WVP ZTD differences

Several days of *WVP-1500* data and their corresponding GPS as well as meteorological data were obtained from a *MET3A* surface meteorological sensor, and a Javad GPS receiver respectively. These days are May 12, 13, 14, 15, 16, and 18, 2004. The Javad GPS datasets have a sampling interval of 1 second and an elevation cut off angle of 10 degrees. Receiver antenna phase center offset and variation effects were considered. Precise IGS final orbit and clock correction at intervals of 15 and 5 minutes are used. A static estimation scheme similar to what used in section 5.1 is adopted for the static GPS datasets that are used in this section. The used meteorological data contains temperature, pressure, and humidity at an interval of 30 seconds. To estimate the wet zenith tropospheric delay from PPP, the total zenith tropospheric delay was estimated every epoch and the dry component was calculated using the Hopfield model as illustrated previously in Equation 3.3. The dry component was then removed from the zenith

tropospheric delay, resulting in an estimation of the wet component. The accuracy of modeling the dry zenith tropospheric delay is very accurate (Hofmann et al.., 2001; Mendes, 1999) and can reach mm level when using accurate meteorological surface parameters (Misra and Enge, 2001).

Figures 7.15 and 7.16 show the consistency between the wet zenith tropospheric delays obtained from the WVP and PPP using the traditional and UofC models. The PPP based UofC model shows a difference bias of 5 mm and a standard deviation of 20 mm; the PPP based traditional model shows a bias of 8 mm and a standard deviation of 19 mm. If a very conservative troposphere spectral density of 10^{-18} m^2/s is used, the difference between PWV data and PPP traditional model troposphere results reaches 3 and 7 mm, for the bias and standard deviation respectively. There are a few spikes in the results. These spikes can mainly be attributed to many reasons such as the epoch matching process and the WVP data. As mentioned earlier, WVP provide the data every a few minutes and without a fixed sampling rate. Different from WVP data, GPS and meteorological data have a fixed sampling interval. Because of the limited number of matching epochs, the corresponding epochs from WVP and PPP solutions that are within 30 second are compared. No interpolation within these 30 seconds was necessary because the value of tropospheric delay was assumed unchanged during this short time. In addition, some of the spikes are mainly caused by the WVP behavior as shown in Figure 7.17. A close examination of the figure shows that the spikes in the WVP are responsible

for spikes in the WZTD difference. These spikes can be attributed to the existence of water drops at the service of the WVP instrument (Skone, 2005).
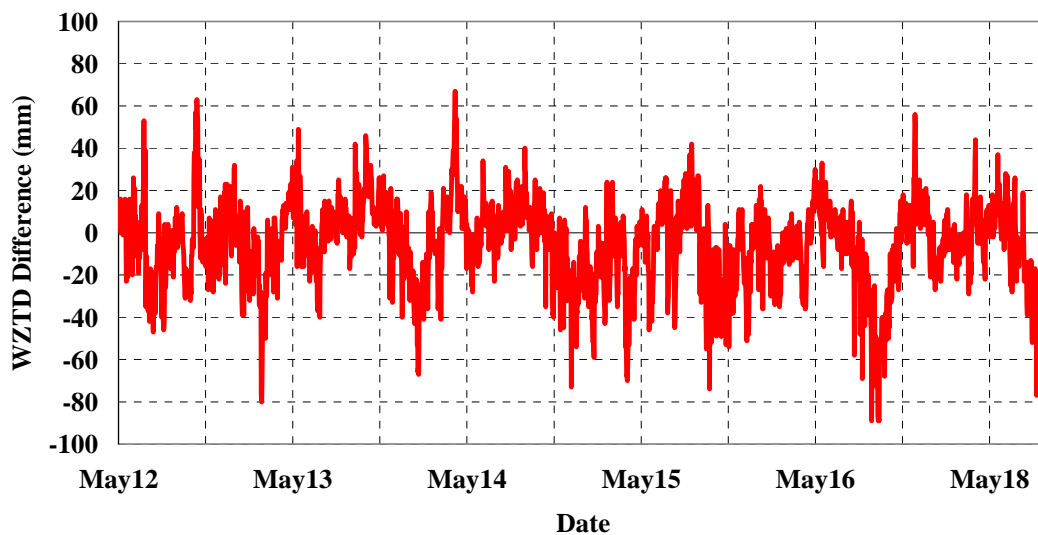
Figure 7.15 WZTD difference based on the PPP UofC model
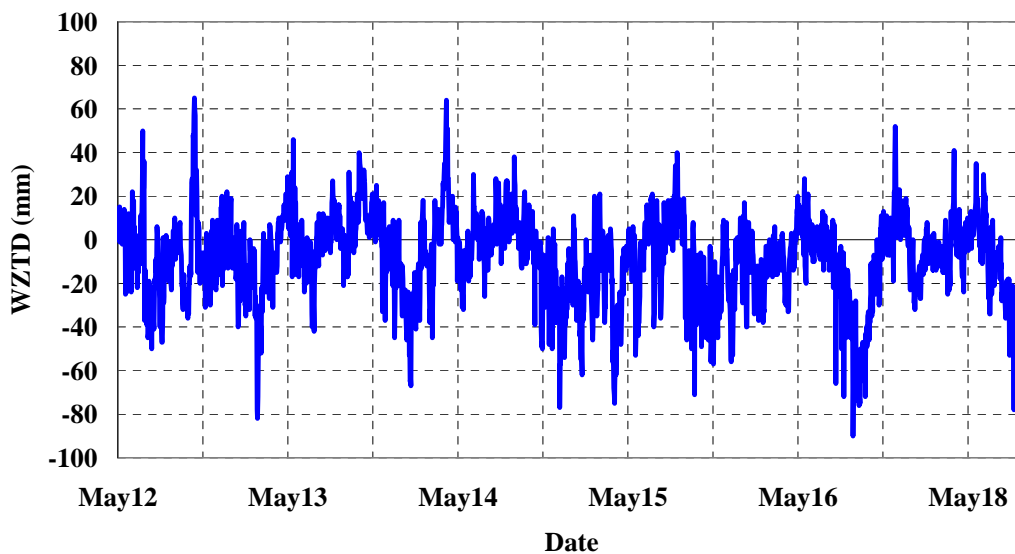
Figure 7.16 WZTD difference based on the PPP Traditional model
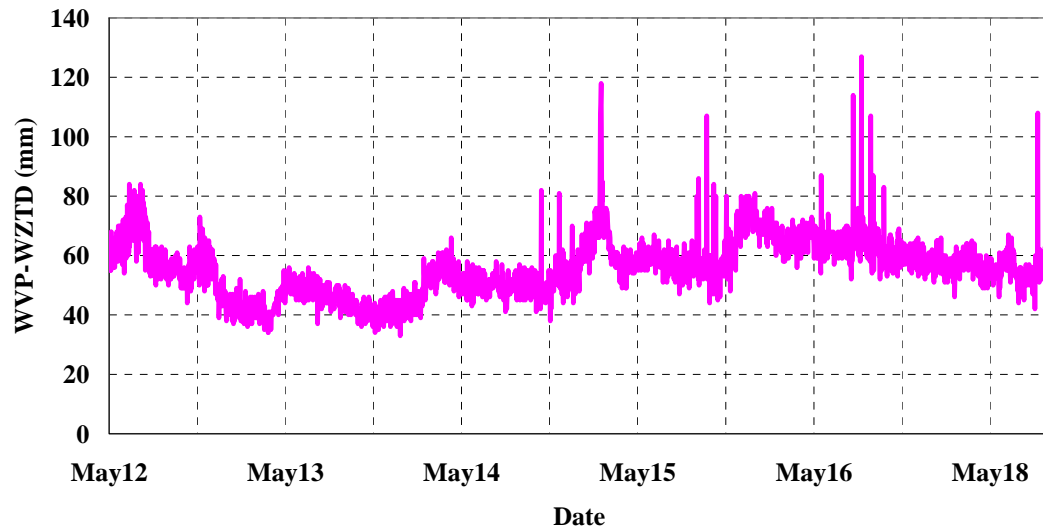
Figure 7.17 Used WVP zenith tropospheric delay

7.6 WZTD Modeling and Estimation

With the availability of surface meteorological parameters, the tropospheric dry component can be modeled with high confidence, but the wet component is more difficult to model. This section shows the comparison of the WZTD obtained from modeling and from the WVP. The Hopfield model is used for the wet tropospheric component as depicted previously in Equation 3.2.

The WVP data of May 12, 13, 14, 15, 16, and 18, 2004 is used in this section. Data from the surface meteorological data was obtained from the *MET3A* instrument that exits near the WVP.

The results of comparing the modeled and WVP wet zenith tropospheric delay are shown in Figure 7.18. The summary of statistics shows a bias of -9 mm and a standard deviation

of 8 mm. This agreement is promising, but it should be noted that it is related to the station height above sea level. This station is at a height of about one kilometer above sea level, which represents about 10% of the wet tropospheric layer.
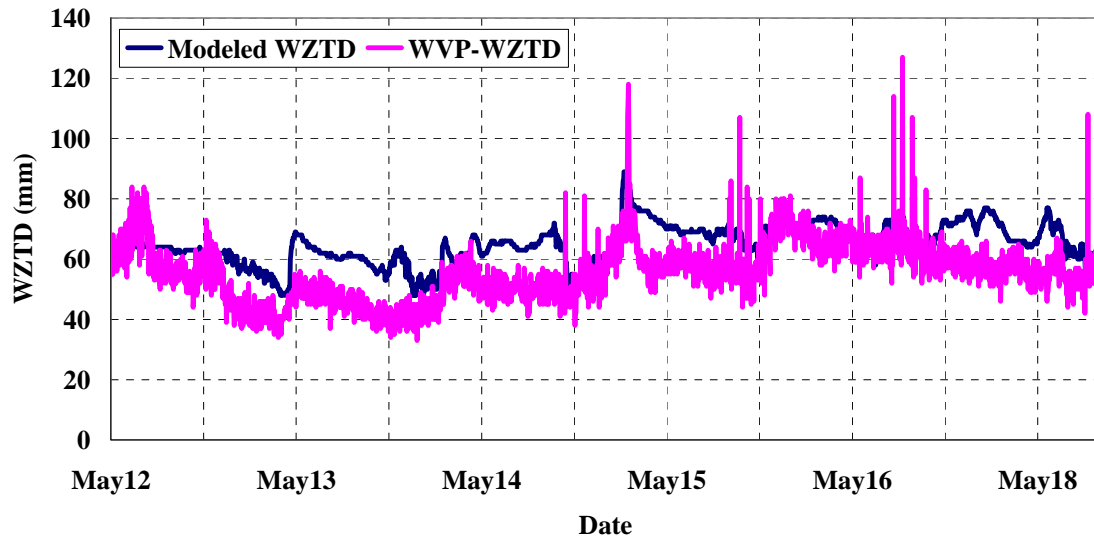
Figure 7.18 Modeled and WVP WZTD

In summary, the merits of PPP as a tool for troposphere estimation are that neither a position constraint, nor a meteorological sensor is necessary. Only when the wet component is sought, precise meteorological data is needed. Accordingly, it can be used as a mobile tool for troposphere monitoring.

7.7 Precise Ionospheric Delay Estimation Using Un-differenced Carrier Phase Observations

The long established way for estimating the absolute ionospheric delay or total electron content is to use a combination of dual frequency GPS pseudo-code observations. The accuracy of this method is usually in the order of 1-5 TEC due to code noise and multipath, where one TEC is equivalent to 14 and 27 cm on the L1 and L2 frequencies, respectively (Skone, 2001). To date, only a precise differential (not absolute) ionospheric delay can be obtained based on carrier phase observations. With the emergence of PPP technology, it is possible to estimate the absolute carrier phase ambiguities with high confidence. Consequently, it is feasible to calculate the absolute ionospheric delay directly with the use of carrier phase observations. In the following sections, the derivation of absolute ionospheric delay from pseudocode and carrier phase observations is presented along with their expected accuracies. The latter were obtained using the concept of error propagation.

7.7.1 Absolute Ionospheric Delay from Pseudocode Observations

Using pseudocode observations on L_1 and L_2, the absolute ionospheric delay can be estimated. An example of the delay on L_1 and L_2 are illustrated in Equations (7.4) and (7.5).

$$\frac{40.3}{f_1^2}TEC = \frac{f_2^2}{f_1^2 - f_2^2}(P_1 - P_2 - (1 - \frac{f_1^2}{f_2^2})cT_{GD,r} + (1 - \frac{f_1^2}{f_2^2})cT_{GD,s}) \qquad (7.4)$$

$$\frac{40.3}{f_2^2}TEC = \frac{f_1^2}{f_1^2 - f_2^2}(P_1 - P_2 - (1 - \frac{f_1^2}{f_2^2})cT_{GD,r} + (1 - \frac{f_1^2}{f_2^2})cT_{GD,s})$$ (7.5)

where

f_1 - frequency of L_1

f_2 - frequency of L_2

P_1 - pseudo range on L_1

P_2 - pseudo range on L_2

TEC - total electron content

c - speed of light

$T_{GD,r}$ - receiver inter-frequency bias

$T_{GD,s}$ - satellite inter-frequency bias

Special attention should be paid to the details associated with the consistency between the pseudocode on L1 and L2 as well as the inter-frequency bias. In the context of the ionospheric delay, the value of the inter-frequency bias reflects also all other hardware delays because they are inseparable as mentioned before. Accordingly, the words of inter-channel bias or DCBs can be used (Skone, 2001; Leick, 2004). The anticipated accuracy from this method is given in Equations (7.6) and (7.7).

$$\sigma^2_{Ionosphere\,Delay\,on\,L1} = (\frac{f_2^2}{f_1^2 - f_2^2})^2(\sigma^2_{P2} + \sigma^2_{P1} + ((1 - \frac{f_1^2}{f_2^2})c)^2\sigma^2_{T_{GD,r}} + ((1 - \frac{f_1^2}{f_2^2})c)^2\sigma^2_{T_{GD,s}})$$ (7.6)

$$\sigma^2_{Ionosphere\,Delay\,on\,L2} = (\frac{f_1^2}{f_1^2 - f_2^2})^2(\sigma^2_{P2} + \sigma^2_{P1} + ((1 - \frac{f_1^2}{f_2^2})c)^2\sigma^2_{T_{GD,r}} + ((1 - \frac{f_1^2}{f_2^2})c)^2\sigma^2_{T_{GD,s}})$$ (7.7)

where

σ^2_{P1} - variance of the pseudocode on L_1

σ^2_{P2} - variance of the pseudocode on L_2

$\sigma^2_{T_{GD,r}}$ - variance of receiver inter-frequency bias

$\sigma^2_{T_{GD,s}}$ - variance of satellite inter-frequency bias

$\sigma^2_{Ionosphere\,Delay\,on\,L1}$ - anticipated variance of the ionospheric delay on L_1

$\sigma^2_{Ionosphere\,Delay\,on\,L2}$ - anticipated variance of the ionospheric delay on L_2

Substituting for f_1=1575.42 MHz and f_2 = 1227.6 MHz in the equations above, a simplified form of the equations describing the accuracy of ionospheric delay can be expressed in Equations (7.8) and (7.9). The limiting factor for this method is the accuracy of the inter-frequency bias and the noise in the code observations.

$$\sigma^2_{IonoDelay\,on\,L1} = (1.54)^2(\sigma^2_{P1} + \sigma^2_{P2} + 0.64^2 \cdot c^2 \cdot \sigma^2_{T_{GD,r}} + 0.64^2 \cdot c^2 \cdot \sigma^2_{T_{GD,s}}) \qquad (7.8)$$

$$\sigma^2_{IonoDelay\,on\,L2} = (2.54)^2(\sigma^2_{P1} + \sigma^2_{P2} + 0.64^2 \cdot c^2 \cdot \sigma^2_{T_{GD,r}} + 0.64^2 \cdot c^2 \cdot \sigma^2_{T_{GD,s}}) \qquad (7.9)$$

7.7.2 Absolute Ionospheric Delay from Carrier Phase Observations

Carrier phase is the most precise GPS observation. The expression for obtaining the absolute ionospheric delay can be written as given in Equation (7.10).

$$\frac{40.3}{f_1^2}TEC = \frac{f_2^2}{f_1^2 - f_2^2}(\Phi_1 + N_1\lambda_1 - \Phi_2 - N_2\lambda_2 + (1-\frac{f_1^2}{f_2^2})cT'_{GD,r} - (1-\frac{f_1^2}{f_2^2})cT'_{GD,s}) \qquad (7.10)$$

where:

Φ_1 - phase measurements on L_1 (m)

Φ_2 - phase measurements on L_2 (m)

N_1 - ambiguity on L_1 (cycles)

λ_1 - L$_1$ wavelength (0.19m)

N_2 - ambiguity on L$_2$ (cycles)

λ_2 - L$_2$ wavelength (0.24m)

$T'_{GD,r}$ - receiver inter-frequency bias for carrier phase

$T'_{GD,s}$ - satellite inter-frequency bias for carrier phase

Similar to pseudo-code ionospheric delay estimation, the error propagation concept can be applied to obtain the expected accuracy as given in Equations (7.11) and (7.12).

$$\sigma^2_{CarrierIonoDelay\ on\ L1} = (1.54)^2(\sigma^2_{\Phi_1} + \lambda_1^2\sigma^2_{N_1} + \sigma^2_{\Phi_2} + \lambda_2^2\sigma^2_{N_2} + \\ 0.64^2 \cdot c^2 \cdot \sigma^2_{T'_{GD,r}} + 0.64^2 \cdot c^2 \cdot \sigma^2_{T'_{GD,s}})$$

(7.11)

$$\sigma^2_{CarrierIonoDelay\ on\ L2} = (2.54)^2(\sigma^2_{\Phi_1} + \lambda_1^2\sigma^2_{N_1} + \sigma^2_{\Phi_2} + \lambda_2^2\sigma^2_{N_2} + 0.64^2 \cdot c^2 \cdot \sigma^2_{T'_{GD,r}} + \\ 0.64^2 \cdot c^2 \cdot \sigma^2_{T'_{GD,s}})$$

(7.12)

where

$\sigma^2_{\Phi_1}$ - variance of the carrier phase observation on L$_1$ (m)

$\sigma^2_{\Phi_2}$ - variance of the carrier phase observation on L$_2$ (m)

$\sigma^2_{N_1}$ - variance of the carrier phase ambiguity on L$_1$ (cycles)

$\sigma^2_{N_2}$ - variance of the carrier phase ambiguity on L$_2$ (cycles)

$\sigma^2_{T'_{GD,r}}$ - accuracy of receiver inter-frequency bias,

$\sigma^2_{T'_{GD,s}}$ - variance of satellite inter-frequency bias,

$\sigma^2_{CarrierIonoDelay\ on\ L1}$ - anticipated variance of the ionospheric delay on L$_1$

$\sigma^2_{CarrierIonoDelay\ on\ L2}$ - anticipated variance of the ionospheric delay on L$_2$

There are three advantages of using carrier phase observations to estimate the ionospheric delay instead of pseudocode observations: the carrier phase observations are much more accurate, less noisy, and less vulnerable to the errors caused by multipath than pseudocode observations. However, there is one disadvantage of using carrier phase observations. The users need to wait for the convergence of the carrier phase ambiguities to get the best accuracy. Tables 7.4 and 7.5 list the anticipated accuracy of the absolute ionospheric delay obtained from pseudocode and carrier phase observations based on the concept of error propagation. They also illustrate the anticipated ionospheric delay accuracy with respect to different variance values of pseudorange observations and carrier phase ambiguities. These error propagation results are obtained based on the assumption that the accuracy of the inter-frequency bias is 0.03ns as reported normally in the JPL-IONEX file (JPL, 2004). In this section, the inter-frequency delays for code and carrier phase observation are assumed the same but with different signs. It is worth noting that this value is better than the inter-frequency bias day-to-day stability as reported by Hugentobler (2002). It is evident that with the use of high quality pseudocode observations, the ionospheric delay estimation is limited in the best case to about four decimeters on L1. In contrast, using the carrier phase method can produce higher accuracy estimates based on the converged ambiguities. If the accuracy of the converged ambiguities is a small fraction of one cycle, then the anticipated accuracy of the ionospheric delay can be significantly better than two decimeters, mainly because of the limitation imposed by the accuracy of the inter-frequency bias. The accuracy of the proposed ionospheric delay estimation method using un-differenced carrier phase is more

precise than the IGS ionosphere TEC product. The latter has accuracy of 2-8 TEC (IGS, 2004).

Table 7.4 Anticipated accuracy of code based ionospheric delay

σ_{P1} (cm)	σ_{P2} (cm)	$\sigma_{CodeIonoDe\ lay\ on\ L2}$ (cm)	$\sigma_{CodeIonoDe\ lay\ on\ L1}$ (cm)
10	10	36	21
20	20	71	43
30	30	107	65

Table 7.5 Anticipated accuracy of carrier phase based ionospheric delay

σ_{Φ_1} (mm)	σ_{Φ_2} (mm)	σ_{N_1} (cycles)	σ_{N_2} (cycles)	$\sigma_{CarrierIonoDelay\ on\ L2}$ (cm)	$\sigma_{CarrierIonoDelay\ on\ L1}$ (cm)
1	1	0.01	0.01	2	1
1	1	0.10	0.10	8	5
1	1	0.10	0.10	8	5
1	1	0.10	0.10	8	5
1	1	0.20	0.20	15	9
1	1	0.30	0.30	23	14
1	1	0.40	0.40	31	19

7.7.3 Comparison between Code and Carrier Phase Ionospheric Delay Estimates

This section presents the numerical results and analysis of ionospheric delay estimation from code and carrier phase observations, respectively. It focuses on the consistency of the two solutions, their behavior with respect to the satellite elevations, and their noise characteristics. The results presented here are based on GPS datasets obtained from IGS network stations WHIT and PIE1 on January 31, 2003. The data has a sampling interval

of 30 seconds and an elevation cutoff angle of 10 degrees. A static dataset processing scheme similar to the one given in Section 5.1 is used in this section. The ionospheric delay was calculated for the medium frequency f_1f_2. Figures 7.19 and 7.20 represent the ionospheric delay for two satellites at different times of the day. Figure 7.19, shows the ionospheric delay estimation for PRN 6 during its two visibility periods at the beginning of PPP processing and after the convergence. Here appears to be consistent between the ionospheric delay obtained from pseudocode and carrier phase observations. However, there is a notable bias between the two solutions at the start of processing. The ionospheric delay obtained from the carrier phase is less noisy compared with the code estimate, and it does not show any severe noise behavior at low elevations.
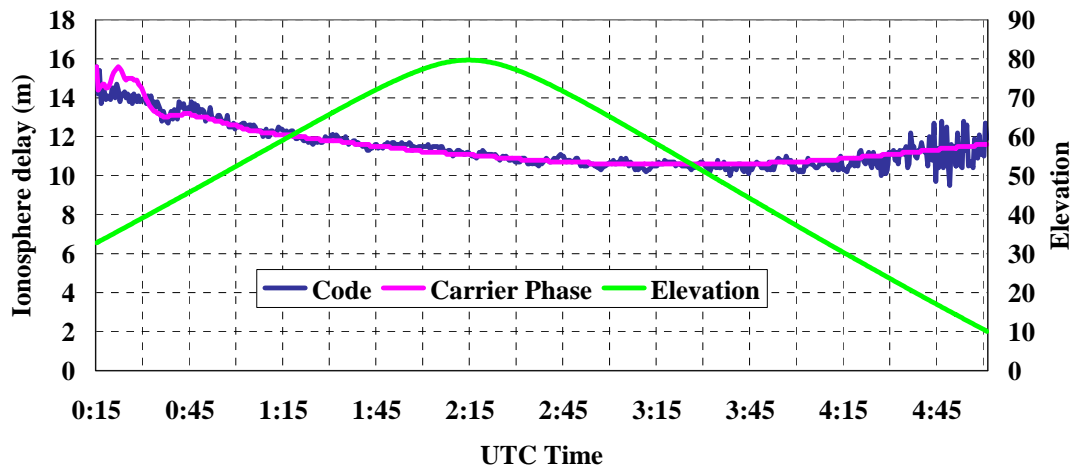
Figure 7.19 Ionospheric delay estimation for PRN 6 at WHIT station
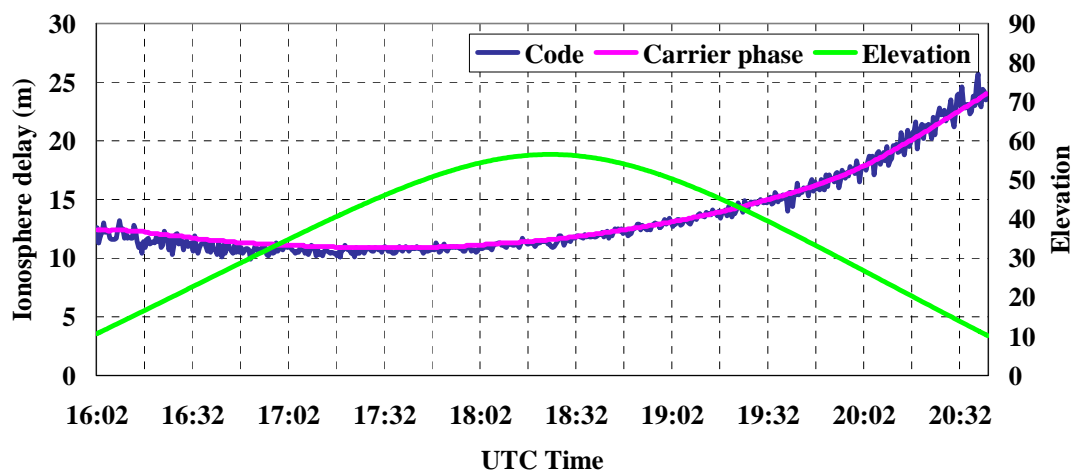
Figure 7.20 Ionospheric delay estimation for PRN 29 at WHIT station

Figures 7.21 and 7.22 show the ionospheric delay for the same satellites but for the PIE1 station. Results are comparable to those obtained from the WHIT station.
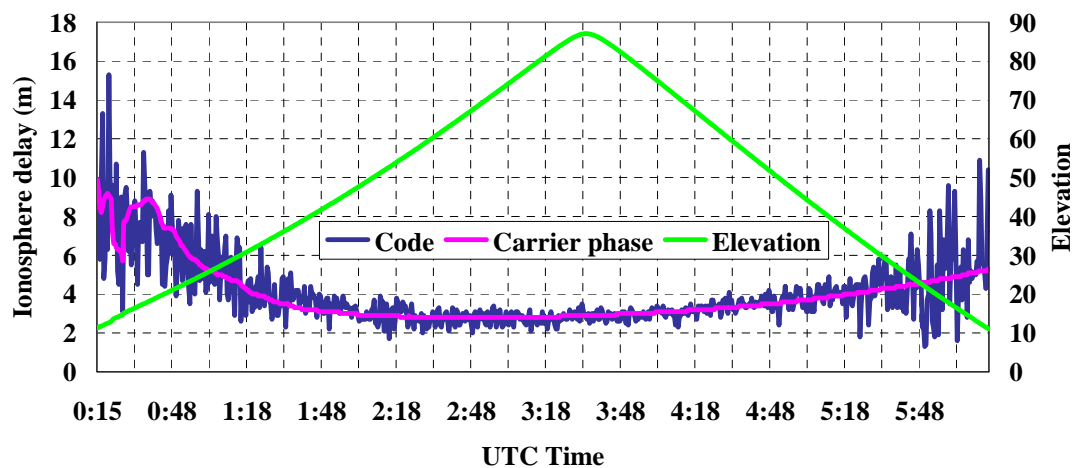
Figure 7.21 Ionospheric delay estimation for PRN 6 at PIE1 station
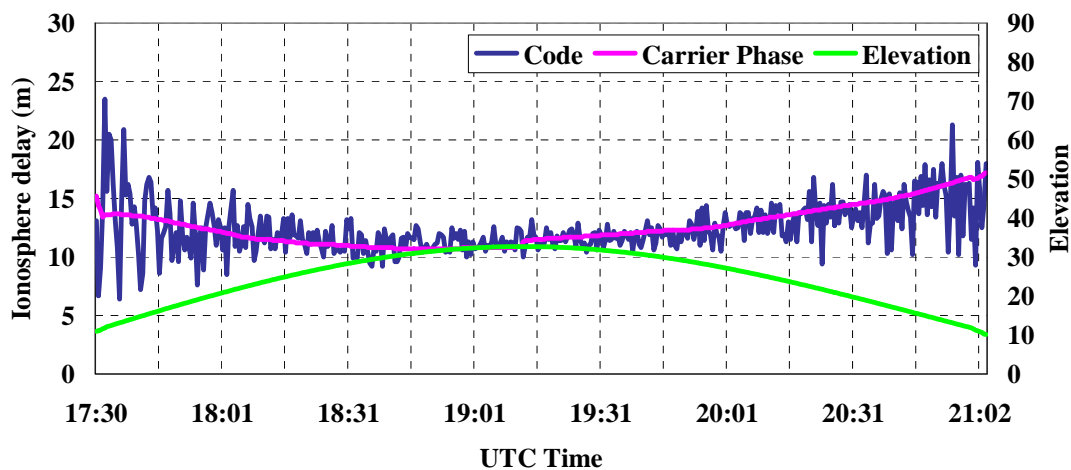
Figure 7.22 Ionospheric delay estimation for PRN 29 at PIE1 station

For several satellites, the WHIT station ionospheric delay shows a bias between the code

and carrier phase solutions, as shown in Figure 7.23.
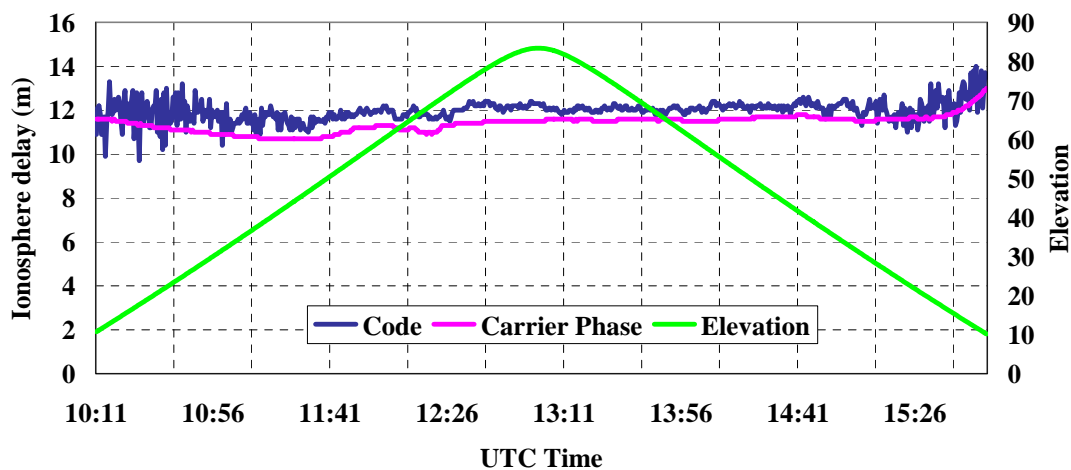
Figure 7.23 Ionospheric delay estimation for PRN 1 at WHIT station

The ionospheric delay bias for these satellites cannot be attributed to any difference in the

inter-frequency offset between pseudocode and carrier phase because the same satellites

at the PIE1 station do not show this bias (Figure 7.24).
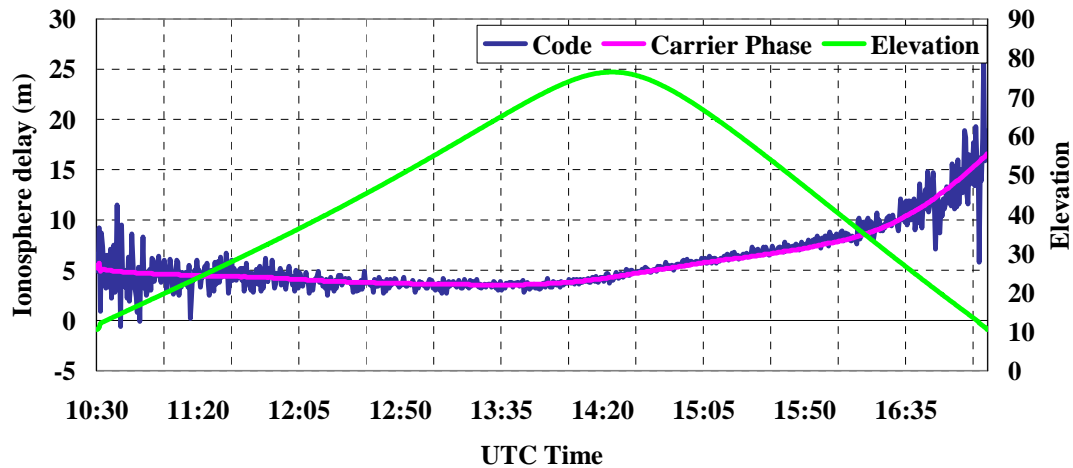
Figure 7.24 Ionospheric delay estimation for PRN 1 at PIE1 station

It is more likely that this bias is caused by the ambiguities of the satellites. It is possible that the ambiguities corresponding to these satellites have absorbed most of the error caused by precise orbit and clock interpolation. The two solutions for all the satellites at the WHIT station have a bias of 12 cm and a standard deviation of 59 cm, whereas the bias and standard deviation values for the PIE1 station are 2 cm and 134 cm, respectively. The large standard deviation between the ionospheric delay obtained from the code and carrier phase can be attributed to the noise in the code observations.

In summary, the proposed carrier phase based absolute ionospheric delay has low noise and high accuracy. The agreement between ionospheric delay obtained from the pseudocode and carrier phase methods suggests the reliability of the ionospheric delay obtained from the carrier phase method and the conformity of the inter-frequency bias for the code and carrier phase observations, which was highlighted in the Chapter 6.

7.8 Summary

This chapter illustrates the use of GPS as a tool for atmosphere sensing. The merits of using GPS are the mobility and the cheap cost. The chapter presented the accuracy of tropospheric delay estimated from PPP with respect to the IGS and WVP. Also, the chapter presented a new method for ionospheric delay estimation.

CHAPTER 8

SUMMARY, CONCLUSIONS, AND RECOMMENDATIONS

8.1 Summary

The development, analysis, and investigation of Precise Point Positioning using un-differenced code and carrier phase observations in addition to precise orbit and clock data were the major goals of this study. These goals were met. The existence of such a system eliminates the need for base stations and provides competitive accuracy to the current GPS positioning system. The development was necessary as this system is only available for large organizations such as JPL and NRcan. The analysis and investigations done in this research have contributed toward a better understanding of several ambiguous areas in the PPP's field.

The specific contributions of this research can be summarized as follows:

- Development of Precise Point Positioning algorithms that use IGS products

- Comprehensive analysis of PPP functional and stochastic models

- Analysis of the nature of non-zero initial phase and its relationship to ambiguity resolution in the case of un-differenced observations

- Comprehensive study for the PPP convergence and its relation with clock and troposphere modeling instead of estimation

- Development of a hybrid solution that can reduce the convergence in certain cases

- Ascertainment of the equivalence of inter-frequency bias for code and carrier phase in magnitude but with different signs.

- Verification the equivalence of ambiguity re-parameterization in traditional and UofC models through numerical results

- Development of a new method for absolute ionospheric delay estimation from carrier phase observations

- Development of a scheme for PPP's tropospheric delay estimate and validation

These contributions have been supported by numerical results, and the system has been tested under several conditions.

8.2 Conclusions

Based on the research and analysis carried out in the course of this thesis, the following findings can be drawn.

8.2.1 Accuracy

PPP is capable of achieving centimeter positioning accuracy level in the case of static positioning when using IGS final orbit and clock products. This absolute accuracy is both seamless and highly repeatable, independent of the station location. The static results obtained from PPP showed centimeter positioning accuracy. Kinematic positioning accuracy cannot be assessed absolutely; the only solution is to compare the PPP positioning solution with commercial software that performs GPS double difference. Therefore, all the kinematics positioning accuracy presented here is with respect to the double difference solution accuracy. The kinematics positioning results that are obtained based on the use of IGS final orbit and clock corrections at intervals of 15 and 5 minutes showed positioning accuracy better than 3 decimeters for many cases of kinematic behavior that include land vehicle, marine and airborne GPS dataset. With the availability of 30 second satellite clock corrections, this level of error can be greatly reduced.

8.2.2 Performance

Like any system estimating ambiguities as float values, PPP needs time to converge to cm positioning accuracy. Therefore, this study has analyzed and investigated the concept

of ambiguity resolution in the case of un-differenced observations. It has been concluded that the ambiguity resolution in the case of PPP is highly unlikely to be applicable because of the nature of the ambiguities. The research has also concluded that the satellite clock corrections cannot represent the non-zero initial phase. The thesis has investigated the effect of satellite clock correction intervals on the convergence and positioning. It has been concluded that it has a potential effect on both convergence and accuracy. Moreover, the research has developed and investigated a hybrid solution that can be used to enhance the positioning results at the beginning of processing. This hybrid solution and its limitations have been presented and highlighted. The research also concluded that modeling the tropospheric delay at the beginning of the processing is highly unlikely to enhance the positioning accuracy significantly.

8.2.3 Ionosphere

A new approach for estimating a precise absolute ionospheric delay has been developed and demonstrated high accuracy and low noise compared with the available technique. This approach has never been used before.

8.2.4 Troposphere

The thesis presented a method for absolute tropospheric delay based on PPP. Estimation and evaluation of the PPP's tropospheric delay were investigated. The evaluation of this tropospheric delay was done with respect to accurate IGS delay and WVR data.

8.2.5 Ambiguity Re-parameterization and the Inter-frequency Delay

The research dealt with unconventional issues such as the ambiguity re-parameterization and the inter-frequency delay on code and carrier phase observations. It has been concluded that the ambiguity estimates in the two PPP functional models are equivalent. Based on the results of the ambiguity re-parameterization and the carrier phase ionospheric delay, it has been concluded that the inter-frequency delays for code and carrier phase are likely to be the same in value but with different signs. Accordingly, the effect of this delay is likely to be canceled in the UofC model. The thesis research work addressed another possibility for the equivalence of this ambiguity re-parameterization which could be the absorption of the inter-frequency delay in the estimated ambiguities of the PPP UofC model and the fading of the values of the inter-frequency delay when constructing the ambiguities of the PPP traditional model.

8.3 Recommendations

Further to this research, many points can be suggested. Among these are the following:

- With the emergence of realtime precise orbit and clock corrections from several organizations such as NRcan and JPL, the PPP should move to the real time mode.

- To integrate the DARTS method and PPP to allow backing the PPP in case of unavailability of precise data

- To investigate the possibility of modeling GPS orbit and estimating satellite clock corrections between epochs. This can be helpful in the case of using precise data with large intervals or in the case of suffering from a precise data gap. The suggestion above will benefit from using only one starting point for the precise orbit and clock.

- To investigate neutrally the kinematics accuracy of PPP with respect to other positioning techniques that do not use IGS orbit and clock data.

- With the availability of the precise GLONASS orbit and with the recent Russian support, it would be important to incorporate GLONASS signals in the PPP system.

- To investigate the effect of GPS signal modernization and the emergence of Galileo system on PPP. This can be done by analyzing the possible signal combinations, which will be available in the near future.

References

Abdel-salam, M. (2005). Natural Disasters Inference from GPS Observations: Case of Earthquakes and Tsunamis. *Proceedings of ION GPS-2005*, Long Beach, California (Accepted).

Abdel-salam, M. (2004). A Hybrid Solution to Reduce the Long Convergence Time in Precise Point Positioning. *Proceedings of ION GPS-2004*, Long Beach, California

Abdel-salam, M. and Y. Gao (2004). Precise GPS Atmosphere Sensing Based on Un-Differenced Observations. *Proceedings of ION GPS-2004*, Long Beach, California.

Abdel-salam, M. and Y. Gao (2003). Ambiguity Resolution in Precise Point Positioning: Preliminary Results. *Proceedings of ION GPS-2003*, Oregon, Portland

Abdel-salam, M., Y. Gao, and X. Shen (2002). Analyzing the Performance Characteristics of a Precise Point Positioning System. *Proceedings of ION GPS-2002*, Oregon, Portland

Klobuchar, A. (1996). Ionosphere Effects on GPS, in *Global Positioning System:* in *Global Positioning System: Theory and Applications*, Progress in Astronautics and Aeronautics, Vol 1, Chapter 12. Eds. B.W. Parkinson, J.J. Spilker Jr, American Institute of Aeronautics and Astronautics, Inc., V, Washington, D.C., U.S.A.

Abousalem, M. (1996). *Development And Analysis Of Wide Area Differential GPS Algorithms*, PhD dissertation, The Department of Geomatics Engineering. The University of Calgary, Alberta, Canada.

Afraimovich, E. L., E. A. Kosogorov, L.A. Leonovich, and O.M. Pirog (1998). Global Pattern of Large-Scale Ionospheric Disturbances during the Magentic Storm of September 25, 1998, as Inferred from GPS Network Data. *Earth, Planets, and Space*, V52, N10, 669-673.

Ashby, N. and J. J. Spilker Jr. (1996). Introduction to Relativistic Effects on The Global Positioning System, *in Global Positioning System: Theory and Applications, Progress in Astronautics and Aeronautics*, Vol. 2, Chapter 18, Eds. B.W. Parkinson, J. J. Spilker Jr, Volume 164, American Institute of Aeronautics and Astronautics, Inc., V, Washington, D.C., U.S.A.

Axelrad, P. and R.G. Brown (1996). GPS Navigation Algorithms. In *Global Positioning System: Theory and Applications*, Progress in Astronautics and Aeronautics ,Volume 1, Chapter 9. Eds. B.W. Parkinson, J.J. Spilker. Volume 164, American Institute of Aeronautics and Astronautics, Inc., V, Washington, D.C., U.S.A.

Bar-Sever, Y. E. (1998). Estimation of The GPS Transmit Antenna Phase Center Offset, AGU spring meeting, *EOS transactions,* 79(45):18.

Bisnath, S. and Langley R. (2001). High–Precision Platform Positioning with a Single GPS Receiver. *Proceedings of ION GPS-2001*, Salt Lake City, UT.

Bisnath, S., D. Wells, D. Dodd (2003). Evaluation of Commercial Carrier-Phase-Based WADGPS Services for Marine Applications. *Proceedings of ION GPS-2003*, Oregon, Portland.

Bona, P. (2000). Precision, Cross Correlation, and Time Correlation of GPS Phase and Code Observations. *GPS Solutions*, 4(2), 3-13.

Bona, P. (2000a). Accuracy of GPS phase and Code Observations in Practice. *Acta Geod. Geoph*. Hung., 35(4), 433-451.

Brown, R. G. and P. Y.C. Hwang (1997*). Introduction to Random Signals and Applied Kalman Filtering* (Third Edition). John Wiley & Sons, Inc. ISBN 0-471-1283-9-2.

Bruton, A. M., M. Kern, K.P. Schwarz, S. Ferguson, A. Simsky, K. Tennant and M. Wei, J. Halpenny, R. Langley, T. Beran, K. keller, P. Mrstik, K. Kusevic and R. Faulkner (2001). On the Accuracy of Kinematic Carrier Phase DGPS for Airborne Mapping. *GEOMATICA*, vol. 55 No. 4, pp. 491 to 507.

Collins, P., F. Lahaye, F. J. Kouba and P. Heroux (2001). Real-Time WADGPS Corrections from Un-differenced Carrier Phase. *ION NTM 2001*, Long Beach, CA, 22-24 January, 2001.

Collins, P., and R. B. Langley (1999). *Possible Weighting Schemes for GPS Carrier Phase Observations in the Presence of Multipath*. Contract report DAAH04-96-C-0086/TCN 98151, for United States Army Corps of Engineers Topographic Engineering Center.

Craymer, M., R. Ferland, and R. Snay (1999). Realization and Unification of NAD83 in Canada and the USA via the ITRF. *Proceeding of the International Symposium of the International Association of Geodesy, Section II, "Toward an Integrated Geodetic Observing System (IGGOS)"* Munich, October 5-9.

EL-Rabbany, A. (1994). *The Effect of Physical Correlations of the Ambiguity Resolution and Accuracy Estimation in GPS Differential Positioning*. PhD thesis, The University of New Brunswick Fredericton, NB, Technical Report 170.

FAA, (2004). URL http://gps.faa.gov/gpsbasics/controlsegment.htm. Date accessed: August, 2004

Fortes, L.B.S. (2002). *Optimizing the Use of GPS Multi Reference Stations for Kinematic Positioning*. PhD Thesis, Department of Geomatics Engineering, University of Calgary, Canada.

Gabor, J. (2000). Characteristics of Satellite-Satellite Single Difference Widelane Fractional Carrier Phase Biases. *Proceedings of ION GPS 2000*, 19-22 September, 2001.

Gao, Y. and X. Shen (2001). Improving Ambiguity Convergence in Carrier Phase-Based Precise Point Positioning. *Proceedings of ION GPS 2001*, Salt Lake City, UT.

Gelb, A., Ed. (1979). *Applied Optimal Estimation*. The MIT press.

Goad C., (1996). Surveying with the Global Positioning System, in *Global Positioning System: Theory and Applications*, Progress in Astronautics and Aeronautics, Vol

1, Chapter 18, Eds. B.W. Parkinson, J. J. Spilker Jr, American Institute of Aeronautics and Astronautics, Inc., V, Washington, D.C., U.S.A.

Grewal, M. S. and A. P. Andrews (1993). *Kalman Filtering, Theory and Practice*. Prentice Hall, Upper Saddle River, New Jersey.

Grewal, M. S., R. L. Weill, and A. P. Andrews (2001). *Global Positioning Systems, Inertial Navigation and Integration*. John Wiley & Sons, Inc.

Gunter, S. (2000). Real Time Satellite Positioning in Centimeter Level in the 21 Century Using Permanent Reference Stations. *Nordic Geodetic Summer School*, Fevik, Norway.

Han S. C., J.H. Kwon, C. Jekeli (2001). Accurate Absolute GPS Positioning Satellite Clock Error Estimation. *Journal of Geodesy* 75, pp. 33-43.

Hofmann-Wellenhof, B., H. Lichtenegger, J. Collins (2001). *GPS Theory and Practice* Fifth revised edition, Springer-Verlag Wien New York, ISBN 3-211-83534-2.

Horvath, T. (2002). *Performance Comparison of Wide Area Differential GPS Systems*. Diploma thesis, Budapest University of Technology and Economics, Department of Geodesy and Geomatics Engineering Technical Report No212, University of New Brunswick, Fredericton, New Brunswick, Canada.

Huber S., K. Kaniuth (2003). On the Weighting of GPS Phase Observations in the EUREF Network Processing. *EUREF Symposium*, Toledo, Spain, June 4-7, 2003.

Hugentobler, U., S. Schaer, G. Beutler, H. Bock, R. Dach, A. Jaggi, M. Meindl, C. Urschl, L. Mervart, and M. Rothacher, U. Wild, A. Wiget, E. Brockmann, D. Ineichen, G. Weber, H. Habrich, and C. Boucher (2002). *CODE IGS Analysis Center Technical Report 2002.*

ICD-GPS-200 (2000). ARINC Research Corporation. CA, USA. Date accessed: April, 2004.

IGDG (2004). Internet-based Global Differential GPS. JPL, NASA. Date accessed: May, 2004.

IGS (2004a). 2001-2002 Annual Report. Pasadena, CA: Jet Propulsion Laboratory.

IGS, (2004b). ftp://cddisa.gsfc.nasa.gov/pub/gps/products/trop. Date accessed: January, 2004

IGS (2004c). http://igscb.jpl.nasa.gov/components/prods.html. Date accessed: December, 2004.

IGS Mail #4913 (2004). CODE High Rate Clocks
http://igscb.jpl.nasa.gov/mail/igsmail/2004/msg00136.html. Date accessed: December, 2004.

IGS Mail #5078 (2004). P1C1
Biasftp://igscb.jpl.nasa.gov/igscb/software/cc2noncc/p1c1bias.hist, 2005. Date accessed: January, 2005.

Jensen A. B. O., C. C. Tscherning, F. Madsen (2002). Integrating Numerical Weather Predictions in GPS Positioning. *ENC GNSS-2002*. Copenhagen, May, 2002.

Jin, X.X. and dC. D.e Jong, (1996). Relationship between Satellite Elevation and Precision of GPS code Observations. *The Journal of Navigation*, vol. 49 pp. 253-265.

Jin, S. and J. Wang, (2004), Impact of Stochastic Modeling on GPS-Derived ZTD estimations. *Proceedings of ION GPS-2004*, Long Beach, California.

JPL, (2004), IONOX, ftp://cddisa.gsfc.nasa.gov/pub/gps/products/ionex/. Date accessed February, 2004.

Kechine, M.O., C.C.J.M. Tiberius, H. van der Marel (2003). Experimental Verification of Internet-Based Global Differential GPS. *Proceedings of ION GPS 2003*, Portland, Oregon, 24-27 September.

Kouba, J. and P. Heroux (2000). GPS Precise Point Positioning Using IGS Orbit Products. *GPS Solutions*, Vol. 5, No. 2.

Kouba J., J. Popelár (1994). Modern Geodetic Reference Frames for Precise Satellite Positioning and Navigation. *Proceedings of the International Symposium on Kinematic Systems in Geodesy, Geomatics & Navigation (KIS94),* Banff, Canada.

Leick, A. (2004). *GPS Satellite Surveying*, 3rd Edition. Wiley, ISBN: 0-471-05930-7.

Lochhead K., A. Kassam, R. Hare, and L. LeBlanc (2002). CDGPS – Canada-wide DGPS Service: Quality Real Time GPS Positioning. *The Canadian Hydrographic Conference*, Toronto, ON, Canada, May 28-31, 2002.

Liu, X. (2002). A Comparison of Stochastic Models for GPS Single Differential Kinematics Positioning. *ION GPS 2002*, Portland, Oregon, September 24-27, 2002.

Lundberg J.B. and A. G. Evans (2001). The Effect of GPS Orbit Solution Strategies on Absolute Point Positioning. *Proceedings of ION GPS 2001*, Salt Lake City, UT, 11-14 September.

McCarthy, D.D., editor (1996). IERS Conventions (1996). IERS Technical Note 21.

Mader, G. L. (2001). A Comparison of Absolute and Relative GPS Antenna Calibrations. *GPS Solutions*, Vol. 4, No 4, John Wiley & Sons, Inc, 2001 pp. 37-40.

Mader, G. L. (2001a). Calibrating the L1 and L2 Phase Centers of a Block IIA Antenna. *Proceedings ION GPS 2001*, Salt Lake City, UT, 2001.

Mader, G. L. (1999). GPS Antenna Calibration at The National Geodetic Survey. *GPS Solutions*, Vol. 3, No1, John Wiley & Sons, Inc, 2001 pp. 50-58

Mendes, V.B. and R.B. Langley (1994). A Comprehensive Analysis of Mapping Functions Used in Modeling Tropospheric Propagation Delay in Space Geodetic Data. *KIS94, Proceedings of the International Symposium on Kinematic Systems*

in Geodesy, Geomatics and Navigation, Banff, Alberta, 30 August - 2 September 1994, pp. 87-98.

Mendes, B. (1999). *Modeling the Neutral-Atmosphere Propagation Delay in Radiometric Space Techniques*, PhD Dissertation. Dept. of Geodesy and Geodetic Engineering, TR 199 University of New Brunswick, Federicton, NB, Canada, ISBN: 0970954409.

Merrigan, M. J., E. R. Swift, R. F. Wong, and J. T. Saffel (2002). A Refinement to the World Geodetic System 1984 Reference Frame. *Proceedings of ION GPS 2002*, Portland, OR, 24-27 September.

Mikhail, E. M., F. Ackermann, (1976). Observation and Least Square, IEP-A Dun-Donnelley Publisher, New York.

Misra, P. and P. Enge (2001). *Global Positioning System: Signals, Measurements and Performance*. Ganga-Jumuna Press.

Muellerchoen R., W. Bertiger and M. Lough (2000). Results of an Internet-Based Dual–Frequency Global Differential GP System. *Proceedings of the IAIN World Congress in association with the U.S. ION Annual Meeting*, 2000.

Muellerchoen R., A. Reichert, Da kuang, M. Heflin, W. Beriger, and Y. Bar-Sever (2001). Orbit Determination with NASA's High Accuracy Real-Time Global Differential GPS System. *Proceedings of ION GPS 2001*, Salt Lake City, UT11-14 September.

NGA (2004). National Geospatial-intelligence Agency. URL: http://earth-info.nga.mil/GandG/sathtml/gpsdoc2004_11a.html. Date accessed: January, 2005.

Neilan, R. E., A. Moore, T. Springer, J. Kouba, J. Ray, and C. Reigber (2000). International GPS Service Life without SA. *Proceedings of the Institute of Navigation GPS 2000 Conference*, Sept. 2000 pp. 438-446.

Neumann, J. B., K. J. VanDierendonck, Allan Manz, and Thomas J. Ford (1999). *Real-Time Carrier Phase Positioning Using the RTCM Standard Message Types 20/21 and18/19*.

Niell, A. E., Coster, A. J., Solheim, F. S., Mendes, V. B., Toor, P. C., Langley, R. B., and Upham, C. A.: Comparison of measurements of atmospheric wet delay by radionsonde, water vapor radiometer, GPS, and VLBI. *Journal of Atmospheric and Oceanic Technology*, 18(6), 830-850, 2001.

Ovstedal O., E. Arne, Ofstad, K. Haustveit, and O. Kristiansen (2002). An Empirical Comparison between Absolute Satellite Positioning Methods and Differential Methods in Maritime Environment. *Proceedings of the ION GPS 2002*, Portland, Oregon 24-27 September.

Parkinson B.W. (1996). Introduction to Heritage of NAVSTAR. In *Global Positioning System: Theory and Applications*, Progress in Astronautics and Aeronautics ,Volume 1, Chapter 1, Eds. B.W. Parkinson, J.J. Spilker Jr, American Institute of Aeronautics and Astronautics, Inc., V, Washington, D.C., U.S.A.

Rabbel, W. and H. Schuh (1986). The Influence of Atmosphere Loading on VLBI-experiments. *J. Geophys*, 59, 164-170.

Radiometrics Corporation (2004). URL http://www.radiometrics.com/Radiometric_Profiling.pdf. Date accessed April, 2004.

Raquet, J. F. (2001). GPS Receiver Design. ENGO 699.64, Department of Geomatics Engineering, the University of Calgary.

Ray, J. K. (2005). *Personal communication*.

Ray, J. and K. Senior (2005). Geodetic techniques for time and frequency comparisons using GPS phase and code measurements. *Metrologia.*

Ray, J. K., M.E. Cannon and P. Fenton (2001a). Mitigation of Carrier Phase Multipath Effects Using Multiple Closely-Spaced Antennas. *Navigation*, Vol. 46, No. 4, pp. 193-201.

Ray, J. K., M.E. Cannon and P. Fenton (2001). Code and Carrier Multipath Mitigation Using a Multi-Antenna System. *IEEE Transactions on Aerospace and Electronic Systems*, Vol. 37, No.1, pp.183-195.

Rizos, C. (2002). Network RTK Research and Implementation: A Geodetic Perspective. *J. GPS*, 1(2), 144-150.

Rothacher, M. and G. Beutler (2002). *Advanced Aspects of Satellite Positioning*. Lecture notes for ENGO 609.90, The University of Calgary, AB, Canada.

Roulston, A., N. Talbot and K. Zhang (2000). An Evaluation of Various GPS Satellite Ephemeredes. *Proceedings of ION GPS 2000*, Salt Lake City, UT. 19-22 September.

Sandhoo, M, D. Turner and M. Shaw (2000). Modernization of the Global Positioning System. *Proceeding ION GPS 2000* Salt Lake City, September 19-22.

Scherneck, H. G. (1991). A Parameterized Solid Earth Tide Model and Ocean Tide Loading Effects for Global Geodetic Baseline Measurements. *Geoph. J. Int*. 106, pp, 677-694.

Schmitz M., G. Wubbena, and G. Boettcher (2002). Test of Phase Center Variations of Various GPS Antennas and Some Results. *GPS Solution* 6 (1, 2), pp. 18-27.

Schupler, B. R., and T.A. Clark (2001). Characterizing the Behavior of Geodetic GPS Antennas. *GPS World* 12(2), pp. 48-52.

Simsky A. (2003). Standalone Real-Time Positioning Algorithm Based on Dynamic Ambiguities (DARTS). *Proceedings of the ION GPS 2003*, Portland, Oregon, September 9-12, 2003.

SINEX_TROPO, (2004), ftp://epncb.oma.be/pub/general/sinex_tropo.txt. Date accessed: January, 2004.

Skone, S., (2005), *personal communication*.

Skone, S. (2001).The Impact of Magnetic Storms on GPS Receiver Performance. *Journal of Geodesy* 75:457-468, Springer-Verlag, 2001.

Skone, S. (2000). GPS Receiver Tracking Performance under Ionospheric Scintillation Conditions. *IGS Network Workshop 2000*, Soria Moria, Oslo, Norway 12-14 July, 2000.

Springer, T. (2000). Common interests of the IGS and the IVS. *Proceedings IVS general meeting,* Kotzting, Germany.

Soler, T. and J. Marshall (2003). A Note on Frame Transformations with Applications to Geodetic Datums. *GPS Solutions*, 7(1), 23-32.

Soler, T. and R.A. Snay (2004). Transforming Positions and Velocities between the International Terrestrial Reference Frame of 2000 and North American Datum of 1983. *J. Surv. Eng.*, ASCE, 130 (2) 49-55.

Soler, T., N. D. Weston, and H. Han (2002). Computing NAD 83 coordinates using ITRF-derived vector components*. Proc. XXII FIG International Congress, ACSM/ASPR Annual Conference*, Washington D.C. April 19-26.

Teunissen, P. J. G. and A. Kleusberg (Eds.) (1998). *GPS for Geodesy*, Second Edition, Springer-Verlag, 1998.

Teunissen, P. J. G. and M. A. Salzmann. (1988) Performance Analysis of Kalman Filters, Reports 88.2, Delft University of Technology, The Faculty of Geodesy, Mathematical and Physical Geodesy, Netherlands.

Tiberius, C. C. J. M. (1999). The GPS Data Weight Matrix: What Are the Issues? *National Technical Meeting Proceedings*, San Diego, California, January 25-27.

TrackLog (2004) URL http://www.tracklogs.co.uk/cgi-bin/publ/user.cgi?obj=home&page=gpsfaq&id=2040. Date accessed: February, 2004.

USNO (2004). GPS Operational Satellites (BLOCK II/IIA/IIR). ftp://tycho.usno.navy.mil/pub/gps/gpsb2.txt. Date accessed: January, 2005.

Vermeer, M. 1997. The Precision of Geodetic GPS and One Way of Improving It, *Journal of Geodesy*, 71, 240-245, Springer-Verlag.

Witchayangkoon, B. (2000). *Elements of GPS Precise Point Positioning.* PhD Thesis, the University of Maine.

Wu, J.T., S, C. Wu, G.A. Hajj, W.I. Bertiger, and S.M. Lichten (1993). Effects of Antenna Orientation on GPS Carrier Phase. *Man. Geodetica* 18, pp. 91-98.

Zhu, S. Y., F. H. Massmann, Y. Yu, and Ch. Reigber (2002). Satellite Antenna Phase Center Offset and Scale Errors in GPS Solutions. *Journal of Geodesy* 76:668-672, Springer-Verlag, September 11-14, 2003.

Zumberge J., F. H. Webb, and Y. Bar-Sever (2001). Precise Post Processing of GPS Data Products and Services from JPL. *ION NTM 2001*, Long Beach, CA, 22-24 January.

Zumberge, J. F., M. B. Heflin, D. C. Jefferson, M.M. Watkins, and F.H. Webb (1997). Precise Point Positioning for the Efficient and Robust Analysis of GPS Data from Large Networks. *Journal of Geophysical research*, Vol. 102, No. B3 Pages 5005-5017.

Zumberge, J. F., M.M. Watkins, and F.H. Webb (1998). Characteristics and Applications of Precise GPS clock Solutions Every 30 seconds. *Journal of Navigation*, 44 (4), 449-456, 1998.

Zumberge, J. F., R. Liu, and R. E. Neilan, eds. (1995). 1994 *IGS Annual Report*.

Appendix A

Niell's Mapping Function Coefficients (Leick, 2004)

Dry Mapping Function Coefficients

φ	$\tilde{a} \cdot 10^3$	$\tilde{b} \cdot 10^3$	$\tilde{c} \cdot 10^3$	$a_p \cdot 10^3$	$b_p \cdot 10^5$	$c_p \cdot 10^5$	$a_h \cdot 10^5$	$b_h \cdot 10^5$	$c_h \cdot 10^3$
15	1.2769934	2.9153695	62.610505	0	0	0			
30	1.2683230	2.9152299	62.837393	1.2709626	2.1414979	9.0128400			
45	1.2465397	2.9288445	63.721774	2.6523662	3.0160779	4.3497037	2.53	5.49	1.14
60	1.2196049	2.9022565	63.824265	3.4000452	7.2562722	84.795348			
75	1.2045996	2.9024912	64.258455	4.1202191	11.723375	170.37206			

Wet Mapping Function Coefficients

φ	$a \cdot 10^4$	$b \cdot 10^3$	$c \cdot 10^2$
15	5.8021897	1.4275268	4.3472961
30	5.6794847	1.5138625	4.6729510
45	5.8118019	1.4572752	4.3908931
60	5.9727542	1.5007428	4.4626982
75	6.1641693	1.7599082	5.4736038

Appendix B

GPS Receiver Delays and their Sources

Antenna

Hardware delay and inter-
frequency source

Inter-channel biases source

GPS Receiver Front End

| Preamplifier | Down Converter | IF |

Signal processing

Navigation Processing

Pos
Vel
Time

LO

LOs and Clocks

Reference oscillator

Frequency Synthesizer
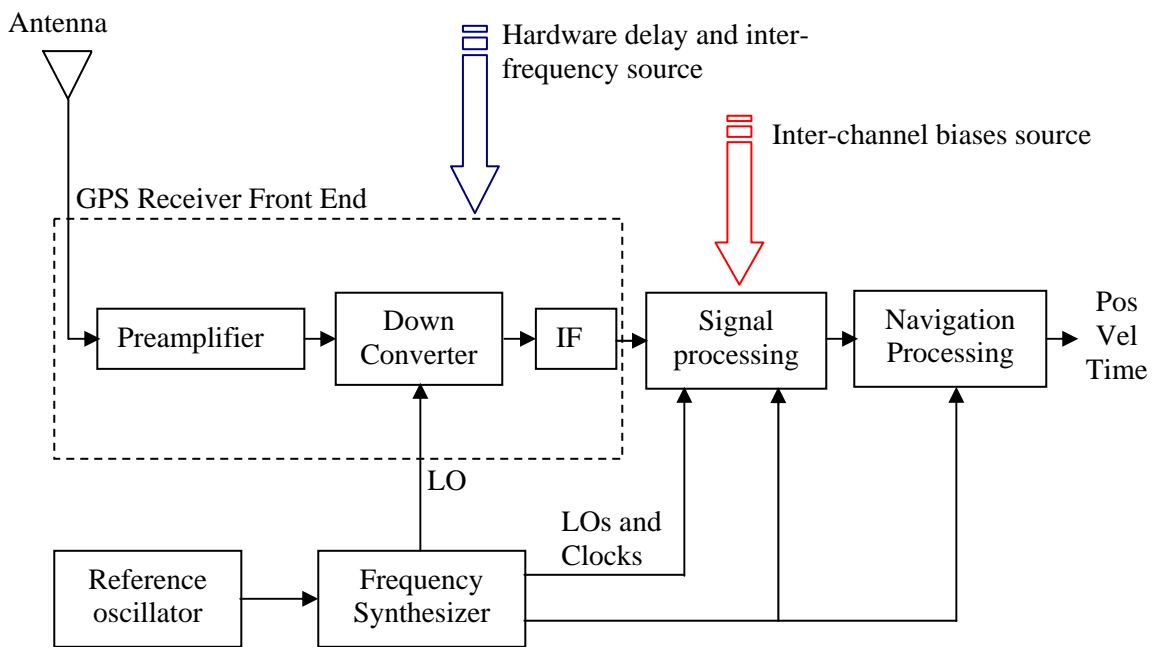
GPS receiver functional diagram (Raquet, 2001)

Can cause

Inter-channel Bias

| Hardware delay | Inter-frequency Bias | Different for L1 and L2 Depends on the channel |
| The same for L1 and L2 | Different for L1 and L2 | |
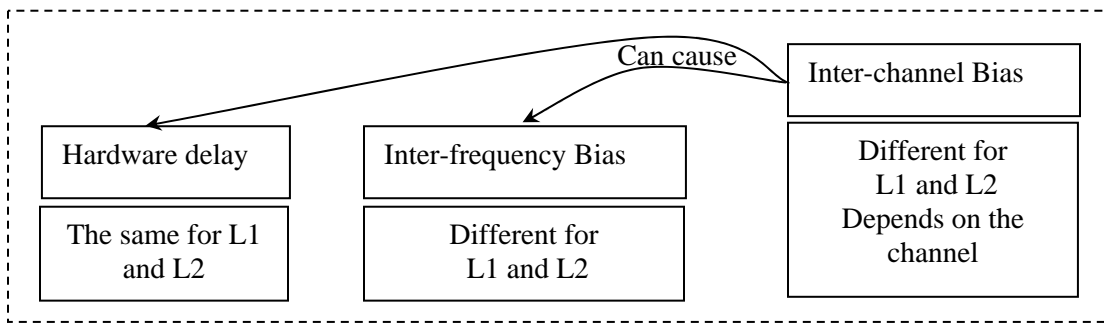
GPS receiver delays and their characteristics (Ray, 2005)

Appendix C

Design Matrix of Traditional Model

$$A_{Station} = \begin{bmatrix} A_{1,1} & A_{1,2} & A_{1,3} \\ A_{2,1} & A_{2,2} & A_{2,3} \\ A_{3,1} & A_{3,2} & A_{3,3} \end{bmatrix} = A_{Station(X,Y,Z)} T_{(\varphi,\lambda,h) \Rightarrow (X,Y,Z)}$$

$$T_{(\varphi,\lambda,h) \Rightarrow (X,Y,Z)} = \begin{bmatrix} -(M+h)\cos\lambda\sin\phi & -(N+h)\cos\phi\sin\lambda & \cos\phi\cos\lambda \\ -(M+h)\cos\lambda\sin\phi & (N+h)\cos\phi\cos\lambda & \cos\phi\sin\lambda \\ (N(1-e^2)+h)\cos\phi & 0 & \sin\phi \end{bmatrix}$$

$$\Delta v_x = \Delta v_x^s - \Delta v_{rx}$$

$$\Delta v_y = \Delta v_y^s - \Delta v_{ry}$$

$$\Delta v_z = \Delta v_z^s - \Delta v_{rz}$$

$$A_{Station(X,y,Z)} =$$

$$\begin{bmatrix} \dfrac{x^s - x}{r_r^s} & \dfrac{y^s - y_r}{r_r^s} & \dfrac{z^s - z_r}{r_r^s} \\ \dfrac{x^s - x}{r_r^s} & \dfrac{y^s - y_r}{r_r^s} & \dfrac{z^s - z_r}{r_r^s} \\ A_{3,1} & A_{3,2} & A_{3,3} \end{bmatrix}$$

$$A_{3,1} = (-\frac{\Delta x^2}{(r_r^s)^3} + \frac{1}{r_r^s})\Delta v_x - \frac{\Delta x \Delta y}{(r_r^s)^3}\Delta v_y - \frac{\Delta x \Delta z}{(r_r^s)^3}\Delta v_z$$

$$A_{3,2} = (-\frac{\Delta y^2}{(r_r^s)^3} + \frac{1}{r_r^s})\Delta v_x - \frac{\Delta y \Delta x}{(r_r^s)^3}\Delta v_y - \frac{\Delta y \Delta z}{(r_r^s)^3}\Delta v_z$$

$$A_{3,3} = (-\frac{\Delta z^2}{(r_r^s)^3} + \frac{1}{r_r^s})\Delta v_x - \frac{\Delta z \Delta x}{(r_r^s)^3}\Delta v_y - \frac{\Delta z \Delta y}{(r_r^s)^3}\Delta v_z$$

$$A_{Station\ Velocity} = \begin{bmatrix} A_{1,1} & A_{1,2} & A_{1,3} \\ A_{2,1} & A_{2,2} & A_{2,3} \\ A_{3,1} & A_{3,2} & A_{3,3} \end{bmatrix} = A_{Station\ Velocity(\dot{X},\dot{Y},\dot{Z})} T_{(\dot{\varphi},\dot{\lambda},\dot{h}) \Rightarrow (\dot{X},\dot{Y},\dot{Z})}$$

$$A_{Station\ Velocity(X,Y,Z)} = \begin{bmatrix} 0 & 0 & 0 \\ 0 & 0 & 0 \\ \dfrac{x^s - x}{r_r^s} & \dfrac{y^s - y}{r_r^s} & \dfrac{z^s - z}{r_r^s} \end{bmatrix}$$

$$T_{(\dot{\varphi},\dot{\lambda},\dot{h}) \Rightarrow (\dot{X},\dot{Y},\dot{Z})} = \begin{bmatrix} -\cos\lambda\sin\phi & -\sin\lambda & \cos\phi\cos\lambda \\ -\cos\lambda\sin\phi & \sin\lambda & \cos\phi\sin\lambda \\ \cos\phi & 0 & \sin\phi \end{bmatrix}$$

$$A_{clock} = \begin{bmatrix} 1 & 0 \\ 1 & 0 \\ 0 & 1 \end{bmatrix}$$

$$A_{Trop} = \begin{bmatrix} M \\ M \\ 0 \end{bmatrix}$$

$$A_{Ambiguity} = \begin{bmatrix} 0 \\ 1 \\ 0 \end{bmatrix}$$

Appendix D

Design Matrix of UofC Model

$$
A_{Station} = \begin{bmatrix} A_{1,1} & A_{1,2} & A_{1,3} \\ A_{2,1} & A_{2,2} & A_{2,3} \\ A_{3,1} & A_{3,2} & A_{3,3} \\ A_{4,1} & A_{4,2} & A_{4,3} \end{bmatrix} = A_{Station(X,Y,Z)} T_{(\varphi,\lambda,h) \Rightarrow (X,Y,Z)}
$$

$$
T_{(\varphi,\lambda,h) \Rightarrow (X,Y,Z)} = \begin{bmatrix} -(M+h)\cos\lambda\sin\phi & -(N+h)\cos\phi\sin\lambda & \cos\phi\cos\lambda \\ -(M+h)\cos\lambda\sin\phi & (N+h)\cos\phi\sin\lambda & \cos\phi\sin\lambda \\ (N(1-e^2)+h)\cos\phi & 0 & \sin\phi \end{bmatrix}
$$

$$
A_{Station(X,Y,Z)} = \begin{bmatrix} \dfrac{x^s-x_r}{r_r^s} & \dfrac{y^s-y_r}{r_r^s} & \dfrac{z^s-z_r}{r_r^s} \\ \dfrac{x^s-x_r}{r_r^s} & \dfrac{y^s-y_r}{r_r^s} & \dfrac{z^s-z_r}{r_r^s} \\ \dfrac{x^s-x_r}{r_r^s} & \dfrac{y^s-y_r}{r_r^s} & \dfrac{z^s-z_r}{r_r^s} \\ A_{4,1} & A_{4,1} & A_{4,1} \end{bmatrix}
$$

$$
\Delta v_x = \Delta v_x^s - \Delta v_{rx}
$$

$$
\Delta v_y = \Delta v_y^s - \Delta v_{ry}
$$

$$
\Delta v_z = \Delta v_z^s - \Delta v_{rz}
$$

$$
A_{4,1} = (-\frac{\Delta x^2}{(r_r^s)^3} + \frac{1}{r_r^s})\Delta v_x - \frac{\Delta x \Delta y}{(r_r^s)^3}\Delta v_y - \frac{\Delta x \Delta z}{(r_r^s)^3}\Delta v_z
$$

$$
A_{4,2} = (-\frac{\Delta y^2}{(r_r^s)^3} + \frac{1}{r_r^s})\Delta v_x - \frac{\Delta y \Delta x}{(r_r^s)^3}\Delta v_y - \frac{\Delta y \Delta z}{(r_r^s)^3}\Delta v_z
$$

$$
A_{4,3} = (-\frac{\Delta z^2}{(r_r^s)^3} + \frac{1}{r_r^s})\Delta v_x - \frac{\Delta z \Delta x}{(r_r^s)^3}\Delta v_y - \frac{\Delta z \Delta y}{(r_r^s)^3}\Delta v_z
$$

$$A_{Station\ Velocity} = \begin{bmatrix} A_{1,1} & A_{1,2} & A_{1,3} \\ A_{2,1} & A_{2,2} & A_{2,3} \\ A_{3,1} & A_{3,2} & A_{3,3} \\ A_{4,1} & A_{4,2} & A_{4,3} \end{bmatrix} = A_{Station\ Velocity(\dot{X},\dot{Y},\dot{Z})} T_{(\dot{\varphi},\dot{\lambda},\dot{h}) \Rightarrow (\dot{X},\dot{Y},\dot{Z})}$$

$$T_{(\dot{\varphi},\dot{\lambda},\dot{h}) \Rightarrow (\dot{X},\dot{Y},\dot{Z})} = \begin{bmatrix} -\cos\lambda\sin\phi & -\sin\lambda & \cos\phi\cos\lambda \\ -\cos\lambda\sin\phi & \sin\lambda & \cos\phi\sin\lambda \\ \cos\phi & 0 & \sin\phi \end{bmatrix}$$

$$A_{Station\ Velocity(X,y,Z)} = \begin{bmatrix} 0 & 0 & 0 \\ 0 & 0 & 0 \\ 0 & 0 & 0 \\ \dfrac{x^s - x}{r_r^s} & \dfrac{y^s - y}{r_r^s} & \dfrac{y^s - y}{r_r^s} \end{bmatrix}$$

$$A_{clock} = \begin{bmatrix} 1 & 0 \\ 1 & 0 \\ 1 & 0 \\ 0 & 1 \end{bmatrix}$$

$$A_{Trop} = \begin{bmatrix} M \\ M \\ M \\ 0 \end{bmatrix} ; M \text{ is the mapping function}$$

$$A_{i\ Ambiguity} = \begin{bmatrix} 0.5\lambda_1 & 0 \\ 0 & 0.5\lambda_1 \\ \dfrac{\lambda_1 f_1^2}{f_1^2 - f_2^2} & \dfrac{\lambda_2 f_2^2}{f_1^2 - f_2^2} \\ 0 & 0 \end{bmatrix}$$

Appendix E

Smoothed Code and Carrier Phase Correlation

$$\Phi_k = \Phi_k$$

$$P_s = \frac{1}{m}P_k + (1 - \frac{1}{m})(P_{k-1} + \Phi_k - \Phi_{k-1})$$

Where m is the number of epochs used in the smoothing process.

$$\begin{bmatrix} \sigma_\Phi^2 & \sigma_{P_s\Phi}^2 \\ \sigma_{P_s\Phi}^2 & \sigma_{P_s}^2 \end{bmatrix} = \begin{bmatrix} \dfrac{\partial\Phi_k}{\partial\Phi_k} & \dfrac{\partial\Phi_k}{\partial\Phi_{k-1}} & \dfrac{\partial\Phi_k}{\partial P_k} & \dfrac{\partial\Phi_k}{\partial P_{k-1}} \\ \dfrac{\partial P_s}{\partial\Phi_k} & \dfrac{\partial P_s}{\partial\Phi_{k-1}} & \dfrac{\partial P_s}{\partial P_k} & \dfrac{\partial P_s}{\partial P_{k-1}} \end{bmatrix} \begin{bmatrix} \sigma_{\Phi_k}^2 & & & \\ & \sigma_{\Phi_{k-1}}^2 & & \\ & & \sigma_{P_k}^2 & \\ & & & \sigma_{P_{k-1}}^2 \end{bmatrix} \begin{bmatrix} \dfrac{\partial\Phi_k}{\partial\Phi_k} & \dfrac{\partial P_s}{\partial\Phi_k} \\ \dfrac{\partial\Phi_k}{\partial\Phi_{k-1}} & \dfrac{\partial P_s}{\partial\Phi_{k-1}} \\ \dfrac{\partial\Phi_k}{\partial P_k} & \dfrac{\partial P_s}{\partial P_k} \\ \dfrac{\partial\Phi_k}{\partial P_{k-1}} & \dfrac{\partial P_s}{\partial P_{k-1}} \end{bmatrix}$$

$$\begin{bmatrix} \sigma_\Phi^2 & \sigma_{P_s\Phi}^2 \\ \sigma_{P_s\Phi}^2 & \sigma_{P_s}^2 \end{bmatrix} = \begin{bmatrix} 1 & 0 & 0 & 0 \\ 1-\dfrac{1}{m} & -1+\dfrac{1}{m} & \dfrac{1}{m} & 1-\dfrac{1}{m} \end{bmatrix} \begin{bmatrix} \sigma_{\Phi_k}^2 & & & \\ & \sigma_{\Phi_{k-1}}^2 & & \\ & & \sigma_{P_k}^2 & \\ & & & \sigma_{P_{k-1}}^2 \end{bmatrix} \begin{bmatrix} 1 & 1-\dfrac{1}{m} \\ 0 & -1+\dfrac{1}{m} \\ 0 & \dfrac{1}{m} \\ 0 & 1-\dfrac{1}{m} \end{bmatrix}$$

$$\begin{bmatrix} \sigma_\Phi^2 & \sigma_{P_s\Phi}^2 \\ \sigma_{P_s\Phi}^2 & \sigma_{P_s}^2 \end{bmatrix} = \begin{bmatrix} \sigma_\Phi^2 & (1-\dfrac{1}{m})\sigma_{\Phi_k}^2 \\ (1-\dfrac{1}{m})\sigma_{\Phi_k}^2 & (1-\dfrac{1}{m})^2\sigma_{\Phi_k}^2 + (1-\dfrac{1}{m})^2\sigma_{\Phi_{k-1}}^2 + \dfrac{1}{m^2}\sigma_{P_k}^2 + (1-\dfrac{1}{m})^2\sigma_{P_{k-1}}^2 \end{bmatrix}$$

Appendix F

Observations Correlation (UofC model)

$$l_1 = 0.5(\Phi_1 + P_1)$$

$$l_2 = 0.5(\Phi_2 + P_2)$$

$$l_3 = \frac{f_1^2 \Phi_1 - f_2^2 \Phi_2}{f_1^2 - f_2^2}$$

$$
\begin{bmatrix}
\sigma_{l_1}^2 & \sigma_{l_{12}}^2 & \sigma_{l_{31}}^2 \\
\sigma_{l_{21}}^2 & \sigma_{l_2}^2 & \sigma_{l_{23}}^2 \\
\sigma_{l_{31}}^2 & \sigma_{l_{32}}^2 & \sigma_{l_3}^2
\end{bmatrix} =
$$

$$
\begin{bmatrix}
\dfrac{\partial l_1}{\partial \Phi_1} & \dfrac{\partial l_1}{\partial \Phi_2} & \dfrac{\partial l_1}{\partial P_1} & \dfrac{\partial l_1}{\partial P_2} \\
\dfrac{\partial l_2}{\partial \Phi_1} & \dfrac{\partial l_2}{\partial \Phi_2} & \dfrac{\partial l_2}{\partial P_1} & \dfrac{\partial l_2}{\partial P_2} \\
\dfrac{\partial l_3}{\partial \Phi_1} & \dfrac{\partial l_3}{\partial \Phi_2} & \dfrac{\partial l_3}{\partial P_1} & \dfrac{\partial l_3}{\partial P_2}
\end{bmatrix}
\begin{bmatrix}
\sigma_{\Phi_1}^2 & & & \\
& \sigma_{\Phi_2}^2 & & \\
& & \sigma_{P_1}^2 & \\
& & & \sigma_{P_2}^2
\end{bmatrix}
\begin{bmatrix}
\dfrac{\partial l_1}{\partial \Phi_1} & \dfrac{\partial l_2}{\partial \Phi_1} & \dfrac{\partial l_3}{\partial \Phi_1} \\
\dfrac{\partial l_1}{\partial \Phi_2} & \dfrac{\partial l_2}{\partial \Phi_2} & \dfrac{\partial l_3}{\partial \Phi_2} \\
\dfrac{\partial l_1}{\partial P_1} & \dfrac{\partial l_2}{\partial P_1} & \dfrac{\partial l_3}{\partial P_1} \\
\dfrac{\partial l_1}{\partial P_2} & \dfrac{\partial l_2}{\partial P_2} & \dfrac{\partial l_3}{\partial P_2}
\end{bmatrix}
$$

$$
=
\begin{bmatrix}
0.5 & 0 & 0.5 & 0 \\
0 & 0.5 & 0 & 0.5 \\
\dfrac{f_1^2}{f_1^2 - f_2^2} & \dfrac{-f_2^2}{f_1^2 - f_2^2} & 0 & 0
\end{bmatrix}
\begin{bmatrix}
\sigma_{\Phi_1}^2 & & & \\
& \sigma_{\Phi_2}^2 & & \\
& & \sigma_{P_2}^2 & \\
& & & \sigma_{P_2}^2
\end{bmatrix}
\begin{bmatrix}
0.5 & 0 & \dfrac{f_1^2}{f_1^2 - f_2^2} \\
0 & 0.5 & \dfrac{-f_2^2}{f_1^2 - f_2^2} \\
0.5 & 0 & 0 \\
0 & 0.5 & 0
\end{bmatrix}
$$

$$
=
\begin{bmatrix}
0.25\sigma_{\Phi_1}^2 + 0.25\sigma_{P_1}^2 & 0 & 0.5\dfrac{f_1^2}{f_1^2 - f_2^2}\sigma_{\Phi_1}^2 \\
0 & 0.25\sigma_{\Phi_2}^2 + 0.25\sigma_{P_2}^2 & 0.5\dfrac{f_2^2}{f_1^2 - f_2^2}\sigma_{\Phi 2}^2 \\
0.5\dfrac{f_1^2}{f_1^2 - f_2^2}\sigma_{\Phi_1}^2 & 0.5\dfrac{f_2^2}{f_1^2 - f_2^2}\sigma_{\Phi 2}^2 & (\dfrac{f_2^2}{f_1^2 - f_2^2})^2\sigma_{\Phi_1}^2 + (\dfrac{f_2^2}{f_1^2 - f_2^2})^2\sigma_{\Phi_2}^2
\end{bmatrix}
$$